Fabrication and Characterization of Novel Nanostructures Based on Block Copolymer Lithography

By

Vivian Peng-Wei Chuang

B.S. Materials Science and Engineering (2004)
National Chung Hsin University

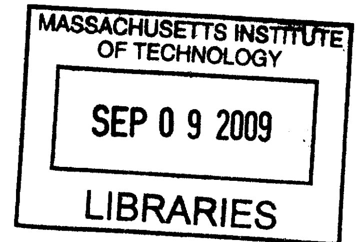
MASSACHUSETTS INSTITUTE OF TECHNOLOGY
SEP 0 9 2009
LIBRARIES

Submitted to the Department of Materials Science and Engineering
in partial fulfillment of the requirements for the degree of

Doctor of Philosophy in Materials Science and Engineering

at the

Massachusetts Institute of Technology

ARCHIVES

Sept. 2009

© Massachusetts Institute of Technology
All rights reserved

Signature of Author ____________________
Department of Materials Science and Engineering
July 22, 2009

Certified by ____________________
Caroline A. Ross
Toyota Professor of Materials Science and Engineering
Thesis Supervisor

Accepted by ____________________
Christine Ortiz
Associate Professor of Materials Science and Engineering
Chair, Departmental Committee on Graduate Students

Fabrication and Characterization of Novel Nanostructures Based on Block Copolymer Lithography

By

Vivian Peng-Wei Chuang

Submitted to the Department of Materials Science and Engineering
On July 22, 2009 in Partial Fulfillment of the Requirements for the
Degree of Doctor of Philosophy in Materials Science and Engineering

Abstract

Microphase-separation of block copolymers into periodic nanoscale structures has drawn considerable attention as a method for pattern generation in nanolithography. One of the main challenges is to create complex nanostructures other than closed-packed nanodots or nanoholes with hexagonal symmetry, or parallel nanolines based on block copolymer lithography. In this thesis, we demonstrate two approaches to generate novel structures such as ellipsoids, rings or square array of dots: diblock copolymers templating and triblock terpolymers. Without templating, diblock copolymer can only form spheres, cylinders, or lamellae typically. Triblock terpolymers, on the other hand, can form a larger number of morphologies even without using any template. The use of triblock terpolymers allows the formation of more complex pattern geometries compared to their diblock counterparts. Moreover, since most features in this thesis are made from an organometallic block, they have a high etch contrast and etch resistance compared to triblock terpolymers in which all three blocks contains organic segments, making them useful for pattern transfer. Rings are useful in the magnetic applications, quantum devices, and biosensors. Square symmetry array, which is not found in diblock copolymers, has applications in via formation, magnetic patterned media, and other applications. Besides, we examine the magnetic behavior of the antidot arrays of Co and pseudo-spin-valve structures with periodicity of 26 nm and 40 nm. As the inter-hole spacing is decreased, both experiment and simulation results show that the coercivity and switching field distribution is reduced, unlike the behavior seen in films with micron- sized holes. In the multilayer, unlike the continuous film, the NiFe reverses at positive fields due to the strong magnetostatic interactions between the Co and NiFe layers present near the holes. Finally, arrays of high-aspect-ratio single crystal silicon nanowires (SiNWs) have also been fabricate by combining block copolymer lithography and metal assisted etching. These SiNWs may be useful in the application of field-effect biosensors and lithium batteries.

Thesis supervisor: Caroline A. Ross
Title: Toyota Professor of Materials Science and Engineering

Table of Contents

Chapter 1 Introduction/Motivation 12

Chapter 2 Background 17

2.1 Diblock copolymers 17

2.2 Triblock terpolymers 20

2.3 Orientation control 23

2.4 Nonregular structures from templated block copolymers 26

Chapter 3 Templated self-assembly of a spherical PS-*b*-PFS diblock copolymer 30

3.1 Introduction 30

3.2 Experimental Methods 31

3.2.1 Fabrication of topographical substrates 31

3.2.2 Non- periodic structures-narrow channels 33

3.2.3 V-shaped grooved substrates 33

3.2.4 Preparation of block copolymer thin films 34

3.3 Self-Assembled One-Dimensional Nanostructure Arrays[22] 35

3.3.1 Effect of confinement width on a single row of PFS domains 36

3.3.2 Analysis of elliptical distortion in 1D arrays 38

3.4 Three-Dimensional Self-Assembly of Spherical Block Copolymer Domains into V-Shaped Grooves[45] 44

3.4.1 The geometrical packing of the PFS spheres within the V groove 45

3.4.2 The effect of polymer film thickness on the 3D structure of the PFS sphere array 48

3.4.3 The packing behavior in shallow trenches and in V grooves 52

3.4.4 Pattern transfer of the surface pattern from 3-D structures 54

Chapter 4 Novel structures from triblock terpolymers with all organic segments 59

4.1 Introduction 59

4.2 Experimental Methods 61

4.2.1 Synthesis and characterization of $PB_{1,4}$-*b*-PS-*b*-PMMA triblock terpolymers 61

4.2.2 Thin film deposition and characterization 64

4.3 Criteria for polymer design 65

4.4 $PB_{1,4}$-*b*-PS-*b*-PMMA triblock terpolymer characteristics 65

4.5 Thin film orientation and morphology 67

4.5.1 Effect of solvent annealing 67

4.5.2 Effect of film thickness 68

4.5.3 Selective etching of the PS, PB and PMMA blocks 72

4.5.4 Pattern transfer into silica 74

4.6 Conclusion 77

Chapter 5. Nanoscale ring arrays from polyferrocenylsilane containing triblock terpolymer 81

5.1 Introduction 81

5.2 Experimental methods 83

5.2.1 Equipment and materials for synthesis of PS-b-PFS-b-P2VP triblock terpolymers 83

5.2.2 Synthesis and characterization of PS-b-PFS-b-P2VP triblock terpolymers 84

5.2.3 Bulk morphology determination 87

5.2.4 Thin film deposition and characterization 88

5.3 Polymer design 88

5.4 Self assembly of PS-*b*-PFS-*b*-P2VP triblock terpolymers in the bulk state 89

5.5 Thin film orientation and morphology 90

5.5.1 Effect of solvent annealing 90

5.5.2 Effect of film thickness 94

5.5.3 Effect of substrate chemistry 95

5.6 Selective etching of the PS, PFS and P2VP blocks and pattern transfer 96

5.7 Conclusion 98

Chapter 6 Templated self-assembly of square arrays from an ABC triblock terpolymer 103

6.1 Introduction 103

6.2 Experimental methods 104

6.2.1 Triblock Terpolymer Synthesis: Equipment and Materials 104

6.2.2 Synthesis and Characterization of PI-b-PS-b-PFS Triblock Terpolymer 105

6.2.3 Thin film deposition and characterization 108

6.3 Polymer design 108

6.4 Self assembly of PI-*b*-PS-*b*-PFS triblock terpolymers in bulk 109

6.5 Thin film morphology on Si substrate 109

6.6 Templated assembly of blended PI-*b*-PS-*b*-PFS triblock terpolymer 114

6.7 Pattern transfer 117

Chapter 7 Applications 121

7.1 Multilayer magnetic antidot arrays from block copolymer templates[1] 121

7.1.1 Introduction 121

7.1.2 Experimental methods 123

7.1.3 Magnetic properties of single-layer Co antidot arrays 125

7.1.4 Magnetic behavior of multilayer antidot arrays 127

7.1.5 Conclusions 134

7.2 Densely-packed arrays of ultrahigh-aspect-ratio silicon nanowire fabricated using block copolymer lithography and metal-assisted etching 135

7.2.1 Introduction 135

7.2.2 Experiment Method 138

7.2.3. Control of Size Distributions, Aspect Ratios, Densities and Locations 145

7.2.4 Properties of nanowires 148

7.2.5 Conclusions 149

Chapter 8 Conclusions and Future Work 154

8.1 Conclusions 154

8.2 Future work 156

List of Figures

Figure 1-1 Process flow for MOS capacitors.. 14

Figure 2-1 Schematics of diblock copolymer phases.. 18

Figure 2-2 A schematic of block copolymer thin film morphologies..........................20

Figure 2-3 Morphologies for linear ABC triblock copolymer.................................. 21

Figure 2-4 Schematic of other morphologies from a linear ABC triblock terpolymer....... 23

Figure 2-5 Schematic molecular picture of how the solvent molecule evaporates in the situations when the top surface of the polymer is covered with the ordering front of lamellae with two orientations... 25

Figure 2-6 A schematic of a symmetric triblock terpolymer (a) in bulk (b) confined lamellar layers with the parallel orientation in which the favorable B component is buried within the layer (c) confined lamellar layers with perpendicular orientation in which at least some of the favorable B component is exposed to the surface... 26

Figure 3-1 Schematics of (a) Lloyd's mirror set up for interference lithography (b) angle-of-incidence on the substrate for the direct and reflected beams................................. 33

Figure 3-2 Schematic of a step-by step procedure for making a topographical substrate... 34

Figure 3-3 SEM images of (a) V-shaped groove anisotropically etched in a (100) silicon substrate with 400 nm period and (b) a PS-PFS polymer film spun on V-shaped grooves and then annealed at 140 °C for 72 h.. 35

Figure 3-4 A composite image of PFS block copolymer domains within channels of different confinement widths *W*... 38

Figure 3-5 (a) The domain dimensions parallel and perpendicular to the channel (b) The calculated aspect ratio of the domains. (c) The periodicity of the 1D array is equal to $p0$, the center-to-center spacing of the unconfined block copolymer, and independent of confinement width... 40

Figure 3-6 (a) A tilted view of a sample with channel width near the one-row to two-row transition. (b) A section of a channel with $W/d0 = 1.5$... 41

Figure 3-7 (a) Energy per chain of the confined polymer as a function of aspect ratio of the domains. (b) The optimum domain aspect ratio that minimizes the free energy at a given confinement width increases linearly with confinement width................................ 44

Figure 3-8 Schematic of the packing of spheres within a V groove.......................... 47

Figure 3-9 SEM images of PS-PFS films in V grooves after 72 h annealing and etching. (a) Square packing of spheres is visible in the top view; (b) the same sample as that in part a in a

crosssectional view showing a sphere array with 11 rows; (c) the polymer directly adjacent to the groove surfaces shows a hexagonal arrangement.. 48

Figure 3-10 SEM images of PS-PFS films with various thicknesses in V grooves, after 72 h annealing and etching.. 50

Figure 3-11 (a) SEM image of a sphere array showing a close-packed sphere arrangement on the top surface. (b) SEM image of a crosssection of the same sample showing the nonepitaxial top layer above the fcc arrangement of the lower layers.. 50

Figure 3-12 Number of layers of spheres in the cross-section images plotted against the polymer film thickness.. 52

Figure 3-13 Top: SEM image showing a change in the number of rows in the top layer of a sphere array from 4 to 5, and the presence of an associated defect in the packing is marked in red.. 54

Figure 4-1 Schematic of a concentric cylinder morphology triblock terpolymer PB-*b*-PS-*b*-PMMA.. 62

Figure 4-2 (a) SEC chromatogram of the intermediate compounds and final PB-*b*-PS-*b*-PMMA triblock terpolymer BSM141, (b) 1H NMR of the PB1,4-*b*-PS-*b*-PMMA triblock terpolymer BSM[141] 67

Figure 4-3 SEM images of thin films of BSM179 with different thicknesses (labeled) after annealing in toluene vapor for 17.5 hrs at room temperature, followed by exposure with deep UV and etching with oxygen RIE to remove the PMMA, then etching with UV/O3 and water to remove PB.. 70

Figure 4-4 The period of the cylindrical domains in BSM[179] as a function of thickness. The error bars show one standard deviation.. 71

Figure 4-5 SEM images of thin films of PB-*b*-PS-*b*-PMMA (a) MW: 141 kg/mol (b) MW: 179 kg/mol (c) MW: 185kg/mol after annealing in toluene vapor, then UV exposure and etching with oxygen plasma.. 72

Figure 4-6 Pattern transfer into silica rings from a BSM179 film annealed in acetone vapor for 6 hrs... 77

Figure 5-1 GPC trace (RI) of triblock terpolymer PS-*b*-PFS-*b*-P2VP and precursor blocks.. 87

Figure 5-2 1H NMR spectrum of PS-*b*-PFS-*b*-P2VP in CD2Cl2, * denotes solvent peak... 88

Figure 5-3 (a) Bright field TEM image of the bulk morphology of the PS-*b*-PFS-*b*-P2VP triblock terpolymer. TEM image is provided by Jessica Gwyther (b)-(e) SEM images of thin films of PS-*b*-PFS-*b*-P2VP on Si after annealing in (b) toluene vapor (c) chloroform vapor (d) mixed solvent

vapor of chloroform and acetone (e) acetone vapor for 4 hours at room temperature, followed by etching with oxygen RIE to remove the PS and P2VP...................................... 92

Figure 5-4 SEM images of thin films of PS-*b*-PFS-*b*-P2VP on Si after annealing in (a)-(c) chloroform and (d)-(f) a mixed solvent vapor of chloroform and acetone for 4 hrs at room temperature, followed by etching with oxygen RIE to remove the PS and P2VP. (a)(d) Plan view (b)(e) Side view (c)(f) Bottom view.. 94

Figure 5-5 SEM images of thin PS-*b*-PFS-*b*-P2VP films with different thickness, after annealing in chloroform vapor, then etching with oxygen plasma.................................... 96

Figure 5-6 (a)-(d) SEM images of bottom view of thin films of PS-*b*-PFS-*b*-P2VP on chemically modified silica substrates after annealing in mixed vapor of chloroform and acetone, then dipping in HF, KOH and etching with oxygen plasma. (a) with PS-OH brush (b) with PFS-OH brush (c) with P2VP brush (d) without brush. (e)-(f)Pattern transfer into a PS layer from a PS-*b*-PFS-*b*-P2VP film annealed in chloroform/acetone vapor for 4 hrs. (e) Mold (f) Imprinted PS layer... 98

Figure 6-1 1H NMR spectrum of PI-*b*-PS-*b*-PFS in CDCl3 and TMS.................... 108

Figure 6-2 (c) Bright field TEM image of the bulk morphology of the pure PI-*b*-PS-*b*-PFS triblock terpolymer. (a)(b)(d)(e) SEM images of thin films of (a) pure PI-*b*-PS-*b*-PFS (b)(d)(e) blended PI-*b*-PS-*b*-PFS on Si after spin-coating and annealing in chloroform vapor for 2.5 hours at room temperature, followed by etching with oxygen RIE to remove both PI and PS blocks. (d) with an additional step of OsO4 staining for 4 hrs before oxygen RIE, giving the PI higher resistance to an oxygen etch.. 111

Figure 6-3 (a) a SEM image of pure PI-*b*-PS-*b*-PFS on Si after spin-coating and annealing in chloroform vapor for 2.5 hours at room temperature, followed by OsO4 staining for 4 hrs and etching with oxygen RIE. (b) schematic of hexagnol packed core-shell structure and square array... 113

Figure 6-4 SEM images of pure PI-*b*-PS-*b*-PFS thin films on Si at different thickness after annealing, followed by etching with oxygen RIE.. 114

Figure 6-5 (a)(b) SEM images of templated assembly of blended PI-*b*-PS-*b*-PFS triblock terpolymer after annealing in chloroform vapor for 2.5 hours at room temperature, followed by etching with oxygen RIE to remove PI and PS domains.(a) with uncoated templates (b) with PS brushed templates. (c) Schematic of packing orientation of blended PI-*b*-PS-*b*-PFS triblock terpolymer in PS brushed templates. (d) A plot of number of rows vs. confinement width for both the 90° and the 45° orientations.. 116

Figure 6-6 SEM images of relatively thick film of blended PI-*b*-PS-*b*-PFS triblock terpolymer assembled in (a) PS brushed template (b) unbrushed substrate after annealing and etching with oxygen RIE... 118

Figure 6-7 (a)-(f) SEM images of (a)-(c)top view and (d)-(f)side view of (a)(d) PFS dots after PI and PS removal;(b)(e) silica dots with PFS cap;(c)(f)silica dots. (h) Schematic of pattern transfer process.. 119

Figure 7-1 Schematic of the fabrication process for the antidot magnetic film............. 124

Figure 7-2 (a) Cross-sectional view of block copolymer templated organosilicate on top of a PMGI underlayer after removal of the polystyrene and unprotected PMGI with an oxygen reactive ion etch. (b) Scanning electron micrograph of antidot array 1. (c) Scanning electron micrograph of antidot array 2... 125

Figure 7-3 (a) Measured hysteresis loops of single-layer Co antidot arrays. (b) Half hysteresis loops of single-layer Co arrays based on micromagnetic modeling. [(c)–(f)] Magnetic configuration calculated for single-layer Co antidot arrays: (c) array 1 at −300 Oe reverse field, (d) array 1 at −1000 Oe, (e) array 2 at −200 Oe, and (f) array 2 at −400 Oe................ 127

Figure 7-4 Major and minor hysteresis loops of the Co(3 nm)/Cu(5 nm)/NiFe(3.5 nm) multilayers measured for (a) continuous film, (b) array 1, and (c) array 2. (d) A schematic representation of the four possible magnetic configurations for the Co and NiFe layers... 129

Figure 7-5 Magnetoresistance data for (a) Continuous film; (b) Array 1; (c) Array 2...... 132

Figure 7-6 (a-e) Snapshots of domain structures and (f) half hysteresis loop of the Co(4 nm)/Cu(4 nm)/NiFe(4 nm) multilayers based on results of simulations at a field of (a) 50 Oe (b) –400 Oe and (c) –750 Oe for array 1, and (d) 50 Oe and (e) –150 Oe for array 2, after positive saturation.. 133

Figure 7-7 Schematic of the SiNW fabrication process.. 141

Figure 7-8 Scanning electron microscope images showing steps in the SiNW fabrication process flow... 142

Figure 7-9 Schematic of the process flow for templated wire fabrication.................... 144

Figure 7-10 SEM images of templated SiNW fabrication.................................... 145

Figure 7-11 Diameter distributions for the wires and the PFS spherical microdomains..... 147

Figure 7-12 (a) SiNW arrays without critical point drying show clustering at the wire tips at a relatively low aspect ratio of 30; (b) SiNW arrays with critical point drying show much less bending at aspect ratios as high as 220.. 149

Figure 8-1 schematic of (a) lamellae-with-cylinders-at-the-interface-phase (b) three-phase four-layer-lamellae.. 158

List of Tables

Table 4-1 Volume percentages (v/v%), polydispersity (PDI) and weight percentages (w/w%) of the three triblock terpolymers........ 64

Table 4-2 Period and dimensions of PS ring patterns in films of the three triblock terpolymers after annealing in toluene vapor followed by deep UV exposure and oxygen etching..... 72

Table 4-3 Etching of homopolymer PS (hPS), hPB and hPMMA under different etching conditions........ 74

Table 7-1 The switching fields and interaction field of the NiFe and Co layers in the antidot arrays and in the continuous films........ 130

List of Schemes

Scheme 4-1 Experimental pathway for the synthesis of PB1,4-*b*-PS-*b*-PMMA triblock terpolymers........ 63

Scheme 5-1 Synthesis of PS-*b*-PFS-*b*-P2VP triblock terpolymer........ 86

Scheme 6-1 Synthesis of PI-*b*-PS-*b*-PFS triblock terpolymer........ 108

Acknowledgements

I would like to take this opportunity to thank those who have helped me over the past five years. First and foremost, I would like to thank my advisor, Professor Caroline Ross. I have had the great fortune of being able to work in her group. Under her guidance and support, I have learned how to conduct research independently and communicate the results. I can never finish my thesis without her encouragement and unlimited patience.

I have been grateful to my thesis committee, Professor Edwin Thomas and Professor Karl Berggren, for their insightful advice, suggestions, and ideas. I enjoyed discussing polymer physics with Professor Thomas. Professor Hank Smith and Professor Berggren have provided the best resource with the NanoStucture Lab.

Without a doubt, this work would not be a complete story without the contributions of my collaborators: Dr. Joy Cheng, Dr. Robert McMichael, Dr. Panayiotis Bilalis, Jessica Gwyther, and Shih-Wei Chang. Thanks for all your help, support and data. I would like to thank the members of the Magnetic Materials and Devices group for making my life here a little better every day. In particular, thanks to Dr. Joy Cheng, Dr. Filip Ilievski, Dr. Fernando Castaño, Dr. Wonjoon Jung, Dr. Vikram Sivakumar, Dr. Yeon Sik Jung, Dr. Rafal Mickiewicz, Dr. David Otero, Brian Ng, Lei Bi and Kevin Gotrik. Without their expertise, it would have been impossible to make these pages reflect the work behind them. Thanks to Gabrielle Joseph for sharing your experience with me. I want to thank Jim Daley and Tim Savas in NSL for making everything work all the time and your insightful opinions on nanofabrication.

On a personal note, I would like to thank my friends and elders for their support and motivation. They are vital in my survival at MIT. In particular, many thanks to Hsuyi and Shih-Long who were like family away from home. Thank you for keeping me going when times were rough and celebrating with me when they were bright. I would also like to thank Ching-Ying, Chung-Yi, Kevin, Nancy, Thomas, Amy, Elise, Chia-Hua, Yi-Chun, Liang-Yi, and Yu-Chung. Thank you for accepting me as what I am.

Most of All, I would like to thank my family. Thanks to Mom and Dad for bringing me in to this world and supporting me all the way from birth with their everlasting care and unwavering patience. Your unconditional love has truly enabled me to get to this point. Finally, a special thanks goes to my brother Jeff and my sister Jenny and brother in-law John. Thank you for your encouragement and always being there for me.

Chapter 1 Introduction/Motivation

Self-assembled block copolymer thin films have attracted a great deal of attention recently as templates for nanolithography. [1-5] A diblock copolymer consists of two immiscible polymer chains covalently bonded together, and on annealing by cooling from above order-disorder temperature or evaporating of solvent to exceed order-disorder concentration, undergoes a microphase separation to form self-assembled periodic nanoscale domains. The domains can exist in several morphologies depending on the volume fractions of the two constituents of the polymer, including spheres, cylinders, and lamellae, and the domain size and period scale with the molecular weight, making these materials useful masks for nanofabrication. Thin films of block copolymers have been used to pattern semiconductor dot and antidot arrays,[1, 6] metal dots and nanowires, [7-9] and magnetic storage media,[10] and devices such as capacitors, flash memory, and transistors have been fabricated using block copolymer lithography.[11-13] Figure 1-1 shows an example of the fabrication of MOS capacitors from block copolymer lithography. After selectively removing one of the blocks in a spherical block copolymer, the remaining pattern was transferred into Si. The device was then formed by oxidizing the block copolymer patterned Si wafer in a tube furnace at 900°C, followed by aluminum deposition.[11] Recently, IBM has demonstrated self-assembly in the Airgap Microprocessor using block copolymer lithography, in which low-k dielectric material formed using block copolymer lithography. A formation of "vacuum" between chip wiring enables the electrical signals to flow 35% faster and the energy consumption to be reduced by 15%. [14]

Successful implementation of block copolymer (BCP) patterning depends on the ability to control the morphology, orientation and packing of the domains. BCP domain patterns

typically have good short-range order, but lack long-range order. Long range ordering has been accomplished by various approaches such as the application of external electrical fields,[15, 16] temperature gradients,[17] a shear field,[18] or by using chemically or topographically patterned

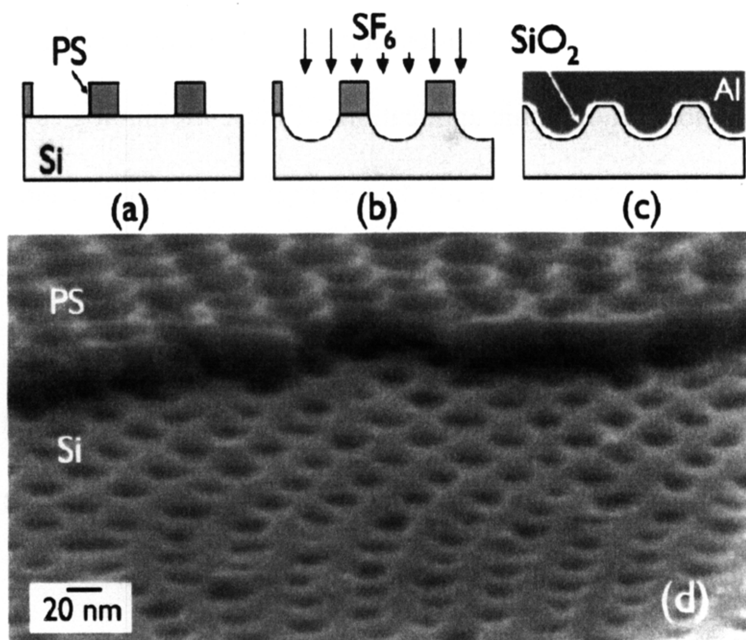

Figure 1-1 Process flow for MOS capacitors. (a) Polymer template on Si after selective removal of another block. (b) Pattern transfer of polymer template into Si, followed by polymer removal. (c) SiO_2 formation, followed by Al deposition. (d) SEM image showing stage (b). Top shows the remaining polymer template after selective removal of spherical domains. Bottom shows the transferred pattern in Si.[11]

substrates.[19-26] Most studies using patterned substrates have focused on the behavior of a diblock copolymer (dBCP), which has a monolayer of spherical or in-plane cylindrical dBCP domains, or on short cylinders or lamellae oriented perpendicular to the surface. In addition, dBCPs have been confined within 3D geometries such as pores or droplets,[15-18] which introduce additional boundary conditions and can promote dBCP morphologies not found in the bulk, such as the

formation of concentric cylinders by lamellar BCPs, or helical structures by cylindrical BCPs. Nevertheless, there are still very limited morphologies that have been made by dBCP.

A combination of block sequence (interaction parameter of the adjacent blocks), volume fraction and molecular weights of ABC triblock polymer thin films provides a diversity of new structures.[19, 20] The possible lithographic applications of these morphologies could include square arrays of discrete metal dots or nanorings for data storage or other applications. The behavior of microphase separation in ABC triblock polymer is more complicated compared to their diblock counterparts since there are three distinct interfaces rather than one and stretching energy contributions from three blocks instead of two[21]. The experimental and theoretical work on ABC triblock terpolymers deals mainly with the bulk morphology,[22-31] and there is only a limited amount of information on the structure of microdomains in thin films.[32-37]

This thesis will investigate both diblock and triblocks with the aim of exploring possible geometries and assessing their suitability in nanolithography. The work will focus particularly on the formation and characterization of magnetic nanostructures made by BCP lithography.

Chapter 2 describes the general background information for diblock and triblock copolymers. Chapter 3 describes templated self-assembly of a spherical polystyrene-*b*-polyferrocenylsilane (PS-*b*-PFS) diblock copolymer. Chapter 4 describes nanoring structures from a triblock terpolymer with all organic segments. Chapter 5 describes self-assembled nanoring arrays from organometalic triblock terpolymer. Chapter 6 describes templated assembly of square arrays from an ABC triblock terpolymer. Chapter 7 demonstrates pattern transfer into magnetic antidot array and Si nanowires. Chapter 8 describes the application of templates in other systems. Chapter 8 gives the conclusions and recommendations for future work.

Reference

1. Park, M.; Harrison, C.; Chaikin, P. M.; Register, R. A.; Adamson, D. H. *Science* **1997,** 276, (5317), 1401-1404.
2. Park, C.; Yoon, J.; Thomas, E. L. *Polymer* **2003,** 44, (22), 6725-6760.
3. Segalman, R. A. *Materials Science and Engineering: R: Reports* **2005,** 48, (6), 191-226.
4. Darling, S. B. *Progress in Polymer Science* **2007,** 32, (10), 1152-1204.
5. Cheng, J. Y.; Ross, C. A.; Smith, H. I.; Thomas, E. L. *Advanced materials* **2006,** 18, (19), 2505-2521.
6. Li, R. R.; Dapkus, P. D.; Thompson, M. E.; Jeong, W. G.; Harrison, C.; Chaikin, P. M.; Register, R. A.; Adamson, D. H. *Applied Physics Letters* **2000,** 76, (13), 1689-1691.
7. Lopes, W. A.; Jaeger, H. M. *Nature* **2001,** 414, (6865), 735-738.
8. Thurn-Albrecht, T.; Schotter, J.; Kastle, G. A.; Emley, N.; Shibauchi, T.; Krusin-Elbaum, L.; Guarini, K.; Black, C. T.; Tuominen, M. T.; Russell, T. P. *Science* **2000,** 290, (5499), 2126-2129.
9. Cheng, J. Y.; Ross, C. A.; Chan, V. Z. H.; Thomas, E. L.; Lammertink, R. G. H.; Vancso, G. J. *Advanced Materials* **2001,** 13, (15), 1174-1178.
10. Naito, K.; Hieda, H.; Sakurai, M.; Kamata, Y.; Asakawa, K., 2.5-in. Disk Patterned Media Prepared by an Artificially Assisted Self-Assembling Method. In 2002; Vol. 38, p 1949.
11. Black, C. T.; Guarini, K. W.; Milkove, K. R.; Baker, S. M.; Russell, T. P.; Tuominen, M. T. *Applied Physics Letters* **2001,** 79, (3), 409-411.
12. Black, C. T. *Applied Physics Letters* **2005,** 87, (16), 163116-3.
13. Guarini, K. W.; Black, C. T.; Zhang, Y.; Babich, I. V.; Sikorski, E. M.; Gignac, L. M., Low voltage, scalable nanocrystal flash memory fabricated by templated self assembly. In *IEEE Int. Electron Devices Meet. (IEDM '03)* IEEE: Piscataway, NJ, 2003; p 541.
14. Nitta, S.; Edelstein, D.; Ponoth, S.; Clevenger, L.; Liu, X.; Standaert, T. In *Performance and reliability of airgaps for advanced BEOL Interconnects*, Interconnect Technology Conference, 2008. IITC 2008. International, 2008; 2008; pp 191-192.
15. Wu, Y.; Livneh, T.; Zhang, Y. X.; Cheng, G.; Wang, J.; Tang, J.; Moskovits, M.; Stucky, G. D. *Nano letters* **2004,** 4, (12), 2337-2342.
16. Yu, B.; Sun, P.; Chen, T.; Jin, Q.; Ding, D.; Li, B.; Shi, A.-C. *Physical Review Letters* **2006,** 96, (13), 138306-4.
17. Shin, K.; Xiang, H.; Moon, S. I.; Kim, T.; McCarthy, T. J.; Russell, T. P. *Science* **2004,** 306, (5693), 76.
18. Xiang, H.; Shin, K.; Kim, T.; Moon, S. I.; McCarthy, T. J.; Russell, T. P. *Macromolecules* **2004,** 37, (15), 5660-5664.
19. Bates, F. S.; Fredrickson, G. H. *Physics Today* **1999,** 52, (2), 32-38.
20. Zheng, W.; Wang, Z.-G. *Macromolecules* **1995,** 28, (21), 7215-7223.
21. Matsen, M. W. *The Journal of Chemical Physics* **1998,** 108, (2), 785-796.
22. Hadjichristidis, N.; Iatrou, H.; Pitsikalis, M.; Pispas, S.; Avgeropoulos, A. *Progress in Polymer Science* **2005,** 30, (7), 725-782.
23. Takahashi, K.; Hasegawa, H.; Hashimoto, T.; Bellas, V.; Iatrou, H.; Hadjichristidis, N. *Macromolecules* **2002,** 35, (13), 4859-4861.
24. Gido, S. P.; Schwark, D. W.; Thomas, E. L.; do Carmo Goncalves, M. *Macromolecules* **1993,** 26, (10), 2636-2640.

25. Brinkmann, S.; Stadler, R.; Thomas, E. L. *macromolecules* **1998,** 31, (19), 6566-6572.
26. Ludwigs, S.; Böker, A.; Abetz, V.; Müller, A. H. E.; Krausch, G. *Polymer* **2003,** 44, (22), 6815-6823.
27. Breiner, U.; Krappe, U.; Jakob, T.; Abetz, V.; Stadler, R. *Polymer Bulletin* **1998,** 40, (2), 219-226.
28. Breiner, U.; Krappe, U.; Abetz, V.; Stadler, R. *Macromolecular Chemistry and Physics* **1997,** 198, (4), 1051-1083.
29. Krappe, U.; Stadler, R.; Voigt-Martin, I. *Macromolecules* **1995,** 28, (13), 4558-4561.
30. Jung, K.; Abetz, V.; Stadler, R. *Macromolecules* **1996,** 29, (3), 1076-1078.
31. Breiner, U.; Krappe, U.; Thomas, E. L.; Stadler, R. *Macromolecules* **1998,** 31, (1), 135-141.
32. Stocker, W.; Beckmann, J.; Stadler, R.; Rabe, J. P. *Macromolecules* **1996,** 29, (23), 7502-7507.
33. Elbs, H.; Drummer, C.; Abetz, V.; Krausch, G. *Macromolecules* **2002,** 35, (14), 5570-5577.
34. Böker, A.; Müller, A. H. E.; Krausch, G. *Macromolecules* **2001,** 34, (21), 7477-7488.
35. Elbs, H.; Abetz, V.; Hadziioannou, G.; Drummer, C.; Krausch, G. *Macromolecules* **2001,** 34, (23), 7917-7919.
36. Bang, J.; Kim, S. H.; Drockenmuller, E.; Misner, M. J.; Russell, T. P.; Hawker, C. J. **2006,** 128, (23), 7622-7629.
37. Guo, S.; Rzayev, J.; Bailey, T. S.; Zalusky, A. S.; Olayo-Valles, R.; Hillmyer, M. A. *Chemistry of Materials* **2006,** 18, (7), 1719-1721.

Chapter 2 Background

This chapter explains the principles of the block copolymer self-assembling process and methods for controlling the perpendicular orientation of the microdomains. Finally, nonregular structures from templated self-assembly will also be discussed.

2.1 Diblock copolymers

Diblock copolymers consist of two chemically distinct polymer chains covalently joined together. Below its order-disorder temperature, the block copolymer tends to undergo microphase separation into a periodic nanoscale structure to lower its free energy by minimizing the interfacial area and maximizing the chain conformational entropy. Depending on the volume ratio of A versus B block in a AB diblock copolymer, it can self-assemble into several bulk morphologies: spheres, cylinders, gyroid and lamellae, as shown in figure 2-1.

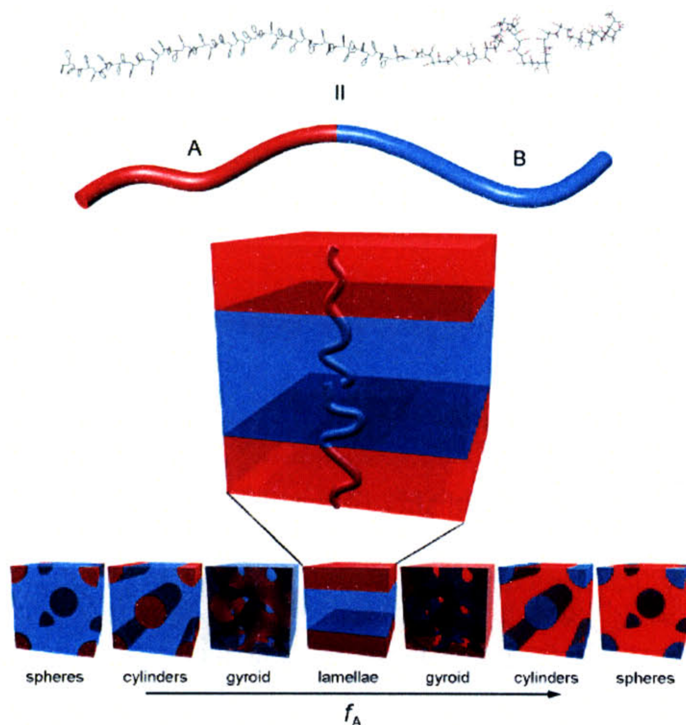

Figure 2-1 Schematics of diblock copolymer phases.[1]

For example, if A and B blocks have the same length, A and B can self-assemble into a lamellae structure. Furthermore, the free energy of lamellae can be described by the following formula:

$$\Delta G = \Delta H - T\Delta S$$
$$= \gamma_{AB}\sum - N\chi_{AB}\phi_A\phi_B kT + \frac{3}{2}kT\left[\frac{(\lambda/2)^2}{Na^2} - 1\right]$$

where

G = Free energy per chain

H = Enthalpy

S= Entropy

γ_{AB} = Interfacial energy = $(kT/a^2)*\sqrt{(\chi_{AB}/6)}$

Σ = Interfacial area per chain = $(Na^3)/(\lambda/2)$

N = Number of segments = $N_A + N_B$

χ_{AB} = Segment-segment interaction parameter = $(z/kT)*[\varepsilon_{AB}-(1/2)*(\varepsilon_{AA}+\varepsilon_{BB})]$

ϕ_A, ϕ_B = Volume fraction of the components

a = Step size

λ = Domain periodicity

z = Coordination number

$\varepsilon_{AB}, \varepsilon_{AA}, \varepsilon_{BB}$ = Energy of interaction between A and B, A and A, and B and B

The first two terms describe enthalpy of the system and the last one corresponds to an entropic spring term. By first derivative free energy with domain periodicity and setting it to zero, the equilibrium domain spacing for lamellae can be calculated:

$$\lambda \cong aN^{2/3}\chi_{AB}^{1/6}$$

As a consequence, the domain spacing scales with $N^{2/3}$. The larger the molecular weight, the larger the period. χ represents the chemical interaction between the two components and is associated with the penalty of contacts between A-B segments. The higher the χ parameter, the more immiscible the two blocks are.

Block copolymer thin films are useful for lithographic applications. In these cases, surface/interfacial energy becomes very important as the film thickness decreases. The thin film morphology of block copolymers can differ from the bulk morphology. Figure 2-2 shows a schematic of thin film morphologies of lamellar, cylindrical, and spherical block copolymer.

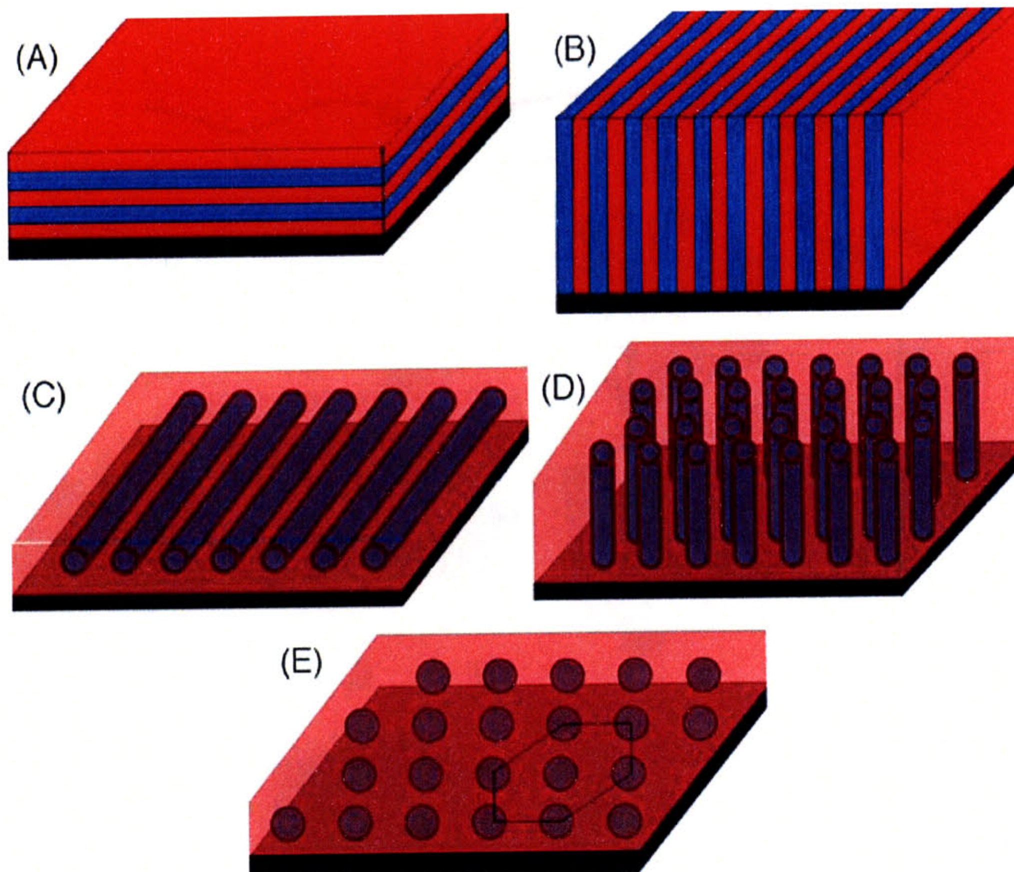

Figure 2-2 A schematic of block copolymer thin film morphologies. (a) Parallel aligned lamellae (b) vertical aligned lamellae, (c) parallel aligned cylinders (D) vertical aligned cylinders packed with hexagonal symmetry, and (E) spheres packed with hexagonal symmetry.[2]

Vertically aligned lamellae and parallel aligned cylinders are useful for patterning nanowires. On the other hand, vertically aligned cylinders and spheres are interesting for applications such as magnetic data storage. Several methods for controlling the orientation of lamellae and cylinders will be discussed in 2.1.3.

2.2 Triblock terpolymers

A combination of block sequences, composition and molecular weights creates a large number of new morphologies in the case of triblock terpolymers which allow for patterning many different pattern geometries. Figure 2-3 shows the bulk morphology of a linear ABC triblock terpolymer.[3]

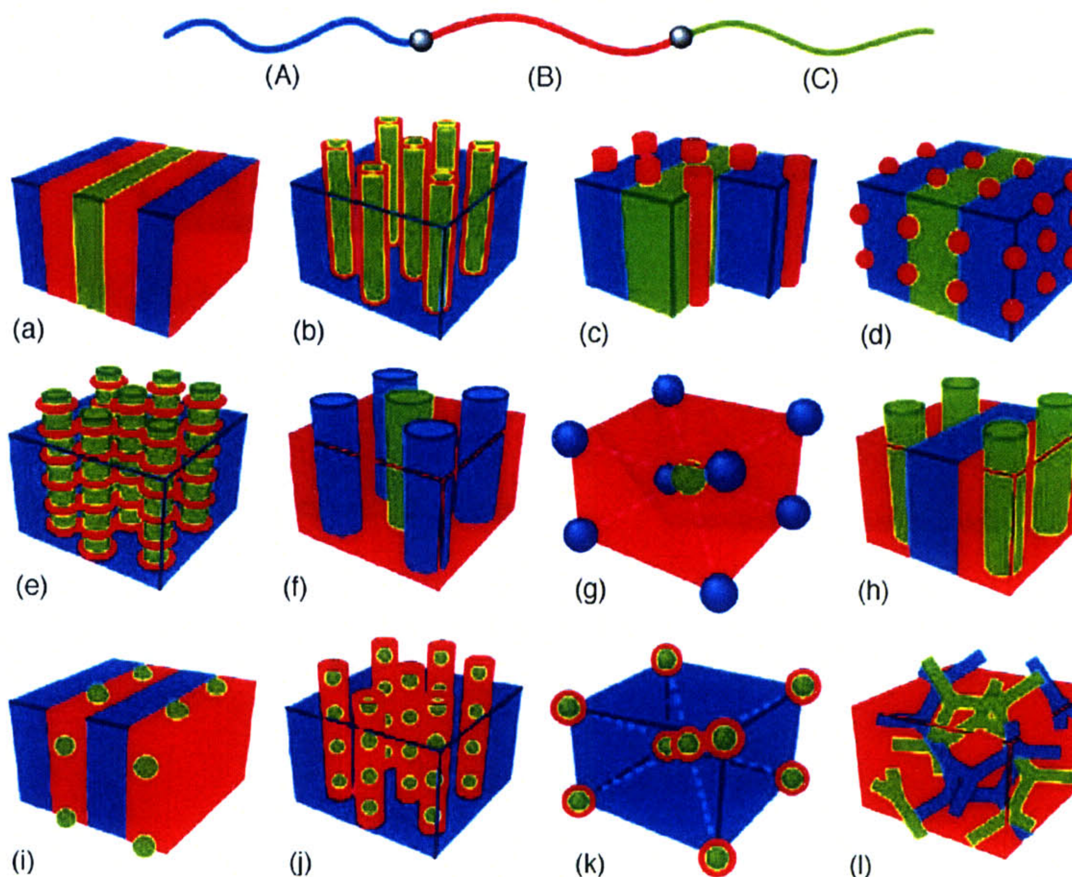

Figure 2-3 Morphologies for linear ABC triblock copolymer.[3]

Block sequence and the relative strength of interaction parameters play an important role in the morphology of a triblock terpolymer.[4] For example, with volume ratio 1:1:1, polystyrene-b-polyisoprene-b-poly-2-vinyl pyridine(PS-b-PI-b-P2VP) forms P2VP core and PI shell cylinders in a PS matrix.[5] On the other hand, with the same volume ratio, polyisoprene-b-polystyrene-b-poly-2-vinylpyridine (PI-b-PS-b-P2VP) forms lamellae.[6] The schematic for this two morphologies are shown in figure 2-3(b) and 2-3(a), respectively. The difference in morphologies is due to the asymmetry of the values of $\chi_{PS\text{-}PI}$ and $\chi_{PI\text{-}P2VP}$. Besides, changing the relative volume ratio among each block also affects the morphology, as observed in diblock copolymers. Breiner et al. studied a series of ABC cylindrical triblock terpolymers with different volume ratio of A and B in a C matrix.[7] In addition to the morphologies showing in Fig. 2-3, other structures such as cylinders-at-cylinder, helical morphology, spheres-on-cylinder, and spheres-on-sphere were observed, as shown in Fig. 2-4.[7, 8]

The general phase behavior of bulk ABC triblock systems can be classified in terms of the relative strength of χ parameters: χ_{AC}/χ_{AB} and χ_{BC}/χ_{AB}.[4] In the case of $\chi_{AC}<\chi_{AB}\cong\chi_{AC}$, contact between A and C is the most favorable. With triblock terpolymers with short middle blocks, the end blocks form lamellae, cylinders or spheres with B decorating the A-C interface. This system has been studied extensively by Stadler's group.[7-10] In the systems where contact between A and C is the least favorable, morphologies form consisting of ABCCBA lamella,[11] core-shell structures (when A or C is the major block),[12, 13] or alternating cylinders or spheres (when B is the major block).[6, 11, 14] In the case where the χ parameters between end blocks and middle block are asymmetric, core-shell structures are more stable than alternating structures.[4, 15]

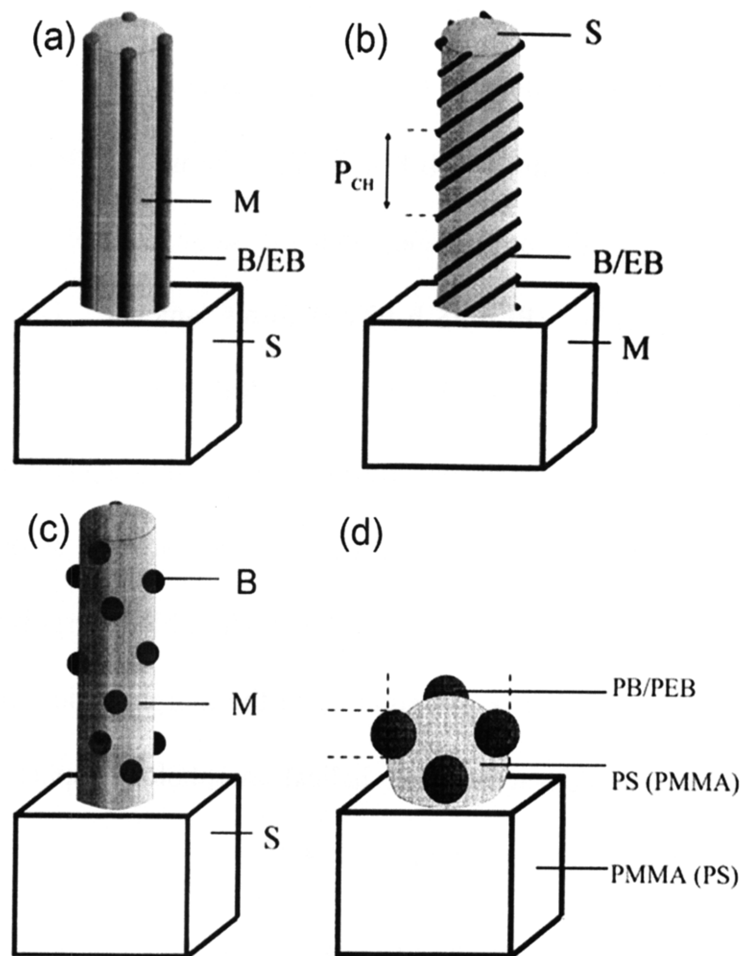

Figure 2-4 Schematic of other morphologies from a linear ABC triblock terpolymer: (a) cylinders- at-cylinder;(b) helical morphology;(c) spheres-on-cylinder; (d) spheres-on-sphere.[7, 8]

As shown in diblock copolymer systems, thin film morphologies of ABC triblock terpolymers are somewhat different from the bulk morphologies. For example, a highly-ordered perforated lamellar structure has been obtained from a thin film of ABC triblock terpolymer which forms a core-shell structure in bulk.[16] By the choosing the lowest surface energy block as a middle block, spontaneous alignment of the perpendicular cylinders was demonstrated.[17] With triblock terpolymers, more functional structures can be obtained compared to diblock copolymers.[18]

2.3 Orientation control

As mentioned in 2.1.1, orientation control, especially for the perpendicular cylindrical or lamellar microdomains, is very important for the use of block copolymers for lithographic applications or fabrication of nanostructures. Several methods have been employed to achieve perpendicular orientation of microdomains in diblock polymers, such as applying electric field,[19, 20] using chemically patterned substrate,[21] adding nanoparticles,[22-24] or homopolymer,[25] controlling humidity,[26] solvent evaporation,[27-31] and thickness.[32] Turturro et al. first observed perpendicular cylinders and lamellae near the free surface of PS-b-PB thin films and discussed the effect of the block surface tension and casting solvent and its evaporation rate on surface morphology.[33] If the evaporation rate is slow, the block copolymer forms parallel cylinders slowly. For two blocks which have a large difference in surface tension, parallel cylinders form in a shorter time. Anastasiadis et al. demonstrated that use of a selective solvent leads to surface enrichment of the most soluble block.[34] As a result, the surface enrichment of PB due to its low surface energy can be hindered by choosing a selective solvent for PS. Moreover, Mori et.al show the glass transition temperature(T_g) of the PS block in PS-b-PI in toluene reaches room temperature as the block copolymer concentration(ϕ_P) increased to 0.75% w/v.[35] Furthermore, the glass transition temperature of PB is much lower than that of PS and thus the free volume available in PB is greater than that of PS for solvent molecules to diffuse through. In addition, toluene is a selective solvent for PS so the toluene molecules escape much faster through PB than PS. In a lamellar structure, such a difference in diffusivity in PB and PS leads to perpendicular orientation of lamellae. Besides, the newly solidified polymer chains during solvent evaporation aggregate much more easily in the normal lamellae than in parallel lamellae, as shown in figure 2-5.[33]

Generally perpendicular orientation of microdomains of diblock copolymers can be promoted by providing a neutral boundary condition at the substrate for each block of the block copolymer, for example, by the use of a random copolymer brush.[36] In the case of ABC triblock polymer, there is no neutral boundary condition for all the three blocks. However, by providing a boundary condition which attracts the middle block, Kubo et al. demonstrated that perpendicular cylinders from triblock terpolymer polystyrene-*b*-polyisoprene-*b*-polylactide (PS-*b*-PI-*b*-PLA) can be obtained[17]. Perpendicular morphology in which all three blocks of PS-*b*-PI-*b*-PLA are exposed to the surface avoids enthalpically unfavorable contact between PI and PLA and entropically unfavorable looping configurations.[37, 38]

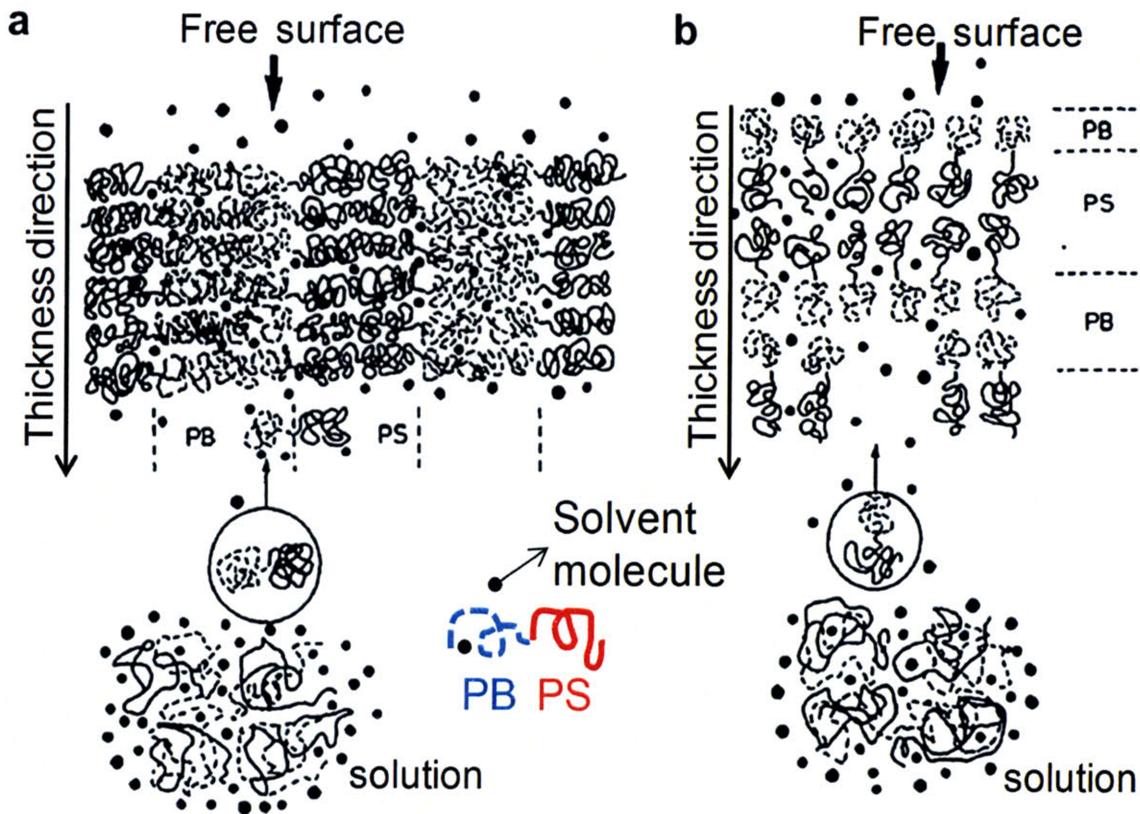

Figure 2-5 Schematic molecular picture of how the solvent molecule evaporates in the situations when the top surface of the polymer is covered with the ordering front of (a) perpendicular lamellae (b) or parallel lamellae.[33]

Pickett et al. has shown by self-consistent-field calculations that the perpendicular orientation can be obtained from a lamellar forming ABC triblock terpolymer if the B block wets both the air surface and also the substrate.[39] Figure 2-6(a) shows a schematic of the bulk morphology of a symmetric triblock terpolymer. In parallel lamellae, as shown in the figure 2-6(b), depending on the symmetric or asymmetric wetting behavior, each substrate wets either the A or the C block. In perpendicular lamellae, as shown in figure 2-6(c), all three component are present at the substrate-film interface. Therefore, in the case of preferential wetting of B block, the perpendicular orientation in which the B block contacts substrate will be adopted since the B block can only be buried inside the film if parallel lamellae form.

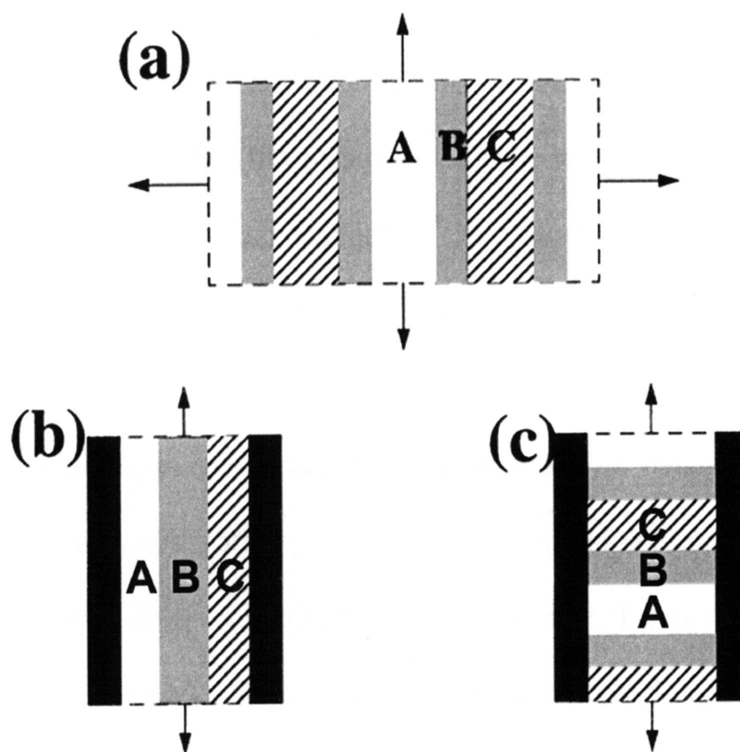

Figure 2-6 Schematic of a symmetric triblock terpolymer (a) in bulk (b) confined lamellar layers with the parallel orientation in which the favorable B component is buried within the layer (c) confined lamellar layers with perpendicular orientation in which at least some of the favorable B component is exposed to the surface. Black regions in (b) and (c) represent confining substrates or surface. [39]

2.4 Nonregular structures from templated block copolymers

Novel structures which are different from those shown in Fig. 2-2 can be generated by combining top-down processes and bottom-up methods such as templated self-assembly of block copolymers. Various 2-D shapes and angles from self-assembling of ternary blends of lamellar forming block copolymers and homopolymers on chemically patterned surfaces have been demonstrated.[40-42] Square arrays of spots and mixtures of parallel and perpendicular cylinders have been fabricated by directed assembly of cylindrical block copolymers using chemically patterned surfaces.[43, 44] Vertical lamellar domains and concentric vertical cylindrical domains with a 16 nm half-pitch and crossbar structures have been reported from confined self-assembly of a diblock copolymer on an electron-beam patterned substrate[45]. With interference lithography-defined templates, concentric rings from a cylindrical diblock copolymer were also obtained.[46] A crossbar structure has also been reported from a directed self-assembled lamellar-forming block copolymer on an e-beam patterned substrate.[47] Graphoepitaxy, in which a block copolymer is physically confined in a lithographically-defined template, is one of the routes to promote long-range-order.[48] For example, by confining a spherical block copolymer into a shallow trench in which the height of the trench wall is designed so that only one single layer of spheres can be accommodated, the row spacing and the diameter of the spherical domains adjusts to conform to the trench width when the trench width falls within $(N\pm0.5)d$. N is the number of rows and d is the equilibrium row spacing. When the trench width is on either upper or lower side of $(N\pm0.5)d$, the system can either create or annihilate a row of polymer domains to accommodate the trench width or keep the number of rows constant and vary the row spacing and domain size depending on the free energy. In this thesis, we present several novel structures such as a single row of elliptical dots and a 3-D structure with a top layer with square symmetry on the top from

templated self-assembly of a spherical diblock copolymer and demonstrate the control of packing orientation by templating triblock terpolymers within a functionalized confining wall.

In summary, in order to use block copolymers for lithographic applications, several ways have been employed to control microdomain orientation. Overall, for perpendicular orientation, one should provide a neutral boundary condition such as using brush layers or solvent annealing or provide a chemically patterned substrate which wets one of the blocks. For triblock terpolymers, an alternative way to promote perpendicular orientation is to apply a boundary condition which is selective to the middle block such as selection of the lowest surface energy block as a middle block. In this thesis, we demonstrate control of the microdomain orientation of triblock terpolymers by solvent annealing and substrate chemistry. In addition, non-bulk structures have been created by templated assembly of a diblock copolymer on chemically patterned or topographical substrates. There are very limited studies on the use of triblock terpolymer thin films which can generate more pattern geometries even without a template. In the following chapters, we present several examples of fabrication of novel structures such as closed-packed rings and square array of dots using triblock terpolymer thin films.

Reference

1. Darling, S. B. *Progress in Polymer Science* **2007,** 32, (10), 1152-1204.
2. Segalman, R. A. *Materials Science and Engineering: R: Reports* **2005,** 48, (6), 191-226.
3. Bates, F. S.; Fredrickson, G. H. *Physics Today* **1999,** 52, (2), 32-38.
4. Zheng, W.; Wang, Z.-G. *Macromolecules* **1995,** 28, (21), 7215-7223.
5. Gido, S. P.; Schwark, D. W.; Thomas, E. L.; do Carmo Goncalves, M. *Macromolecules* **1993,** 26, (10), 2636-2640.
6. Mogi, Y.; Kotsuji, H.; Kaneko, Y.; Mori, K.; Matsushita, Y.; Noda, I. *Macromolecules* **1992,** 25, (20), 5408-5411.
7. Breiner, U.; Krappe, U.; Abetz, V.; Stadler, R. *Macromolecular Chemistry and Physics* **1997,** 198, (4), 1051-1083.
8. Breiner, U.; Krappe, U.; Jakob, T.; Abetz, V.; Stadler, R. *Polymer Bulletin* **1998,** 40, (2), 219-226.
9. Auschra, C.; Stadler, R. *Macromolecules* **1993,** 26, (9), 2171-2174.
10. Krappe, U.; Stadler, R.; Voigt-Martin, I. *Macromolecules* **1995,** 28, (13), 4558-4561.
11. Mogi, Y.; Nomura, M.; Kotsuji, H.; Ohnishi, K.; Matsushita, Y.; Noda, I. *Macromolecules* **1994,** 27, (23), 6755-6760.
12. Shefelbine, T. A.; Vigild, M. E.; Matsen, M. W.; Hajduk, D. A.; Hillmyer, M. A.; Cussler, E. L.; Bates, F. S. *Journal of American Chemical Society* **1999,** 121, 8457-8465.
13. Huckstadt, H.; Goldacker, T.; Gopfert, A.; Abetz, V. *Macromolecules* **2000,** 33, (10), 3757-3761.
14. Brinkmann, S.; Stadler, R.; Thomas, E. L. *macromolecules* **1998,** 31, (19), 6566-6572.
15. Sugiyama, M.; Shefelbine, T. A.; Vigild, M. E.; Bates, F. S. *Journal of Physical Chemistry B* **2001,** 105, (50), 12448-12460.
16. Ludwigs, S.; Boker, A.; Voronov, A.; Rehse, N.; Magerle, R.; Krausch, G. *Nature Materials* **2003,** 2, (11), 744-747.
17. Kubo, T.; Wang, R. F.; Olson, D. A.; Rodwogin, M.; Hillmyer, M. A.; Leighton, C. *Applied Physics Letters* **2008,** 93, (13), 133112-3.
18. Rzayev, J.; Hillmyer, M. A. *Macromolecules* **2005,** 38, (1), 3-5.
19. Morkved, T. L.; Lu, M.; Urbas, A. M.; Ehrichs, E. E.; Jaeger, H. M.; Mansky, P.; Russell, T. P. *Science* **1996,** 273, (5277), 931-933.
20. Thurn-Albrecht, T.; Schotter, J.; Kastle, G. A.; Emley, N.; Shibauchi, T.; Krusin-Elbaum, L.; Guarini, K.; Black, C. T.; Tuominen, M. T.; Russell, T. P. *Science* **2000,** 290, (5499), 2126-2129.
21. Heier, J.; Kramer, E. J.; Walheim, S.; Krausch, G. *Macromolecules* **1997,** 30, (21), 6610-6614.
22. Lin, Y.; Boker, A.; He, J.; Sill, K.; Xiang, H.; Abetz, C.; Li, X.; Wang, J.; Emrick, T.; Long, S.; Wang, Q.; Balazs, A.; Russell, T. P. *Nature* **2005,** 434, (7029), 55-59.
23. Li, X.; Zhao, S.; Zhang, S.; Kim, D. H.; Knoll, W. *Langmuir* **2007,** 23, (13), 6883-6888.
24. Park, S. C.; Kim, B. J.; Hawker, C. J.; Kramer, E. J.; Bang, J.; Ha, J. S. *Macromolecules* **2007,** 40, (22), 8119-8124.
25. U. Jeong; Kim, H. C.; Rodriguez, R. L.; Tsai, I. Y.; Stafford, C. M.; Kim, J. K.; Hawker, C. J.; Russell, T. P. *Advanced materials* **2002,** 14, (4), 274-276.
26. Bang, J.; Kim, B. J.; Stein, G. E.; Russell, T. P.; Li, X.; Wang, J.; Kramer, E. J.; Hawker, C. J. *Macromolecules* **2007,** 40, (19), 7019-7025.

27. Ho, R.-M.; Tseng, W.-H.; Fan, H.-W.; Chiang, Y.-W.; Lin, C.-C.; Ko, B.-T.; Huang, B.-H. *Polymer* **2005,** 46, (22), 9362-9377.
28. Kim, G.; Libera, M. *Macromolecules* **1998,** 31, (8), 2569-2577.
29. Kim, S. H.; Misner, M. J.; Xu, T.; Kimura, M.; Russell, T. P. *Advanced Materials* **2004,** 16, (3), 226-231.
30. Mansky, P.; haikin, P.; Thomas, E. L. *Journal of Materials Science* **1995,** 30, (8), 1987-1992.
31. Turturro, A.; Gattiglia, E.; Vacca, P.; Viola, G. T. *Polymer* **1995,** 36, 3987.
32. van Dijk, M. A.; van den Berg, R. *Macromolecules* **1995,** 28, (20), 6773-6778.
33. Turturro, A.; Gattiglia, E.; Vacca, P.; Viola, G. T. *Polymer* **1995,** 36, (21), 3987-3996.
34. Anastasiadis, S. H.; Russell, T. P.; Satija, S. K.; Majkrzak, C. F. *The Journal of Chemical Physics* **1990,** 92, (9), 5677-5691.
35. Mori, K.; Hasegawa, H.; Hashimoto, T. *Polymer* **1990,** 31, (12), 2368-2376.
36. Huang, E.; Pruzinsky, S.; Russell, T. P.; Mays, J.; Hawker, C. J. *Macromolecules* **1999,** 32, (16), 5299-5303.
37. Khanna, V.; Cochran, E. W.; Hexemer, A.; Stein, G. E.; Fredrickson, G. H.; Kramer, E. J.; Li, X.; Wang, J.; Hahn, S. F. *Macromolecules* **2006,** 39, (26), 9346-9356.
38. Wim, H. d. J.; Peter, L.; Ian, W. H.; David, V.; Jan Skov, P.; Kristian, K.; Roger, S.; Paul van, H.; Georges, H. *Journal of Physics II* **1993,** 3, (1), 139-146.
39. Pickett, G. T.; Balazs, A. C. *Macromol. Theory Simul.* **1998,** 7, (2), 249-255.
40. Stoykovich, M. P.; Muller, M.; Kim, S. O.; Solak, H. H.; Edwards, E. W.; de Pablo, J. J.; Nealey, P. F. *Science* **2005,** 308, (5727), 1442-1446.
41. Stoykovich, M. P.; Kang, H.; Daoulas, K. C.; Liu, G.; Liu, C.-C.; de Pablo, J. J.; Müller, M.; Nealey, P. F. *ACS Nano* **2007,** 1, (3), 168-175.
42. Kang, H.; Craig, G. S. W.; Nealey, P. F. *J. Vac. Sci. Technol. B* **2008,** 26, (6), 2495-2499.
43. Park, S.-M.; Craig, G. S. W.; La, Y.-H.; Solak, H. H.; Nealey, P. F. *Macromolecules* **2007,** 40, (14), 5084-5094.
44. Kim, S. O.; Kim, B. H.; Meng, D.; Shin, D. O.; Koo, C. M.; Solak, H. H.; Wang, Q. *Advanced Materials* **2007,** 19, (20), 3271-3275.
45. Toru Yamaguchi; Yamaguchi, H. *Advanced materials* **2008,** 20, (9), 1684-1689.
46. Jung, Y. S.; Jung, W.; Ross, C. A. *Nano letters* **2008,** 8, (9), 2975-2981.
47. Kim, H.-C.; Rettner, C. T.; Sundstrom, L. *Nanotechnology* **2008,** 19, (23), 235301.
48. Cheng, J. Y.; Mayes, A. M.; Ross, C. A. *Nature Materials* **2004,** 3, (11), 823-828.

Chapter 3 Templated self-assembly of a spherical PS-*b*-PFS diblock copolymer

3.1 Introduction

Block copolymers, which consist of two immiscible polymer chains bonded together, form self-assembled periodic structures in the bulk with geometries that depend on the molecular weight and volume fractions of the two blocks.[1, 2] By control of the self-assembly of block copolymers with a template, a rich variety of hierarchical structures can be made, depending on the polymer morphology, polymer-surface interaction, and the commensurability between the polymer period and the size of the template.[3-13] These structures have been used as versatile building blocks for nanofabrication. The case of spherical and cylindrical morphology BCPs is particularly interesting because of the possible lithographic applications of these polymers in forming arrays of discrete metal dots for data storage or other applications. Both spherical and cylindrical morphology polymers have been templated in order to create two-dimensional arrays consisting of multiple rows of close-packed domains,[10-17] but to date there has been very limited work[14] on the formation of one-dimensional arrays of block copolymer domains. Naito et al. has shown a single row of poly(methyl methacrylate) (PMMA) spherical domains from templated assembly of a diblock copolymer in a narrow groove.[14] However, control of the ellipticities of these structures and template a spherical BCP in a 3D confinement have not been demonstrated.

Here we present a study of one- and three-dimensional nanostructure arrays by templating a spherical morphology block copolymer, polysyrene-*b*-polyferrocenyldimethylsilane (PS-*b*-PFS), within a narrow groove (for 1-D study) and a V-shaped groove (for 3-D study). PS could be selectively etched away by oxygen plasma and PFS forms a good lithographic mask for subsequent pattern transfer.

3.2 Experimental Methods

3.2.1 Fabrication of topographical substrates

Novel geometrical structures can be obtained by using a topographical substrate to template the self-assembly of a block copolymer. Topographical substrates with large-area periodic structures, such as a grating or an array of holes, were made by interference lithography. Figure 3-1(a) illustrates a schematic of a Lloyd's Mirror interference lithography system.[18] A coherent helium-cadmium laser beam with a 325 nm-wavelength passes through a spatial filter and interferes with a second coherent beam which is reflected from the mirror. A standing wave pattern is thus generated at which two beams intersect and record a grating image in the photoresist. Temporal coherence is achieved by the choice of a laser with long coherent length. Spatial coherence is done by focusing the beam on a pin hole. An array of holes or dots can be produced with a double exposure instead of one exposure for a grating. The periodicity of the exposed grating can be tuned from 180 nm to 1500 nm by varying the wavelength of light (λ) and the half angle between the two beams (θ), as shown in Fig. 3-1(b), according to the following equation:

$$Po = \frac{\lambda}{2\sin(\theta)}$$

Substrates containing shallow grooves were made by the following method. Initially, a trilayer resist stack[20] consisting of antireflective coating/silica/photoresist was deposited onto a Si wafer that had been coated with 30 nm of silicon nitride or 60 nm of silica. Positive resist PFI-88 was used to create gratings with wide trench with narrow mesa and negative resist PS4 was used to create gratings with narrow trench with wide mesa and an array of holes. For a positive

resist, the region where received exposure dose is higher than threshold value will dissolve in the developer completely. The period of the grating was varied between 200 and 500 nm by changing the angle of incidence of the expanded laser beam on the substrate and an adjacent mirror. Achromatic interference lithography was employed to pattern 100 nm periodic gratings.[21]

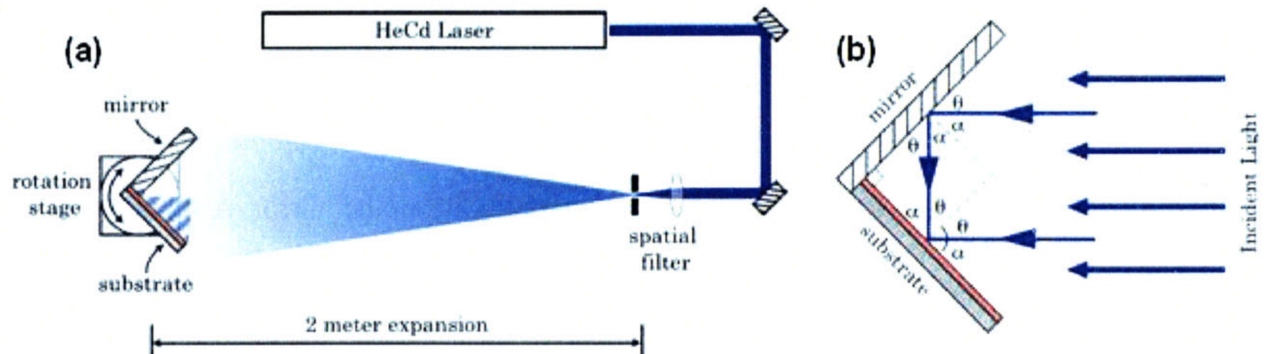

Figure 3-1 Schematics of (a) Lloyd's mirror set up for interference lithography (b) angle-of-incidence on the substrate for the direct and reflected beams.[19]

Figure 3-2 shows the process flow for fabrication of a topographical template. The periodic grating structure in the CD 26 developed photoresist was transferred through the nitride (or oxide) layer by a series of reactive-ion-etch (RIE) steps which were performed on a Plasma Therm Model 790 plasma etcher. Silica in the trilayer resist stack, which serves as a hard mask to etch thick ARC layer, was etched by CF_4-RIE at power of 100W and 10 mtorr of CF_4. O_2+He-RIE performed at 300W power had good selectivity for etching thick ARC layer with a silica mask. Subsequently, the pattern was transferred into underlying nitride (or oxide) layer by another CF_4-RIE process. Finally, after RIE etching, the remaining trilayer resist stack was removed by a resist stripper, EKC265, at 70 °C, followed by oxygen plasma. A silicon nitride grating on the top of silicon is formed as shown in Fig. 3-2.

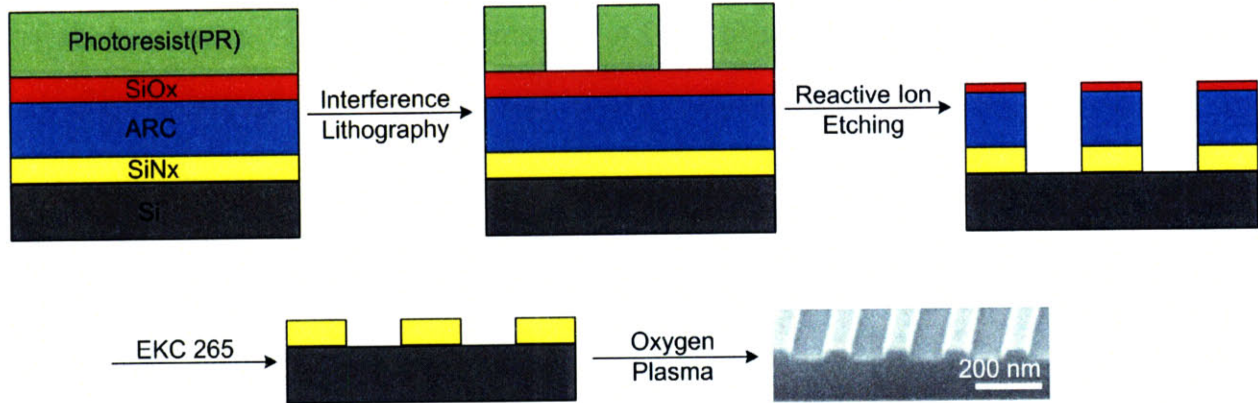

Figure 3-2 Schematic of a step-by step procedure for making a topographical substrate.

3.2.2 Non- periodic structures-narrow channels

This Isolated 1D arrays were made by confining a block copolymer within a topographical template consisting of narrow channels made from a hydrogen silsesquioxane(HSQ) resist layer patterned using electron-beam lithography. These narrow channels were made by Dr. Feng Zhang in Professor Hank Smith's group at Massachusetts Institute of Technology. The channel width was 30-80 nm with line edge roughness of 2 nm. The cross-sectional shape shows rounding of the inner angles of the rectangular grooves, with a radius of curvature of 10-20 nm.

3.2.3 V-shaped grooved substrates

3D templates consisting of V-shaped grooves were formed by the anisotropic etching of a (100) Si wafer. The wafer was first patterned with a grating of nitride, as shown in Fig. 3-2, and then dipped into buffered hydrofluoric acid, immediately prior to etching the silicon in 25% KOH at 40 °C with ultrasonic agitation. After the silicon etch, the nitride mask was removed by hydrofluoric acid solution and the samples were finally cleaned by oxygen ashing. The resulting

V-shaped grooves had widths varying from 50 to 290 nm (Figure 3-3a). A native oxide layer (~2-3 nm) was present on the groove walls.

3.2.4 Preparation of block copolymer thin films

Toluene solutions(1-1.5%w/v) of the a spherical-morphology polystyrene (PS)-*block*-polyferrocenyldimethylsilane (PFS) block copolymer, with a molecular weight of 32 kg/mol for PS and 10 kg/mol for PFS, were spin coated onto narrow channels or grooved substrates. The diblock copolymer used in the experiment described in this chapter was synthesized by Professor G. J. Vancso's group at University of Twente. The thickness was controlled by spin speed and determined by ellipsometer. The thin films were then annealed under vacuum at 140°C for 72 hrs to facilitate microdomain segregation. During annealing, the BCP flows into the grooves, resulting in a planar film that partially or completely fills the grooves (Figure 3-3b), leaving the mesas between the grooves free from polymer.

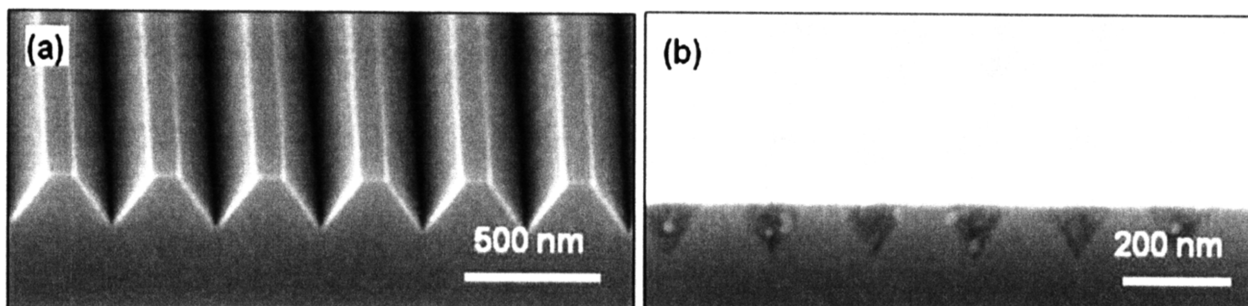

Figure 3-3 SEM images of (a) V-shaped groove anisotropically etched in a (100) silicon substrate with 400 nm period and (b) a PS-PFS polymer film spun on V-shaped grooves and then annealed at 140 °C for 72 h. The polymer flows to fill the grooves leaving a planar surface.

In the case of one-dimensional nanostructure arrays, a microphase-separated thin film formed within the channels consisting of a monolayer of PFS domains in a PS matrix,

surrounded by a thin brush layer of the copolymer with PFS preferentially wetting the channel surfaces. In the case of 3-dimensional packing, the polymer fills the entire volume of V-grooves with multilayers of PFS domains in a PS matrix. To reveal the arrangement of the PFS spheres in PS/PFS on the top surface or the cleaved cross section, the sample was subjected to deep- UV exposure before cleaving and the PS matrix was then partially etched by oxygen plasma. Additionally, the domain arrangement at the flat surfaces of the grooves could be revealed by applying hot melt glue to the top surface of the sample, then etching away the entire Si substrate in 25% KOH solution to leave triangular prisms of polymer attached to the glue that could be imaged from the side.

3.3 Self-Assembled One-Dimensional Nanostructure Arrays[22]

One-dimensional (1D) chains of regularly spaced nanoparticles exhibit unique transport properties and have been proposed for applications such as plasmon waveguides, magnetic logic, quantum cellular automata, and Coulomb blockade devices.[23-26] Controlling the size, spacing, and aspect ratio of the nanoparticles is critical for the function and performance of these devices. For example, the shape and size of metal particles profoundly affect their plasmonic properties, and the plasmon resonance red shifts for increasing aspect ratio,[27] while in magnetic nanoparticles, even a modest ellipticity can provide a significant shape anisotropy, determining the easy magnetization direction. As an example, a thin film polycrystalline single-domain cobalt ellipse with aspect ratio 1.5 would have an in-plane switching field of order 1000 Oe, whereas a circular particle would have ideally zero switching field, thus the magnetic anisotropy can be tailored over a wide range via the particle shape, as required in applications such as quantum cellular automata.[25] Many fabrication methods incorporating self-assembly processes have been used to make nanoparticle chains, for example, sphere-to-string transitions in nanoparticle

micelles,[28] or DNA templating of metallic nanoparticles,[29-31] but the dimensional control of these 1D self -assembled arrays is limited, especially with regard to controlling the aspect ratio of the nanoparticles. To address this limitation, we demonstrate here that diblock copolymers may be template in order to create 1D arrays of nanostructures with uniquely independent control over both the periodicity of the array and the aspect ratio of the nanoparticles. These well controlled arrays can then serve as templates for device fabrication, for example, by transferring the self-assembled block copolymer pattern into a functional thin film by etching.[32] Good fidelity of pattern transfer from a block copolymer array into a functional layer has been demonstrated, for example, silicon nitride hole and dot arrays,[33] silica pillar arrays,[20] and magnetic dot arrays,[14, 34] among other materials, have been patterned. Moreover, block copolymer patterning has already been integrated into semiconductor device manufacturing,[3, 35, 36] and developments of this process may have a dramatic impact on future nanoscale device fabrication.[2, 4, 37]

3.3.1 Effect of confinement width on a single row of PFS domains

In an unconfined film of thickness approximately equal to the domain spacing, the PFS forms a close-packed monolayer of spherical domains with a row spacing, d_0, of 24.8 nm and center-to-center spacing of $p_0 = d_0 2/\sqrt{3} = 28.6$ nm.[3, 10] In confined channels of width approaching d_0, a single row of ordered PFS domains forms as shown in Figure 3-4. The confinement width of the channel, W, is defined as the channel width minus the thickness of the brush layers and represents the space available to accommodate the row of PFS domains and their surrounding PS matrix. A single row of PFS domains forms when $0.6 < W/d_0 < 1.5$. Significantly, the shapes of the PFS domains in plan view depend on the template width: at $W/d_0 \sim 1.0$, the domain projections are circular, for $W/d_0 > 1.0$ they are elongated perpendicular to the channel, and for $W/d_0 < 1.0$ they are elongated parallel to the channel (Figure 3-4).

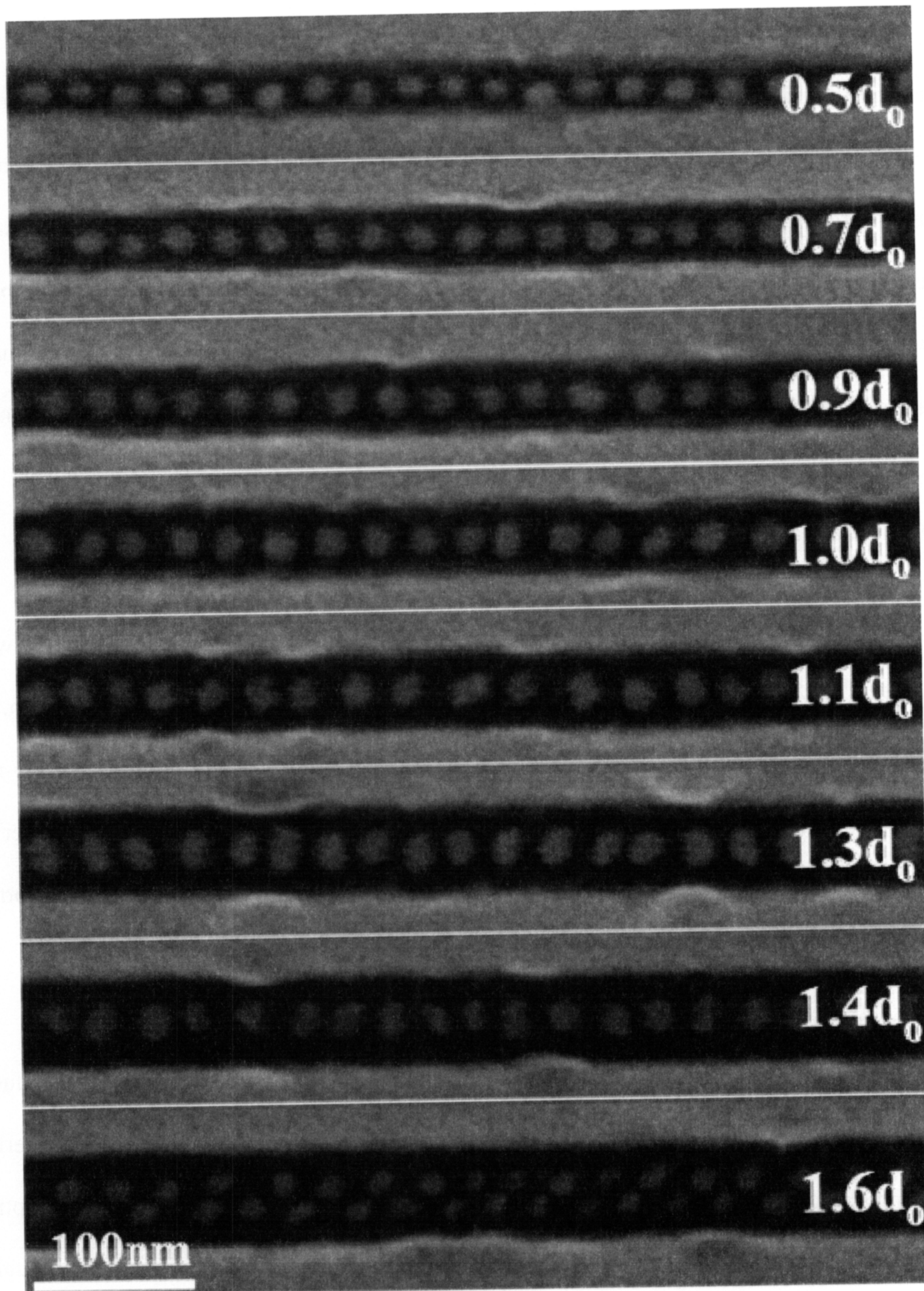

Figure 3-4 A composite image of PFS block copolymer domains within channels of different confinement widths W. A single row of spheres forms for $0.6 < W/d_0 < 1.5$, where d_0 is the equilibrium row spacing of this block copolymer.

Domain dimensions were measured from the scanning electron microscopy images by fitting each domain to an ellipse and measuring the projected major and minor axes. Figure 3-5(A) shows that the diameter of the PFS domains, measured perpendicular to the channel, increases with the groove width, while the diameter parallel to the channel remains constant. Figure 3-5(B) shows the aspect ratio of the domains vs W/d_0, with a best-fit line with a slope of 0.63 ± 0.03 (for $W/d_0 > 0.65$). By contrast (Figure 3-5(C)), the period of the 1D array remains constant and equal to p_0 within the error of the measurement, indicating that the lateral period is independent of the elliptical distortion transverse to the template induced by the incommensurability between W and d_0.

To assess the out-of-plane domain dimensions, crosssectional images of domains were acquired by sectioning then etching an additional sample perpendicular to the channel length. An example is shown in Figure 3-6(A) for a channel of width close to the one-row to two-row transition. The domains within the channel are clearly elongated compared with the spherical domains outside the channel but have a similar thickness, suggesting that the elliptical distortion is uniaxial.

3.3.2 Analysis of elliptical distortion in 1D arrays

There has been previous experimental and modeling work on the confinement-induced distortion of lamellar and cylindrical morphology block copolymers,[38-42] but spherical morphology block copolymers have been less widely studied. The confinement-induced elliptical distortion of spherical block copolymer domains has not been reported experimentally, though it was predicted by an analytical model[43] and self-consistent field theory.[44] To understand the origin of the elliptical distortion in these 1D arrays, we compared our experimental results to a

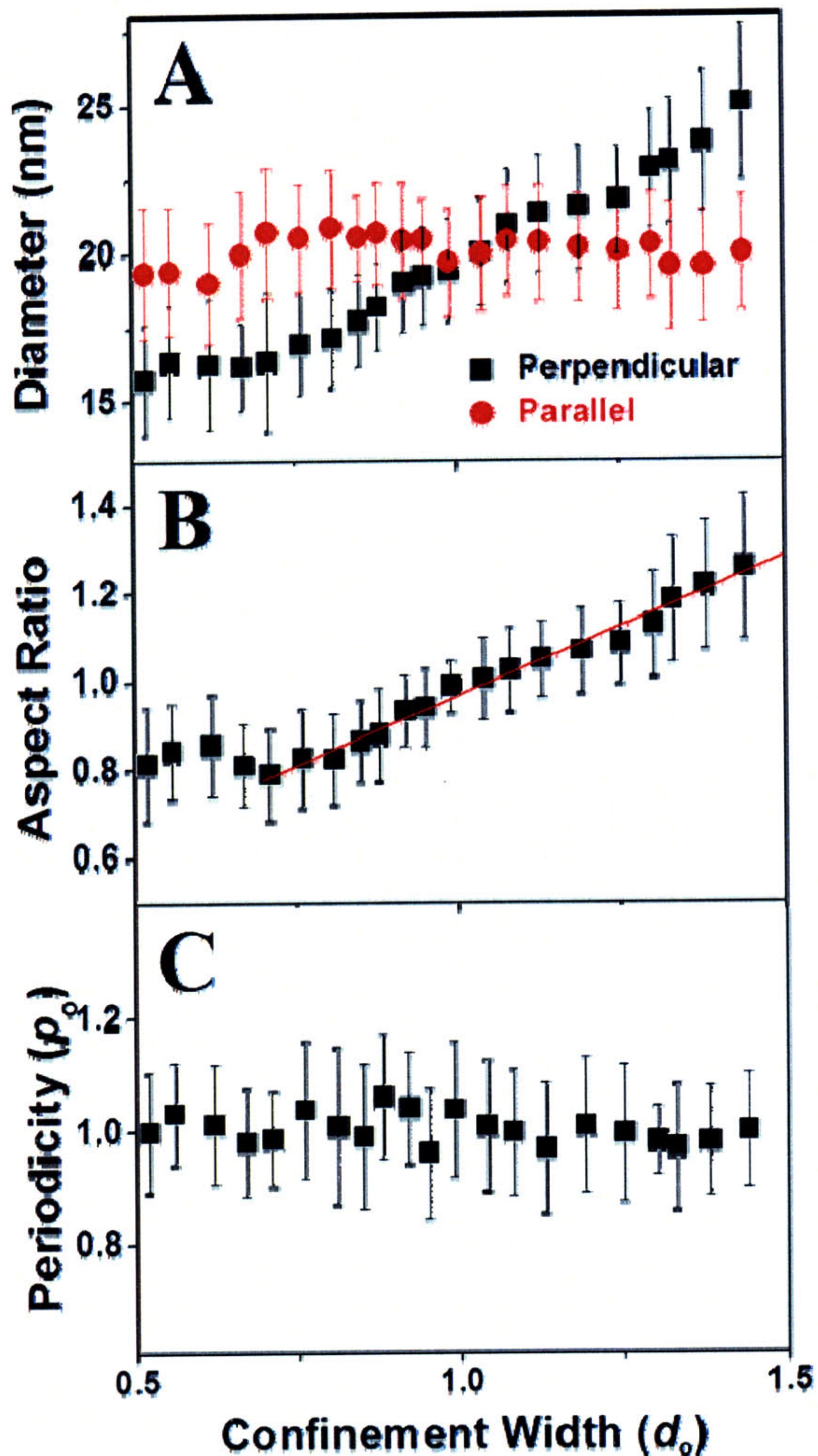

Figure 3-5 (a) The domain dimensions parallel and perpendicular to the channel (b) The aspect ratio of the domains calculated from the data of (a), with a linear best fit to the data for W/d_0 in the range 0.65- 1.5. (c) The periodicity of the 1D array is equal to p_0, the center-to-center spacing of the unconfined block copolymer, and independent of confinement width.

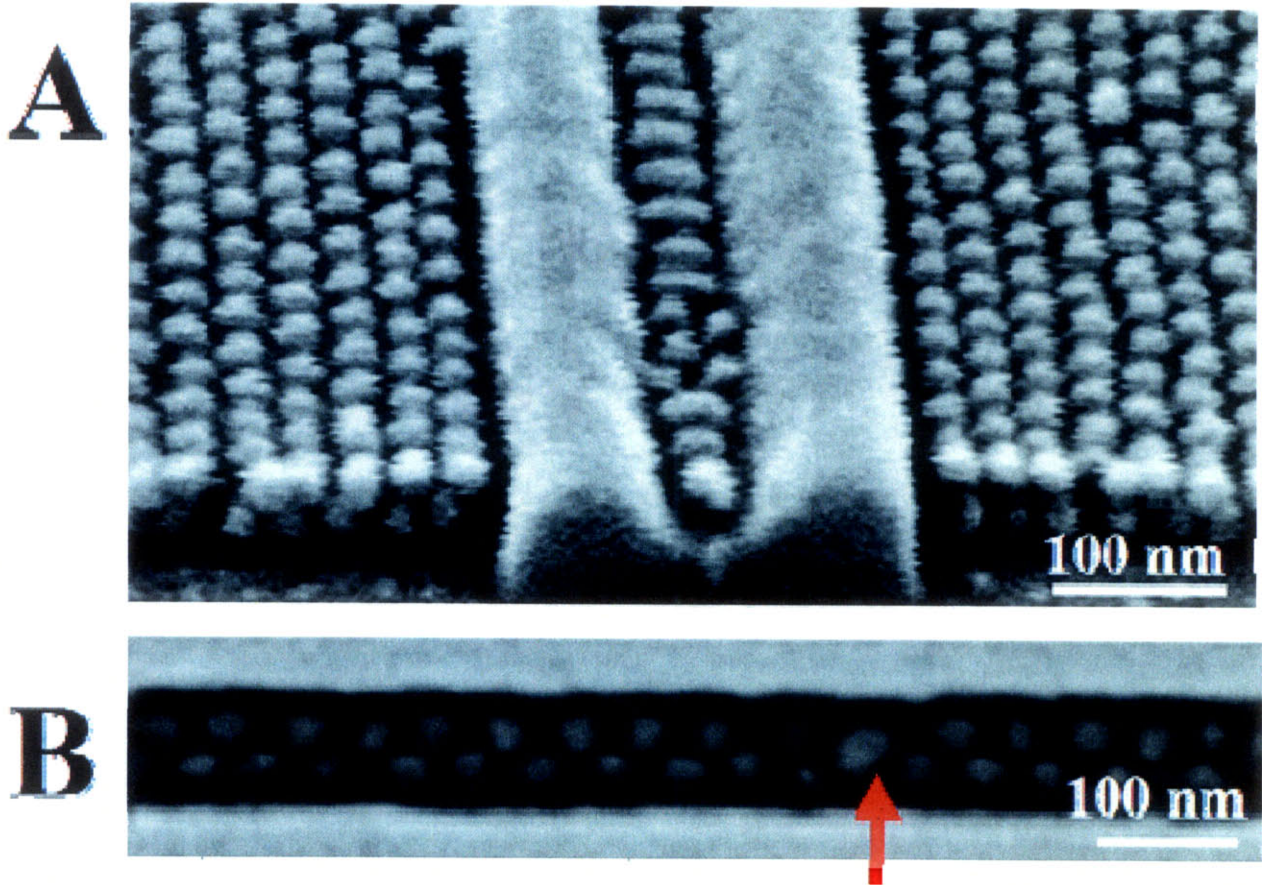

Figure 3-6 (a) A tilted view of a sample with channel width near the one-row to two-row transition, illustrating the comparison between the out-of-plane dimensions of confined and unconfined domains. A small region with two-row arrangement can be seen. (b) A section of a channel with W/d_0 = 1.5 showing a one-row domain (indicated) that tilts to adapt to the symmetry of its two-row neighbors.

model by Pereira for the strain-induced elliptical distortion of spherical domains based on the unit cell approximation.[43] The model gives the shape-dependent free energy per chain in the strong segregation limit (large χN, where N is the number of segments in the chain and χ the Flory-Huggins interaction parameter) when the spherical domain is distorted into an oblate (compressed) or prolate (stretched) ellipsoid. The model assumes a spherical boundary for the Wigner-Seitz cell that becomes ellipsoidal when subjected to uniaxial strain. The free energy is a

sum of the interfacial and strain energies, computed from the additive contributions of each wedge of the ellipsoidal cell.

For prolate distortion of the domain

$$\frac{F(\lambda.e^2)}{F_0} = \frac{2}{3}\frac{1}{2\lambda}\left(1 + \frac{\sin^{-1}(e)}{e(1-e^2)^{1/2}}\right) + \frac{1}{3}\lambda^2\left(1 - \frac{2e^2}{3}\right)$$

where

$$e = \left(1 - \frac{1}{A^2}\right)^{1/2}$$

and for oblate distortion

$$\frac{F(\lambda.e^2)}{F_0} = \frac{2}{3}\frac{1}{2\lambda}\left(1 + \frac{1-e^2}{2e}\ln\left(\frac{1+e}{1-e}\right) + \frac{1}{3}\lambda^2\left(\frac{3-e^2}{3(1-e^2)}\right)\right)$$

where

$$e = (1 - A^2)^{1/2}$$

F is the free energy per chain in the ellipsoidal domain, F_0 is the free energy in the unstrained spherical domain, (λ - 1) represents the strain, A is the aspect ratio of the ellipsoid (dimension in strained direction/dimension perpendicular to strain), and e is the eccentricity of the ellipsoid. The model was applied to the 1D arrays of PFS domains by setting $\lambda = W/d_0$ and by calculating the ratio F/F_0 for different values of the confinement width W (Figure 3-7A). For λ=1, the system has lowest energy when the domains are spherical (A =1), and its free energy rises as the aspect ratio deviates from 1. Other values of λ similarly exhibit a unique aspect ratio for

which the free energy is minimized, and these optimized aspect ratios are plotted in Figure 3-7B vs channel width. Also shown in this figure is the corresponding value of λ. These results show that the domains distort ellipsoidally to fit within the channel width such that their aspect ratio is equal to the normalized channel width, and there is no change in spacing parallel to the channel.

It is significant that both the data and the model shown that the spheres adopt their bulk equilibrium dimension in the direction normal to the imposed confinement. This result reflects the Gaussian coil nature of the copolymer chains, characterized by decoupled random-walk trajectories in the x, y, and z directions.

With the bulk period in the unconfined direction, the aspect ratio of the ellipses is necessarily fixed to vary linearly with the imposed strain λ, as shown for the data and model in Figures 3-5C and 3-7B, respectively. The discrepancy in the slopes of these two plots may reflect deviations from a true ellipsoidal geometry, domain tilting, or thickness variations in the adjacent brush layer that engender less extreme entropic penalties than implied in the model, which cannot account for such effects. For confinement widths W/d_0 below ~0.6 and above 1.5, the morphology of the confined film changes, giving lower and upper limits for the formation of the 1D array. At the lower limit, the domains transform to hemispheres protruding from the brush layers in an alternating fashion from opposite sides of the channel, in accord with theoretical predictions.[43] At the upper limit, regions consisting of two rows of domains start to appear. The major axes of the remaining one-row domains are oriented at 60° to the groove edge, to optimize packing with their two-row neighbors. For example, there is a region of five domains forming a two-row arrangement between single-row domains in Figure 3-6A, and a single-row domain can be seen within a two-row arrangement in Figure 3-6B. For grooves with two or more rows of domains, the domain shapes show little or no elliptical distortion;[10] they form regular close-

packed arrays which do not provide the opportunity to control the domain aspect ratio that we have shown in single-row arrays.

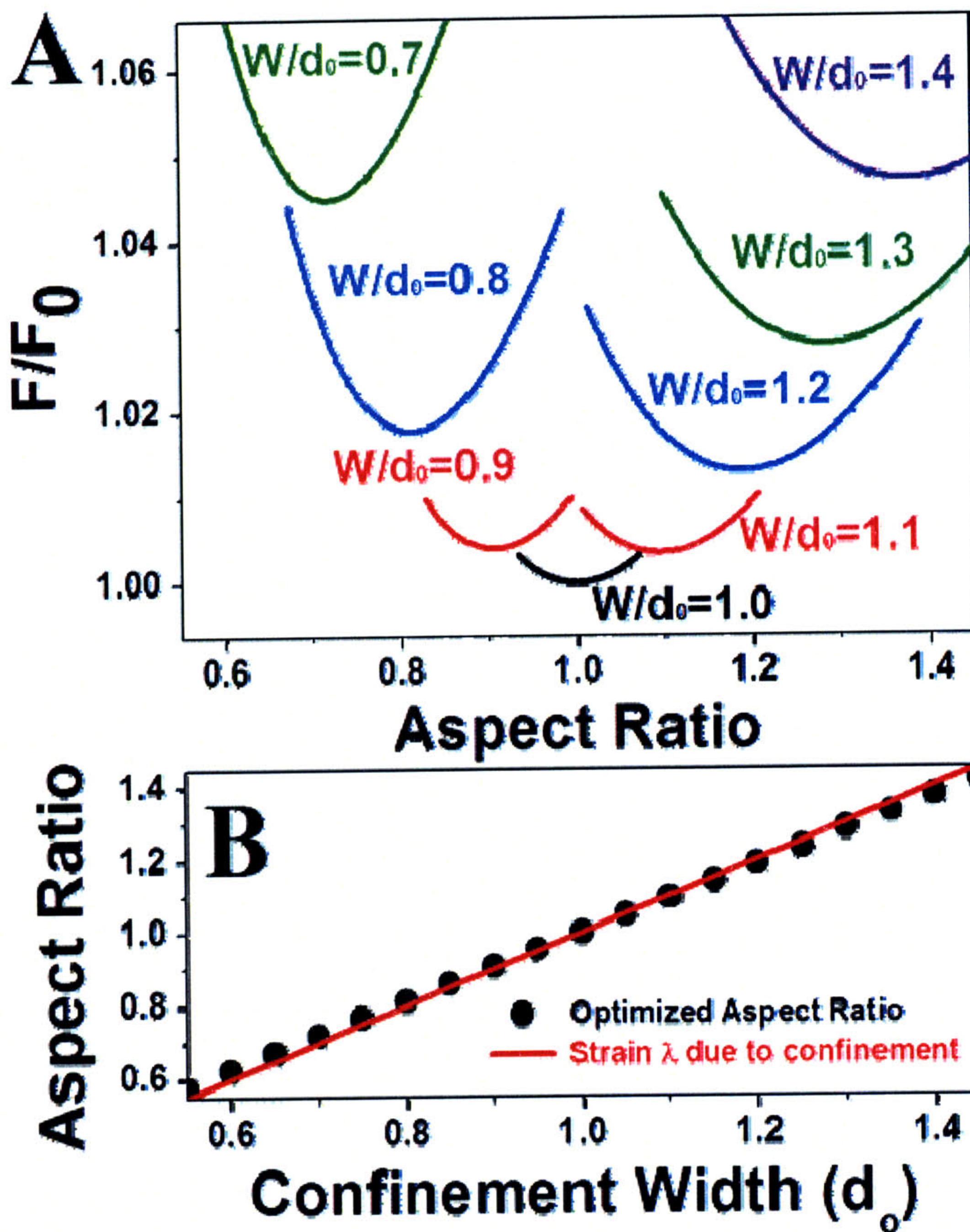

Figure 3-7 (a) Energy per chain of the confined polymer as a function of aspect ratio of the domains. Each plot corresponds to a different confinement width. (b) The optimum domain aspect ratio that minimizes the free energy at a given confinement width increases linearly with confinement width. The solid line shows the corresponding values of λ, which are very similar to the aspect ratio values.

In summary, 1D arrays form in this block copolymer system over a wide range of channel widths, $0.6 < W/d_0 < 1.5$, despite the *extreme incommensurability* between channel width W and the equilibrium row spacing d_0. The ellipticity of the domains, and the orientation of their major axis either parallel or perpendicular to the length of the array, is controlled by W/d_0, as a result of the system's tendency to adopt the bulk equilibrium spacing in the direction normal to confinement. This method allows a linear feature, which is relatively easy to pattern by lithography, to be converted into an array of dots, a structure that is much harder to pattern. In addition, the ellipticity can be varied continuously within an array by changing the channel width. This method augments traditional fabrication methods by enabling template formation of sublithographic, thermodynamically stable features of controlled shape.

The uniform size and morphology of the rows of ellipsoidal domains offer the promise of high-yield nanofabrication compared to other proposed self-assembly processes for making 1D arrays. For example, 1D chains of DNA-mediated gold nanoparticle arrays have a wide distribution of interparticle distances[29] compared to the interdomain spacings of $(1.0 \pm 0.1)p_0$ observed here, where p_0 is the equilibrium center-to-center domain spacing. The domain size, ellipticity, and period in 1D block copolymer arrays can be tuned *independently* through judicious choice of copolymer block molecular weights and template channel width, enabling the precise patterning of 1D arrays on the nanoscale using block copolymer lithography.

3.4 Three-Dimensional Self-Assembly of Spherical Block Copolymer Domains into V-Shaped Grooves[45]

A spherical BCP templated in a 3D confinement demonstrates the formation of a f.c.c. close-packed sphere array, with a top surface that shows a square symmetry that may be useful in fabricating square arrays of functional nanostructures. Such arrangements do not occur in

monolayers of spherical domains, which are restricted to hexagonal symmetry, or in bulk spherical BCPs, which typically pack in a b.c.c. structure.

3.4.1 The geometrical packing of the PFS spheres within the V groove

A three dimensional array can be made by packing a spherical diblock copolymer in V-shaped grooves. The grooves are formed by the (111) planes of the Si and have an intersection angle of 70.6°. An fcc sphere array can be accommodated within such a groove as shown in Figure 3-8a and b, where the (111) and (11-1) planes of the sphere array are parallel to the two groove walls, the (001) plane is parallel to the substrate, and the (1-10) plane is perpendicular to the length of the groove. Figure 3-8b shows that the top surface of the fcc sphere array has a square symmetry, whereas in the cross section, layers of spheres can be identified parallel to the surface, corresponding to parallel (001) planes. Alternatively, for bcc packing in the same V-shaped groove, if the closest-packed plane, (110), lies parallel to a groove wall (Figure 3-8c), then the top surface of the array will have a distorted hexagonal arrangement (Figure 3-8d).

Figure 3-9 shows a top view and cross section of an etched sphere array. The top surface shows a square symmetry in the sphere packing, and the cross-section shows 11 rows of spheres parallel to the surface of the substrate. The arrangement is consistent with the fcc packing shown in figure 3-8a and b. For this polymer, the average center-to-center distance in a close-packed monolayer of spheres is p_0 = 28.6 nm and the spacing between two parallel close-packed rows in a monolayer of spheres is d_0 = 24.8 nm.[9] On the basis of 3D fcc packing, we therefore expect a spacing of $t_0 = \sqrt{2}d_0/\sqrt{3}$= 20.25 nm between the projected rows of spheres in the cross-sectional image of the array in the groove. This is in good agreement with the average interlayer spacing (excluding the top layer) of 20.5 nm measured from the cross-sectional image, figure 3-9b.

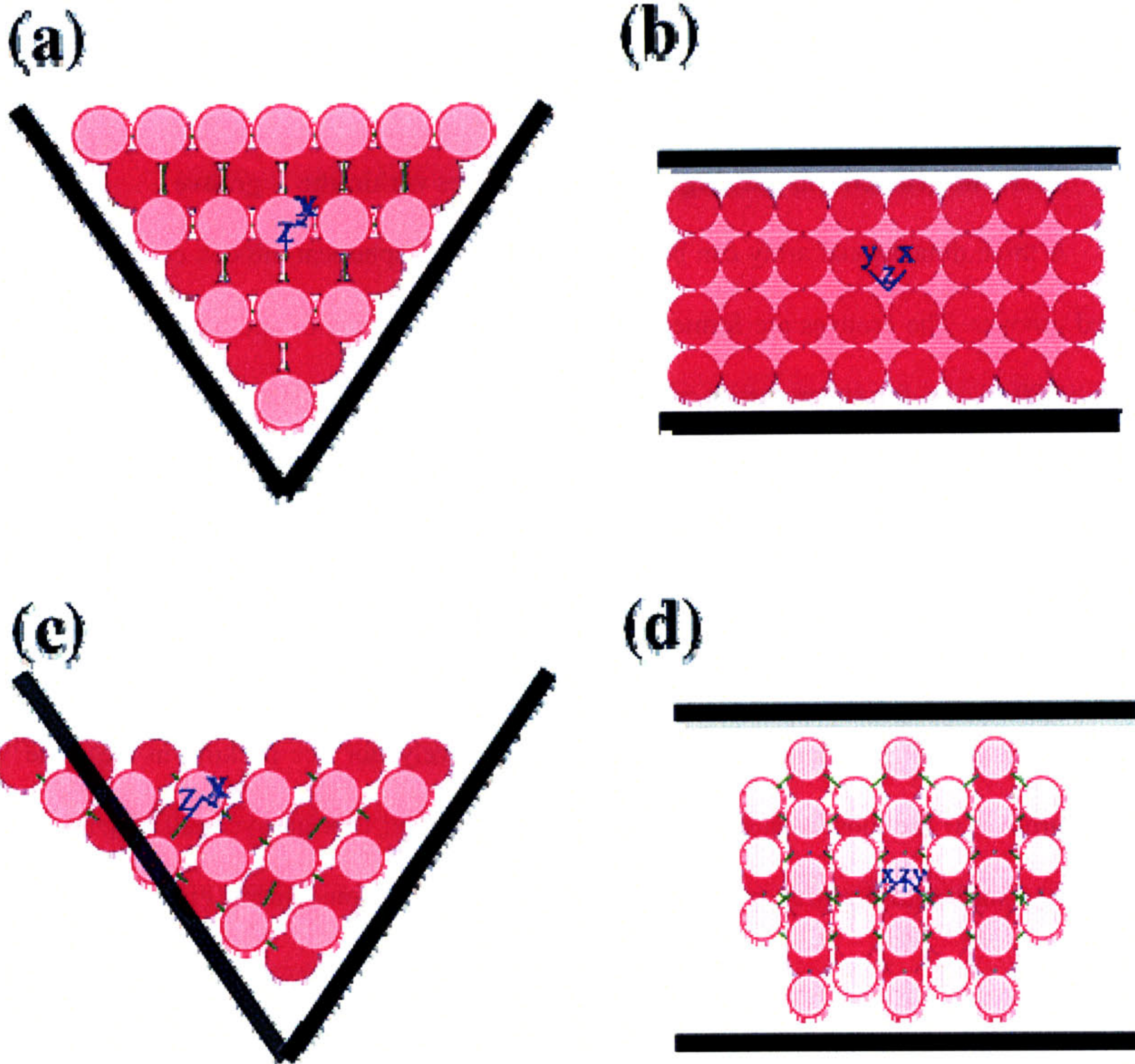

Figure 3-8 Schematic of the packing of spheres within a V groove. (a) Cross section of fcc packing with the (111) close-packed planes parallel to the groove surfaces; (b) top view of fcc packing; (c) cross-section of bcc packing with the (110) closest-packed plane parallel to one groove surface (shown dark); (d) top view of bcc packing.

This confirms that the PFS spheres are packed in an fcc arrangement. Figure 3-9c shows a side view of the polymer in a groove after removal of the substrate, imaged at an angle from the normal to show one surface of the polymer prisms. The hexagonal arrangement of domains

that can be seen on the surfaces of the polymer (i.e., in contact with the original groove surfaces) is consistent with the (111) planes of fcc packing.

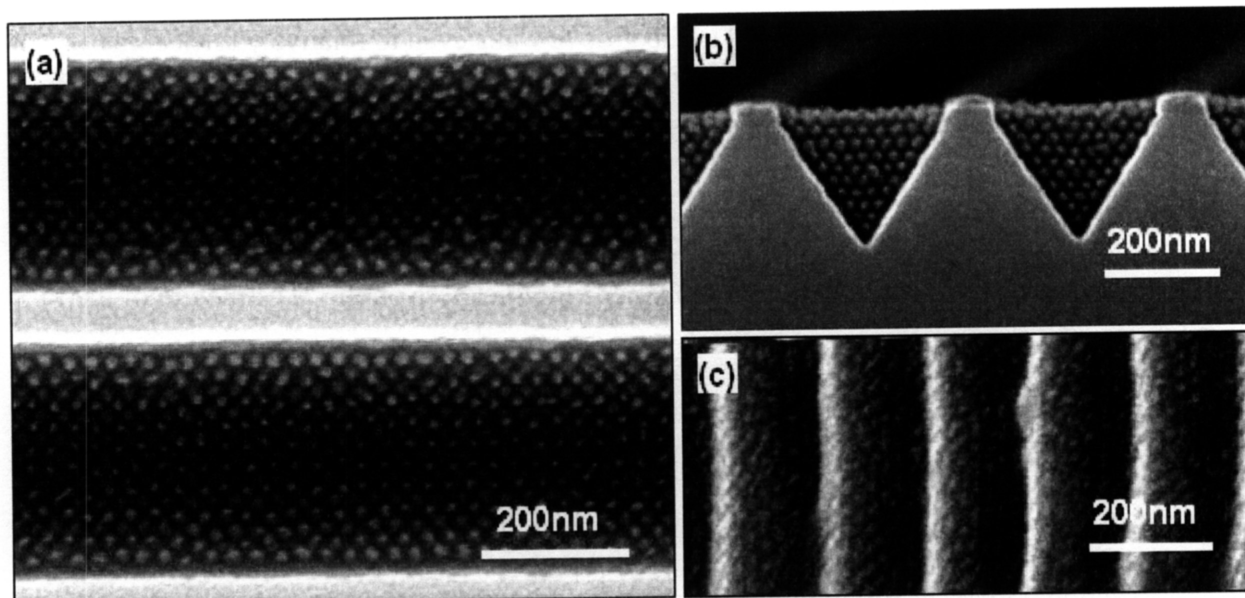

Figure 3-9 SEM images of PS-PFS films in V grooves after 72 h annealing and etching. (a) Square packing of spheres is visible in the top view; (b) the same sample as that in part a in a crosssectional view showing a sphere array with 11 rows; (c) the polymer directly adjacent to the groove surfaces shows a hexagonal arrangement. The contrast is poor because the PS matrix has not been removed, but the PFS spheres can be seen as lighter dots. The vertical white lines are the apexes of the prism-shaped polymer regions remaining after dissolving the substrate. The sample is tilted so only one set of prism faces is visible.

Previous work has shown that spherical-morphology block copolymers form bcc structures in the bulk, with fcc expected only under very limited conditions of composition, segment interaction parameter, and chain length.[46] However, close packing is typically found in thin films consisting of a monolayer of spheres.[47] In films with two or three layers, close-packing has also been found,[48] but in films with a larger number of layers, bcc packing has been observed

with the (110) plane parallel to the substrate.[49, 50] For example, in poly- (styrene-*b*-2-vinylpyridine), films with six layers of spheres showed a bcc structure.[49] In the case studied here, it is likely that the geometrical constraint of the V grooves would stabilize the fcc arrangement with the (111) planes of the array parallel to the groove walls even to relatively thick films.

3.4.2 The effect of polymer film thickness on the 3D structure of the PFS sphere array

We will now describe the effect of polymer film thickness on the 3D structure of the PFS sphere array. For the smallest V grooves with the thinnest films, a single row of spheres was formed in the groove as shown in Figure 3-10a. In this sample, the film thickness, which is measured from the intersection point of the two sides of the V groove to the top of the sphere in the cross-sectional view, is 36–40 nm. A 73-nm-thick film shows a two-layer arrangement where the second layer of spheres is offset from the spheres in the first row and has a square arrangement (Figure 3-10b). Figure 3-10c–e show arrangements of 3, 4, and 5 layers, respectively, formed in deeper grooves. The top layer of spheres again has a square arrangement, but its sphere diameter is often smaller than that of the lower layers. In addition, the spacing between the top layer of spheres and the layer immediately below differs from the average spacing. The same behavior is seen in thicker films (Figure 3-9); for example, films 216–229 nm thick consist of 10 layers of spheres, whereas films ~230–240 nm thick show an additional layer of smaller spheres, and films ~240–255 nm thick consist of 11 layers of approximately uniform spheres.

We also observe in some cases the existence of a close-packed sphere arrangement on the top surface of the V groove, as shown in Figure 3-11. In this sample, cross-sectional images

indicate that the lower layers are close-packed, but the top layer of spheres is no longer epitaxial with the underlying structure and consists of 12 rows of spheres. The top layer packing is identical to that seen in a close-packed monolayer of spheres templated by a shallow, vertical-walled trench.[9, 10]

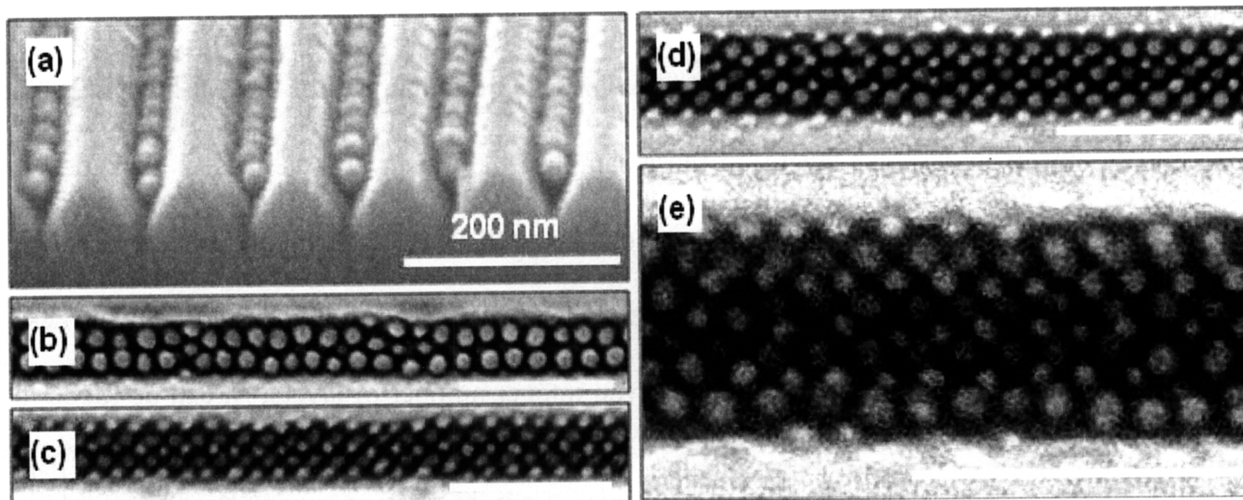

Figure 3-10 SEM images of PS-PFS films with various thicknesses in V grooves, after 72 h annealing and etching. (a) Ordered arrays of PFS domains with $N = 1$, where N is the number of (100) layers of polymer spheres in the groove; (b) $N = 2$; (c) $N = 3$; (d) $N = 4$; (e) $N = 5$ layers. All scale bars represent 200 nm.

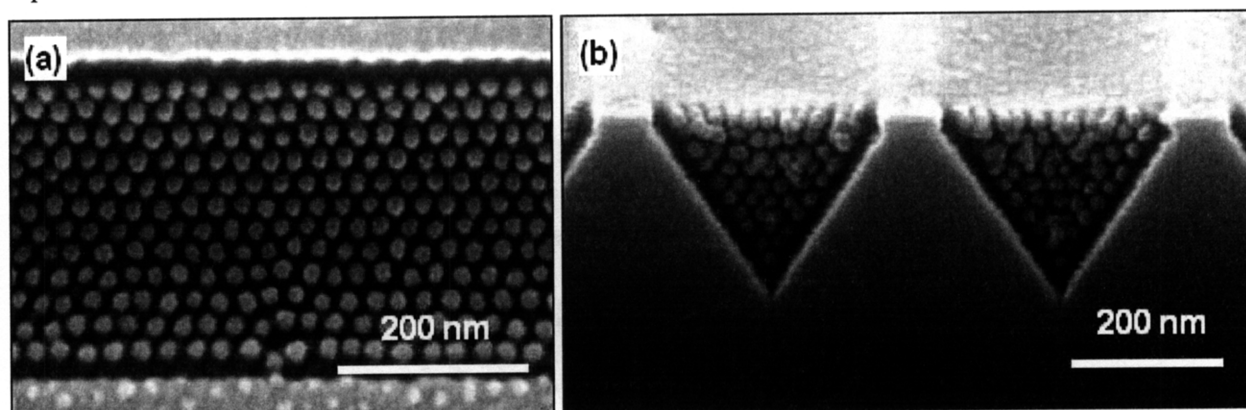

Figure 3-11 (a) SEM image of a sphere array showing a close-packed sphere arrangement on the top surface. (b) SEM image of a crosssection of the same sample showing the nonepitaxial top layer above the fcc arrangement of the lower layers.

To quantify the sphere arrangement, we show in Figure 3-12 a plot of the number of layers of spheres seen in the cross-sectional images versus the polymer film thickness. This thickness is divided by t_0 = 20.46 nm, which is the average spacing between layers in the cross-sectional projection measured from all samples (excluding the spacing between the top and second layers in those samples with a smaller sphere diameter in the top layer). Two sets of data points are plotted. Solid points represent samples in which the diameter of the top-layer spheres is similar to that of underlying layers. In these samples, the top layer was usually hexagonally arranged, and therefore nonepitaxial with the underlying fcc array (as in Figure 3-11a), although some samples showed a square symmetric, epitaxial top layer (as in Figure 3-10b or e). These data points form a "staircase" plot in which a given integer number of layers, N, can be found in films within a thickness range of approximately $(N + 0.5)t_0$ to $(N + 1.5)t_0$. The second set of data points, shown with open symbols, represents arrays where the top layer of spheres is significantly smaller than the underlying spheres. In this case, a fractional layer number was calculated as the ratio of the projected area of the top layer of spheres to that of the underlying spheres in the cross-sectional image. All of these samples show square-symmetric, epitaxial top layers. The data points are clustered in between the horizontal sections of the staircase plot.

A solid line, corresponding to a slope of 1.0, is fitted through the solid data points. This intersects the x axis at a thickness of $0.99t_o$. The nonzero intercept is due to the presence of the brush layer at the surfaces of the grooves. The PFS block preferentially wets the surfaces of the groove,[10] which are covered by a thin native oxide layer, leading to an offset of the first layer of spheres above the lowest part of the V groove, as indicated in the inset of Figure 3-12. Films thinner than $\sim t_0$ are expected to consist only of a brush layer and would not show a well-developed sphere morphology.

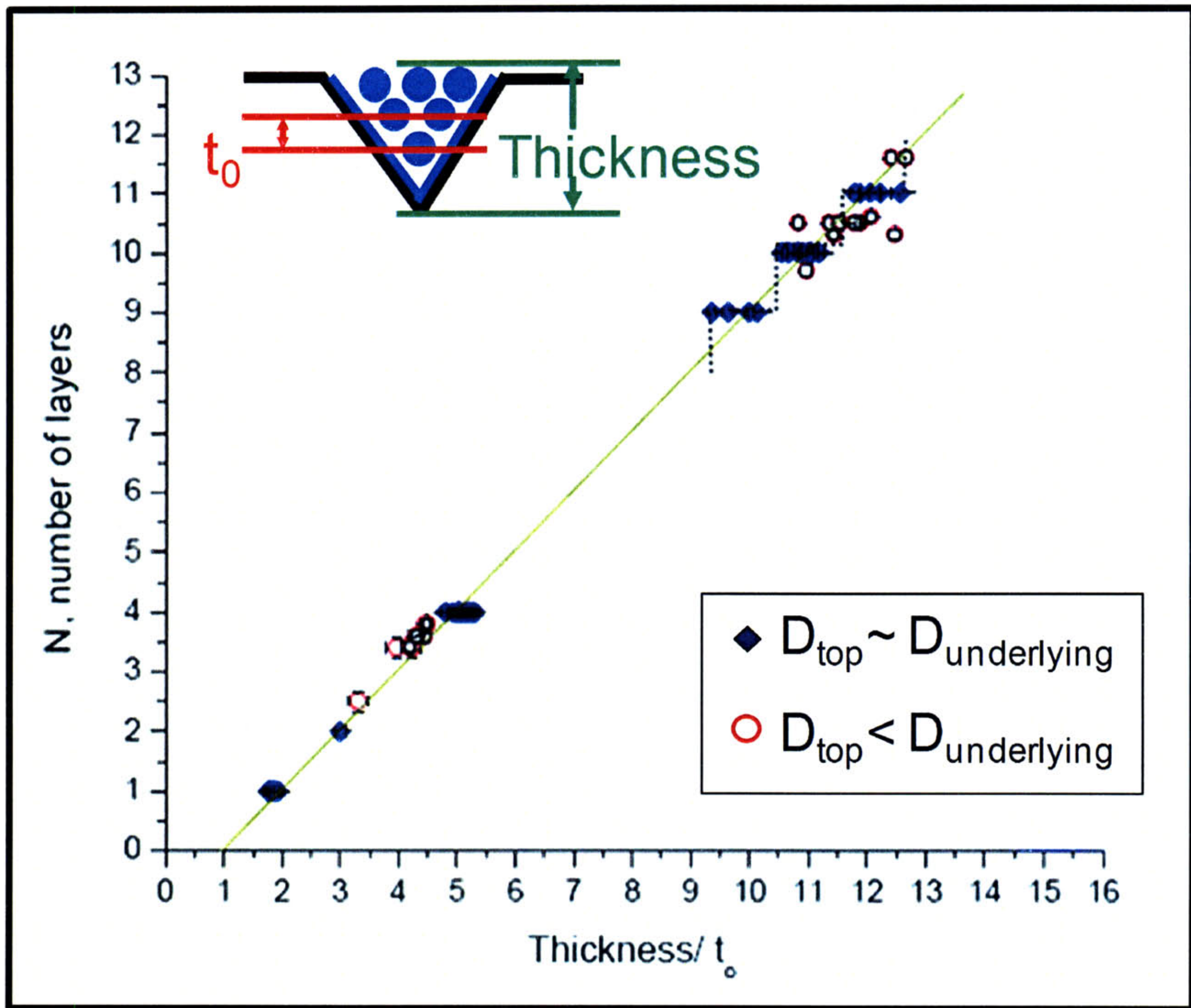

Figure 3-12 Number of layers of spheres in the cross-section images plotted against the polymer film thickness. The thickness is divided by the average layer spacing, t_0, of 20.5 nm. The solid points indicate the sample in which the diameter of the top-layer spheres(D_{top}) is similar to that of the underlying layers($D_{underlying}$). These form a staircase, indicated for $N = 9$-11 layers with a dotted line. The open circles represents arrays where the top layer of spheres is significantly smaller than the underlying spheres. The inset shows that PFS (in blue) wets the surface of the groove.

The BCP can fill the V-shaped confinement in different ways depending on the relationship between the polymer film thickness and the periodicity of the spherical domains. The geometry of the V groove promotes a fcc packing of the spheres, which conforms exactly to the angle of the groove. If the film thickness is close to an integer number of (100) fcc sphere

layers, then a well-ordered fcc structure is expected to form. However, deviations from exact commensurability can be accommodated in two ways: either by the formation of a top fcc layer with a different sphere diameter and thickness, or by a change in the packing of the top layer that maintains, approximately, the sphere diameter, but leads to defective packing such that the top layer is no longer epitaxial with the underlying fcc sphere array. For example, the sample in Figure 3-11 exhibits the latter case, where the loss of epitaxy in the top layer has allowed an additional row of spheres to be present in the top layer. The coexistence of these two types of morphology in this BCP system suggests that the energy differences between them are modest, though the formation of the smaller-diameter epitaxial spheres appears to dominate when the film thickness is furthest from commensurability. The formation of spheres that are significantly smaller than the equilibrium size, but with equilibrium in-plane periodicity, suggests a change in conformation of the polymer molecules, and has some resemblance to the arrangement on a substrate of block copolymer micelles with a compact core and an extended corona.

Finally, Figure 3-13 shows the coexistence of different top layer sphere arrangements within a groove. This sample shows a change from four rows of spheres to five, with the introduction of a defect in the top, nonepitaxial layer of spheres, as shown in the schematic cross-sectional view on the bottom.

3.4.3 The packing behavior in shallow trenches and in V grooves

The behavior of this spherical-morphology PS-PFS block copolymer shows interesting parallels with the packing of the same polymer in shallow, vertical-walled trenches[9, 10] and also with the packing of colloidal spheres in V grooves.[51-54] For the same PS-PFS BCP arranged in a shallow trench, a well-ordered close-packed monolayer of spheres is observed for all groove

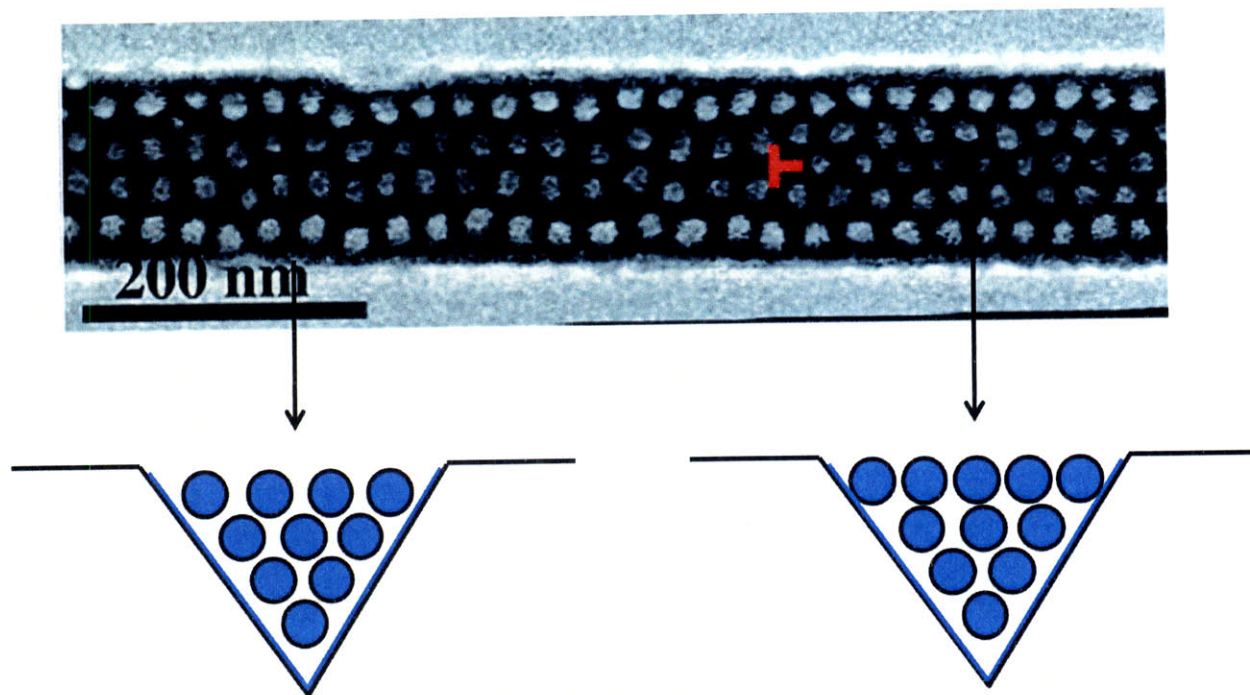

Figure 3-13 Top: SEM image showing a change in the number of rows in the top layer of a sphere array from 4 to 5, and the presence of an associated defect in the packing is marked in red. Bottom: the schematic showing corresponding crosssectional view. Blue dots represent PFS domains.

widths up to approximately $13d_o$ (~320 nm), beyond which long-range order breaks down. In the ordered monolayer, the row spacing adjusts such that an integer number of rows of polymer spheres forms within the groove, leading to a staircase-shaped plot of number of rows of spheres versus groove width, but for all groove widths the sphere array is close-packed with hexagonal (or slightly distorted hexagonal) packing. In contrast, the polymer confined within the V groove does not adjust its interlayer spacing t_o within the bulk of the groove, and incommensurabilities are instead accommodated by changes in packing, or changes in sphere diameter, which are restricted to the top layer of spheres. Thus, the top layer of spheres may show a hexagonal arrangement or a square arrangement. It is significant that the groove geometry promotes a fcc sphere array even for relatively thick films, despite the bulk morphology being bcc.

As a further comparison, colloidal spheres assembled in V grooves also show fcc packing with a square-symmetric top layer,[51-54] which is superficially similar to that of the BCP spheres, though on a much larger length scale. However, if the number of spheres available does not form an integer number of layers, then partial layers are created, containing vacancies. In the BCP case, the local density of the block copolymer remains constant and the system cannot form "vacancies", so the incommensurability must be accommodated by adjustment of the sphere size or the packing structure.

3.4.4 Pattern transfer of the surface pattern from 3-D structures

The square array formed by the fcc-packed BCP may have uses in block copolymer lithography or other device applications where a square array of nanostructures is required. Unlike the case of a monolayer of block copolymer domains, the pattern cannot simply be transferred into an underlying functional layer by etching.[9] Instead, an alternative pattern transfer method, such as nanoimprinting, may be used. For example, we made an imprint stamp from an etched PS-PFS block copolymer film by coating it with a conformally sputtered 7-nm-thick silica layer, and then stamped it into a polymethyl methacrylate (495 kg/mol) resist layer with a pressure of 150 MPa at 110 °C for 3.5 h. This leads to an imprinted pattern in the resist corresponding to the topography of the top layer of PFS domains.

In conclusion, a spherical diblock copolymer microphase-separated within a V-shaped groove forms an fcc structure because of the geometric constraints of the substrate, in which the close-packed (111) planes are parallel to the groove surfaces, and the top surface of the array is a (100) plane with square symmetry. The top layer of spheres adjusts its structure depending on the commensurability between the thickness of the polymer and the (100) plane spacing. Either the

sphere diameter adjusts within the top layer, while maintaining the fcc epitaxy, or the top layer of spheres may lose its epitaxial relation with the underlying fcc lattice and instead form a close-packed layer. This behavior differs from that of colloidal sphere packing,[51-54] which exhibits vacancies in the structure if the top layer of spheres is incomplete. The square symmetry of the top layer of the fcc block copolymer sphere array may provide a useful template for making square arrays of nanostructures. The ability to form ordered 3D arrangements for a range of film thicknesses makes BCPs attractive for the fault-tolerant templated self-assembly of nanoscale periodic arrays.

References

1. Bates, F. S.; Fredrickson, G. H. *Annu. Rev. Phys. Chem.* **1990,** 41, (1), 525-557.
2. Park, C.; Yoon, J.; Thomas, E. L. *Polymer* **2003,** 44, (22), 6725-6760.
3. Black, C. T. *Applied Physics Letters* **2005,** 87, (16), 163116-3.
4. Fasolka, M. J.; Mayes, A. M. *Annu. Rev. Mater. Res.* **2001,** 31, (1), 323-355.
5. Stoykovich, M. P.; Muller, M.; Kim, S. O.; Solak, H. H.; Edwards, E. W.; de Pablo, J. J.; Nealey, P. F. *Science* **2005,** 308, (5727), 1442-1446.
6. Shin, K.; Xiang, H.; Moon, S. I.; Kim, T.; McCarthy, T. J.; Russell, T. P. *Science* **2004,** 306, (5693), 76.
7. Wu, Y.; Livneh, T.; Zhang, Y. X.; Cheng, G.; Wang, J.; Tang, J.; Moskovits, M.; Stucky, G. D. *Nano letters* **2004,** 4, (12), 2337-2342.
8. Darling, S. B.; Yufa, N. A.; Cisse, A. L.; Bader, S. D.; Sibener, S. J. *Advanced Materials* **2005,** 17, (20), 2446-2450.
9. Cheng, J. Y.; Ross, C. A.; Thomas, E. L.; Smith, H. I.; Vancso, G. J. *Advanced Materials* **2003,** 15, (19), 1599-1602.
10. Cheng, J. Y.; Mayes, A. M.; Ross, C. A. *Nature Materials* **2004,** 3, (11), 823-828.
11. Li, H.-W.; Huck, W. T. S. *Nano letters* **2004,** 4, (9), 1633-1636.
12. Black, C. T.; Bezencenet, O. *IEEE Transactions Nanotechnology* **2004,** 3, (3), 412-415.
13. Fasolka, M. J.; Harris, D. J.; Mayes, A. M.; Yoon, M.; Mochrie, S. G. J. *Physical Review Letters* **1997,** 79, (16), 3018.
14. Naito, K. H., H.; Sakurai, M.; Kamata, Y.; Asakawa, K. *IEEE Transactions Magnetics* **2002,** 38, (5), 1949-1951.
15. Edwards, E. W.; Stoykovich, M. P.; Müller, M.; Solak, H. H.; Pablo, J. J. d.; Nealey, P. F. *J. Polym Sci. B Polym. Phys.* **2005,** 43, (23), 3444-3459.
16. Xiao, S.; Yang, X.; Edwards, E. W.; La, Y.-H.; Nealey, P. F. *Nanotechnology* **2005,** 16, (7), S324-S329.
17. La, Y.-H.; Edwards, E. W.; Park, S.-M.; Nealey, P. F. *Nano Letters* **2005,** 5, (7), 1379-1384.
18. Walsh, M. E. On the design of lithographic interferometers
and their application. Massachusetts Institute of Technology, Cambridge, 2004.
19. Walsh, M. E. On the design of lithographic interferometers and their application. Massachusetts Institute of Technology, Cambridge, MA, 2004.
20. Cheng, J. Y.; Ross, C. A.; Thomas, E. L.; Smith, H. I.; Vancso, G. J. *Applied Physics Letters* **2002,** 81, (19), 3657-3659.
21. Savas, T. A.; Farhoud, M.; Smith, H. I.; Hwang, M.; Ross, C. A. *Journal of Applied Physics* **1999,** 85, (8), 6160-6162.
22. Cheng, J. Y.; Zhang, F.; Chuang, V. P.; Mayes, A. M.; Ross, C. A. *Nano Letters* **2006,** 6, (9), 2099-2103.
23. Maier, S. A.; Kik, P. G.; Atwater, H. A.; Meltzer, S.; Harel, E.; Koel, B. E.; Requicha, A. A. G. *Nature Materials* **2003,** 2, (4), 229-232.
24. Cowburn, R. P.; Welland, M. E. *Science* **2000,** 287, (5457), 1466-1468.
25. Imre, A.; Csaba, G.; Ji, L.; Orlov, A.; Bernstein, G. H.; Porod, W. *Science* **2006,** 311, (5758), 205-208.
26. Chen, W.; Ahmed, H.; Nakazoto, K. *Applied Physics Letters* **1995,** 66, (24), 3383-3384.

27. Kelly, K. L.; Coronado, E.; Zhao, L. L.; Schatz, G. C. *J. Phys. Chem. B* **2003,** 107, (3), 668-677.
28. Kang, Y.; Erickson, K. J.; Taton, T. A. *J. Am. Chem. Soc.* **2005,** 127, (40), 13800-13801.
29. Deng, Z.; Tian, Y.; Lee, S.-H.; Ribbe, A. E.; Mao, C. *Angew. Chem., Int. Ed.* **2005,** 44, (23), 3582-3585.
30. Warner, M. G.; Hutchison, J. E. *Nat Mater* **2003,** 2, (4), 272-277.
31. Le, J. D.; Pinto, Y.; Seeman, N. C.; Musier-Forsyth, K.; Taton, T. A.; Kiehl, R. A. *Nano Letters* **2004,** 4, (12), 2343-2347.
32. Cheng, J. Y.; Ross, C. A.; Chan, V. Z. H.; Thomas, E. L.; Lammertink, R. G. H.; Vancso, G. J. *Advanced Materials* **2001,** 13, (15), 1174-1178.
33. Park, M.; Harrison, C.; Chaikin, P. M.; Register, R. A.; Adamson, D. H. *Science* **1997,** 276, (5317), 1401-1404.
34. Cheng, J. Y.; Jung, W.; Ross, C. A. *Physical Review B* **2004,** 70, (6), 064417.
35. Guarini, K. W.; Black, C. T.; Zhang, Y.; Kim, H.; Sikorski, E. M.; Babich, I. V. In *Process integration of self-assembled polymer templates into silicon nanofabrication*, Papers from the 46th International Conference on Electron, Ion, and Photon Beam Technology and Nanofabrication, Anaheim, California (USA), 2002; AVS: Anaheim, California (USA), 2002; pp 2788-2792.
36. Guarini, K. W.; Black, C. T.; Zhang, Y.; Babich, I. V.; Sikorski, E. M.; Gignac, L. M., Low voltage, scalable nanocrystal flash memory fabricated by templated self assembly. In *IEEE Int. Electron Devices Meet. (IEDM '03)* IEEE: Piscataway, NJ, 2003; p 541.
37. Segalman, R. A. *Mater. Sci. Eng., R* **2005,** 48, 191-226.
38. Walton, D. G.; Kellogg, G. J.; Mayes, A. M.; Lambooy, P.; Russell, T. P. *Macromolecules* **1994,** 27, (21), 6225-6228.
39. Yu, B.; Sun, P.; Chen, T.; Jin, Q.; Ding, D.; Li, B.; Shi, A.-C. *Physical Review Letters* **2006,** 96, (13), 138306-4.
40. Wu, Y.; Cheng, G.; Katsov, K.; Sides, S. W.; Wang, J.; Tang, J.; Fredrickson, G. H.; Moskovits, M.; Stucky, G. D. *Nat Mater* **2004,** 3, (11), 816-822.
41. Wang, Q.; Nealey, P. F.; de Pablo, J. J. *Macromolecules* **2001,** 34, (10), 3458-3470.
42. Fasolka, M. J.; Banerjee, P.; Mayes, A. M.; Pickett, G.; Balazs, A. C. *Macromolecules* **2000,** 33, (15), 5702-5712.
43. Pereira, G. G. *Macromolecules* **2004,** 37, (4), 1611-1620.
44. Chen, H.-Y.; Fredrickson, G. H. *The Journal of Chemical Physics* **2002,** 116, (3), 1137-1146.
45. Chuang, V. P.; Cheng, J. Y.; Savas, T. A.; Ross, C. A. *Nano Letters* **2006,** 6, (10), 2332-2337.
46. Matsen, M. W.; Bates, F. S. *Macromolecules* **1996,** 29, (4), 1091-1098.
47. Thomas, E. L.; Kinning, D. J.; Alward, D. B.; Henkee, C. S. *Macromolecules* **1987,** 20, (11), 2934-2939.
48. Henkee, C. S.; Thomas, E. L.; Fetters, L. J. *Journal of Materials Science* **1988,** 23, (5), 1685-1694.
49. Yokoyama, H.; Kramer, E. J.; Rafailovich, M. H.; Sokolov, J.; Schwarz, S. A. *Macromolecules* **1998,** 31, (25), 8826-8830.
50. Yokoyama, H.; Mates, T. E.; Kramer, E. J. *Macromolecules* **2000,** 33, (5), 1888-1898.
51. Ozin, G. A.; Yang, S. M. *Advanced Functional Materials* **2001,** 11, (2), 95-104.

52. Matsuo, S.; Fujine, T.; Fukuda, K.; Juodkazis, S.; Misawa, H. *Applied Physics Letters* **2003,** 82, (24), 4283-4285.
53. Yin, Y.; Lu, Y.; Gates, B.; Xia, Y. *J. Am. Chem. Soc.* **2001,** 123, (36), 8718-8729.
54. Yin, Y.; Xia, Y. *Advanced Materials* **2002,** 14, (8), 605-608.

Chapter 4 Novel structures from triblock terpolymers with all organic segments

4.1 Introduction

One of the main challenges in block copolymer lithography is to create a set of essential pattern geometries from which complex devices may be formed, such as sets of parallel lines, lines with angles (L-shapes), junctions (T-shapes) and *square* arrays of dots. Diblock copolymers (dBCPs), which microphase separate into spheres, cylinders, gyroids or lamellae in the bulk, have been used to form well-ordered arrays of nano-scaled lines and dots,[1-3] single rows of ellipses[4] or crossed lines[5] by self-assembly on substrates with chemical or topographical templates created using electron beam lithography. In addition to dot and line structures, a number of devices make use of ring-shaped features, for example memories,[6, 7] sensors,[8] and quantum devices,[9, 10] and structures for persistent current phenomena.[11] It is therefore of interest to create ring-shaped patterns by self-assembly of a block copolymer, as well as the lines and dots already achieved. Although ring structures do not occur in a bulk untemplated dBCP, concentric cylinders formed by lamellar dBCPs[12, 13] and helical structures formed by cylindrical dBCPs[14, 15] have been demonstrated by self-assembly of dBCPs within 3D templates such as narrow pores. However, pattern transfer from these 3D structures may be difficult. Ring and rod morphologies have been demonstrated in polystyrene-*b*-poly(4-vinyl pyridine) (PS-*b*-P4VP) in a mixture of water and toluene, but the rings are randomly distributed and mixed with rods.[16] In addition, randomly distributed rings have been observed in polyisoprene-*b*-poly(4-vinyl pyridine) (PI-*b*-P4VP) in a tetrahydrofuran (THF) /ethanol solvent mixture.[17] Rings have also been made by self-assembly of a cylindrical dBCP in circular pits,[18] and a wide range of patterns has been fabricated using directed assembly of a blended dBCP on chemically patterned substrates,[19, 20] but these methods require fabrication of appropriate templates.

In contrast, ring structures may be formed without templating by the self-assembly of more complex block copolymers such as the linear ABC triblock terpolymers. In such materials a diversity of new structures can be obtained by designing the combination of block sequence, the interaction parameter between the adjacent blocks, and the volume fraction and molecular weights of the three blocks.[21, 22] The experimental and theoretical work on ABC triblock terpolymers deals mainly with the bulk morphology,[23-31] but there has been some study of the complex structures generated by microphase separation of triblock terpolymer thin films.[32-42] For example, highly ordered perforated lamellae were formed in films of poly(styrene-*b*-2-vinyl pyridine-*b*-*tert*-butyl methacrylate) (PS-*b*-P2VP-*b*-PtBMA),[32, 33] and well ordered nanoporous thin films were made from poly(ethylene oxide-*b*-methyl methacrylate-*b*-styrene) (PEO-*b*-PMMA-*b*-PS).[38] Moreover, nanopores with controlled pore wall functionality were fabricated by removing the core domains in core-shell structured triblock terpolymers,[39] while structures containing highly ordered perpendicular lamellae were made by application of an electric field to a triblock terpolymer with a short middle block.[41] Finally, a ring array in a poly(isoprene-*b*-styrene-*b*-lactide) (PI-*b*-PS-*b*-PLA) thin film has been demonstrated, where the PI and PLA were removed to leave PS rings.[42]

Despite this progress in understanding triblock thin film morphologies, there has been relatively little work on the use of triblock terpolymers as lithographic templates for pattern transfer. Here we show that an array of rings can be formed in poly(butadiene-*b*-styrene-*b*-methyl methacrylate) (PB-*b*-PS-*b*-PMMA) thin films. The terpolymer was synthesized by sequential anionic polymerization, and spin-coated to form the geometry shown in Fig. 4-1. The PMMA and PB blocks were then removed to leave the ring-shaped PS domains, and this pattern was transferred into a silica film. Silica rings may then serve as a mask for further pattern

transfer into a functional material.

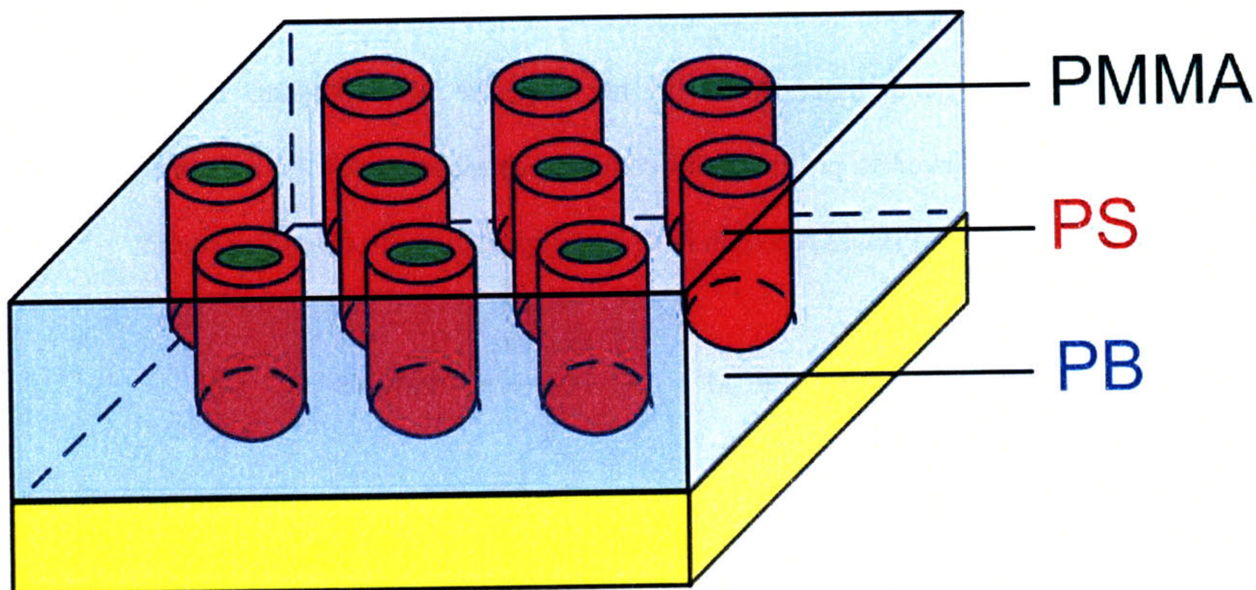

Figure 4-1 Schematic of a concentric cylinder morphology triblock terpolymer PB-*b*-PS-*b*-PMMA.

4.2 Experimental Methods

4.2.1 Synthesis and characterization of $PB_{1,4}$-*b*-PS-*b*-PMMA triblock terpolymers

The terpolymers were synthesized by Dr. Panayiotis Bilalis in Professor Nikos Hadjichristidis's group at University of Athens. The polymer synthesis and almost all the purification techniques were performed under vacuum, in all-glass reactors provided with break-seals and constrictions. The purification of the monomers, (1,3-butadiene, styrene, methyl methacrylate), 1,1-diphenylethylene (DPE), the solvents (THF and benzene), and the terminating agent MeOH was carried out according to literature methods.[43] The initiator *sec*-butyl lithium (*sec*-BuLi) was prepared under vacuum from *sec*-butyl chloride and lithium metal in hexane.[44] In a typical experiment shown in Scheme 4-1 (described here for $PB_{1,4}$-*b*-PS-*b*-PMMA with a

molecular weight of 141 kg/mol, or BSM[141]), 70 mL of benzene was distilled into the polymerization apparatus, then 3.8 g of 1,3-butadiene was poured into the reactor flask, followed by addition of 0.047 mmol *sec*-BuLi, by breaking the corresponding break-seal. The polymerization was allowed to proceed until complete consumption of the monomer (24h). A small sample of the living PB was then removed, by flame sealing, for characterization.

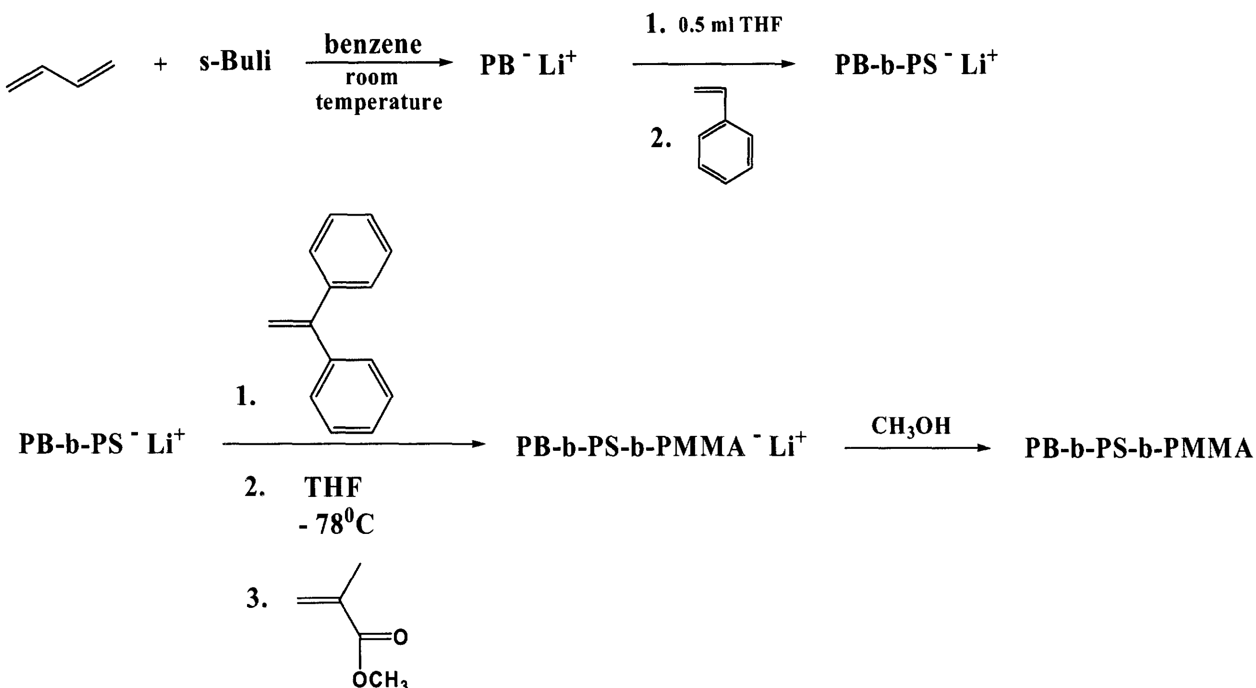

Scheme 4-1 Experimental pathway for the synthesis of $PB_{1,4}$-*b*-PS-*b*-PMMA triblock terpolymers.

A small amount of THF (0.5 ml) was added into the solution, followed by styrene (1.9 g), and the reaction was allowed to proceed for 24h. After the polymerization was completed, 0.18 mmol of DPE (3-fold excess over the concentration of the living anions) was added. The solution was collected into an ampoule equipped with a break-seal which was removed from the apparatus by flame sealing. A small amount of the living PB-*b*-PS was used for characterization. The ampoule was attached to another apparatus where 210 mL of THF (THF/benzene=3/1) was

distilled and then the apparatus was subsequently sealed off from the vacuum line. The flask was cooled to -78 °C in a dry ice—2-propanol bath. The break-seal of the ampoule containing the living PB-*b*-PS end-capped with DPE was broken and the polymerization of methyl methacrylate was initiated by breaking the methyl methacrylate ampoule (0.5 g) and distilling the monomer into the reactor. The polymerization was conducted for 1h under vigorous mixing using a glass stirrer. Finally the living polymer was deactivated by adding degassed methanol. The polymer was precipitated in excess methanol. The final product was dried in a vacuum oven until constant weight. Three PB-*b*-PS-*b*-PMMA terpolymers, BSM^{141}, BSM^{179}, and BSM^{185}, of molecular weights 141 kg/mol, 179 kg/mol, and 185 kg/mol respectively, were synthesized (Table 4-1).

Sample	ϕ_{PB} %v/v^{b}	ϕ_{PS} %v/v^{b}	ϕ_{PMMA} %v/v^{b}	PDI	$PB_{1,2}$ %w/w^{b}	$PB_{1,4}$ %w/w^{b}	PS %w/w^{b}	PMMA %w/w^{b}
$B_{85}S_{40}M_{16}^{141}$	62.7	27.4	9.9	1.05	14.7	45.7	28.0	11.6
$B_{111}S_{36}M_{32}^{179}$	64.7	19.6	15.7	1.04	7.9	54.3	20.3	17.5
$B_{101}S_{55}M_{29}^{185}$	57.1	29.0	13.8	1.05	6.2	48.4	29.7	15.7

Table 4-1 Volume percentages (v/v%), polydispersity (PDI) and weight percentages (w/w%) of the three triblock terpolymers, based on densities of PB: 0.9 g/cm^3, PS: 1.07 g/cm^3 and PMMA: 1.19 g/cm^3. In $B_xS_yM_z^w$, x,y and z denote the blocks' molecular weights and w denotes the total molecular weight. This data is provided by Dr. Panayiotis Bilalis.

To characterize the intermediate compounds, size-exclusion chromatography (SEC) experiments were conducted at 40 °C using a modular instrument consisting of a Waters model

510 pump, a Waters model U6K sample injector, a Waters model 401 differential refractometer, a Waters model 486 UV spectrometer, and a set of 4 μ-Styragel columns with a continuous porosity range from 10^6 to 10^3 Å. Tetrahydrofuran was the carrier solvent at a flow rate of 1 mL/min. Dual-detector SEC analysis [refractive index and two angle laser light scattering (SEC-TALLS) detectors], using a Waters 1525 high-pressure liquid-chromatography pump, Waters Ultrastyragel columns (HR-2, HR-4, HR-5E, and HR-6E), a Waters 2410 differential refractometer detector, and a Precision 2020 two-angle (15°, 90°) light-scattering detector, was also employed for the determination of the refractive index increments, dn/dc, and the weight-average molecular weights of the samples. The ^{1}H NMR spectra were recorded in chloroform-*d* at 25 °C with a Varian Unity Plus 300/54 NMR spectrometer.

4.2.2 Thin film deposition and characterization

The thin film samples were prepared by spin coating of 1wt% toluene solution of PB-*b*-PS-*b*-PMMA to form films with thickness of 33 nm to 59 nm, as determined by ellipsometry. Substrates consisted of SiO_2(19 nm)/Cu(2 nm)/Co(9 nm)/Si substrate, in which the layers were deposited by electron beam evaporation. After annealing the terpolymer film in acetone vapor for 5-6 hrs or toluene vapor for 17 hrs at room temperature, various etching steps were applied in order to remove the PB and PMMA domains completely before transferring the remaining PS pattern into the silica layer. Deep UV exposure in an OAI (Optical Associates Inc.) exposure system using a wavelength of 220 nm and power of 0.48μW for 320s or 500s, and oxygen reactive ion etching (RIE, in a Plasmatherm etcher) were primarily used to etch the PMMA. The PB was etched using UV/ozone, which attacks the double bonds of the 1,4 addition. The samples

were then immersed in deionized water at room temperature or at 50°C to wash away the degraded PB. The PS patterns were transferred into silica using a CHF_3 RIE.

4.3 Criteria for polymer design

The polymers used here were designed using two criteria. First, the interaction parameters and volume fractions of the blocks were chosen to generate a bulk morphology expected to consist of an array of core-shell cylinders. Core-shell cylinders will occur in an ABC triblock terpolymer if C is the majority block, which forms the matrix surrounding the cylinders, and if χ(A-C) > χ(B-C) > χ(A-B),[45] where χ is the segment-segment chemical interaction (Flory-Huggins) parameter, which is proportional to the difference between the solubility parameters of the components (blocks)) for nonpolar polymers.[46] In the PB-*b*-PS-*b*-PMMA system, the solubility parameters of PS, PB, PMMA are 18.5 $(MPa)^{1/2}$, 17 $(MPa)^{1/2}$, and 19 $(MPa)^{1/2}$, respectively.[47] Since PB-PMMA has the largest positive interaction paramete,[34] this polymer is expected to order into periodic core-shell cylinders if PB is the majority block. The core-shell structures would consist of a PMMA core and a PS shell in a PB matrix. The second criterion is that the inner most and outer most blocks should be removable with high selectivity, so that the blocks can be removed without degrading the cylindrical shell morphology. In this work we use a high percentage of 1, 4-addition PB which can be etched using ozone to react with the double bond in the polymer backbone. These design considerations may be extendable to the formation of other triblock terpolymer thin film morphologies for lithographic applications.

4.4 $PB_{1,4}$-*b*-PS-*b*-PMMA triblock terpolymer characteristics

For these experiments, three different $PB_{1,4}$-*b*-PS-*b*-PMMA triblock terpolymers were synthesized with molecular weights 141 kg/mol, 179 kg/mol and 185 kg/mol (Table 4-1), labeled

BSM[141], BSM[179], and BSM[185]. This is the first report of the synthesis of this particular triblock terpolymer. Although the synthesis of $PB_{1,4}$-*b*-PS-*b*-PMMA is much more difficult than that of $PB_{1,2}$-*b*-PS-*b*-PMMA, it was necessary for lithographic processing because $PB_{1,4}$ can be removed more easily with ozonolysis compared to $PB_{1,2}$.[48]

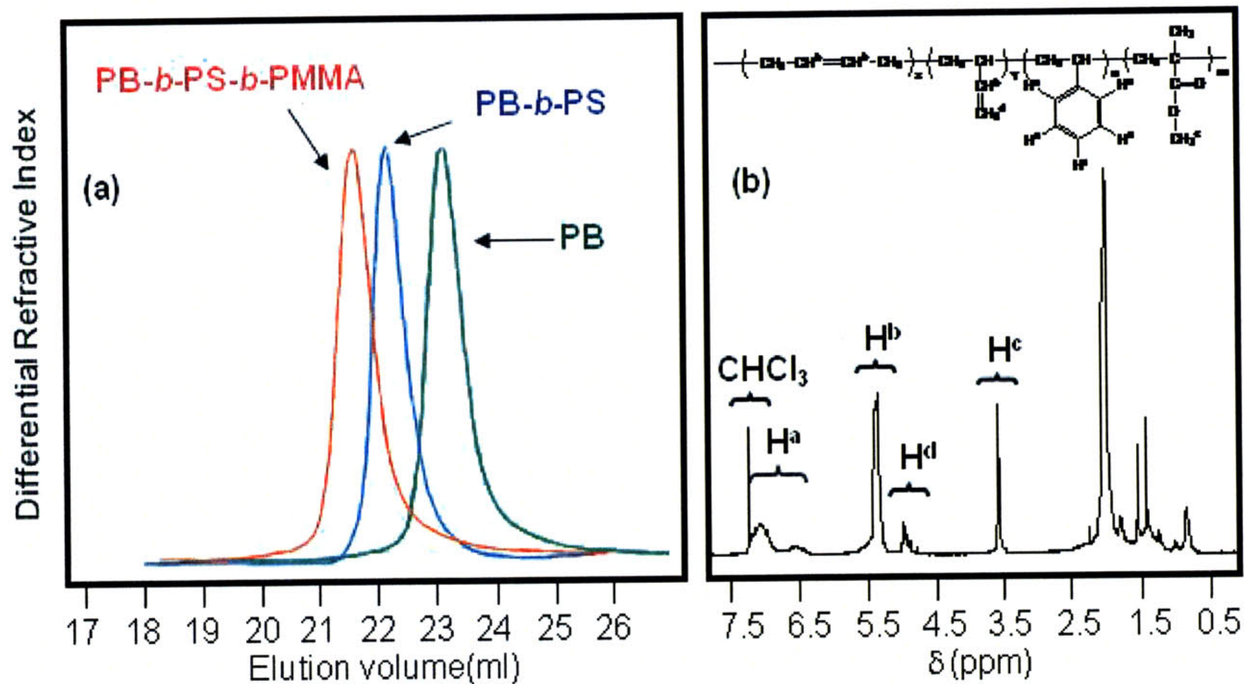

Figure 4-2 (a) SEC chromatogram of the intermediate compounds and final PB-*b*-PS-*b*-PMMA triblock terpolymer BSM[141], (b) ^1H NMR of the $PB_{1,4}$-*b*-PS-*b*-PMMA triblock terpolymer BSM[141]. The blocks in the chemical structure labeled x and y indicate 1,2 and 1,4 PB respectively. This data is provided by Dr. Panayiotis Bilalis.

Figure 4-2(a) shows a representative example (BSM[141]) of size-exclusion chromatography (SEC) monitoring during the synthesis of the BSM triblock terpolymers. The polydispersity index (M_w/M_n) of the intermediate and final products is extremely low (PDI=1.05) and no extra peaks, indicating deactivation of living chains, are apparent. The molecular weights

of the intermediate and final products were determined by low-angle light scattering and are listed in Table 4-1. A representative ^{1}H NMR spectrum for BSM[141] is shown in Figure 4-2(b). The PS aromatic protons appear between 6.3 and 7.5 ppm, the methyl protons of PMMA are displayed at 3.6 ppm, whereas the characteristic PB protons resonate at 5 ppm (2 protons for $PB_{1,2}$) and 5.4 ppm (2 protons for $PB_{1,4}$ and 1 proton for $PB_{1,2}$).

4.5 Thin film orientation and morphology

4.5.1 Effect of solvent annealing

From the volume fractions and χ-parameters of the blocks, the bulk morphology of the terpolymers is expected to consist of PMMA cylinders with a PS shell in a PB matrix. Although the bulk morphology was not analyzed directly, images of the thin films, described below, show that this morphology was formed under the processing conditions used in this work. In order to use these terpolymers as lithographic masks for making ring arrays, the cylinders must be oriented perpendicular to the film plane. This orientation can be accomplished by a combination of film thickness control and solvent annealing of the film after spin-casting. During solvent annealing, the polymer film absorbs the solvent and swells. Upon removal from the solvent atmosphere, the concentration of the solvent in the film next to the free surface decreases, creating a concentration gradient normal to the surface, and this becomes the ordering front as the solvent evaporates from the film.[49] Furthermore, the process can be controlled by choice of solvent. For example, the vapor pressure for acetone at room temperature (181 Torr) is much higher than that of toluene (22 Torr), and as a result, the degree of swelling is higher for acetone than that for toluene[50] and the rapid evaporation of acetone promotes perpendicular cylinder formation due to kinetic constraints.[51] Compared to toluene, acetone has a strong preferential affinity for the PMMA block[52] while PB (32mJ/m^2) and PS (40.7mJ/m^2) have lower surface

energy than PMMA (41.1mJ/m^2).[53] The balance between selectivity of the solvent and surface energy of the swollen blocks can also promote the formation of perpendicular cylinders.[54] Thus, solvent annealing was used both to provide chain mobility to promote ordering in the polymer films and to induce orientation of the cylinders perpendicular to the film plane.

4.5.2 Effect of film thickness

Figure 4-3 shows the effect of film thickness on the morphology of BSM[179] films, which were annealed in toluene vapor then etched using deep UV exposure and oxygen reactive ion etching to remove the PMMA, then with UV plus ozone and water to remove the PB. At 33.1 nm thickness, the cylinders are oriented perpendicular to the film, but as the thickness increases to 51 nm, a mixed orientation is formed, and at 62.3 nm, short in-plane cylinders are observed. The formation of in-plane cylinders is expected in films thicker than about half the domain periodicity.[49] Our terpolymers have periods of ~65 – 90 nm, which was measured from the SEM images of etched terpolymer films, so the observations are consistent with this expectation. The high molecular weights lead to poor ordering kinetics, and the cylinders form poorly ordered arrays.

The center-to center distance (period) of the cylinder arrays was measured from SEM images of etched films such as those shown in Fig. 4-3. The period represents the average center-to-center spacing of perpendicular cylinders, or the spacing measured normal to the cylinders for cylinders oriented in-plane. Each data point represents the average of approximately 20 measurements, and the standard deviation was of the order of ~7% of the period. The period was

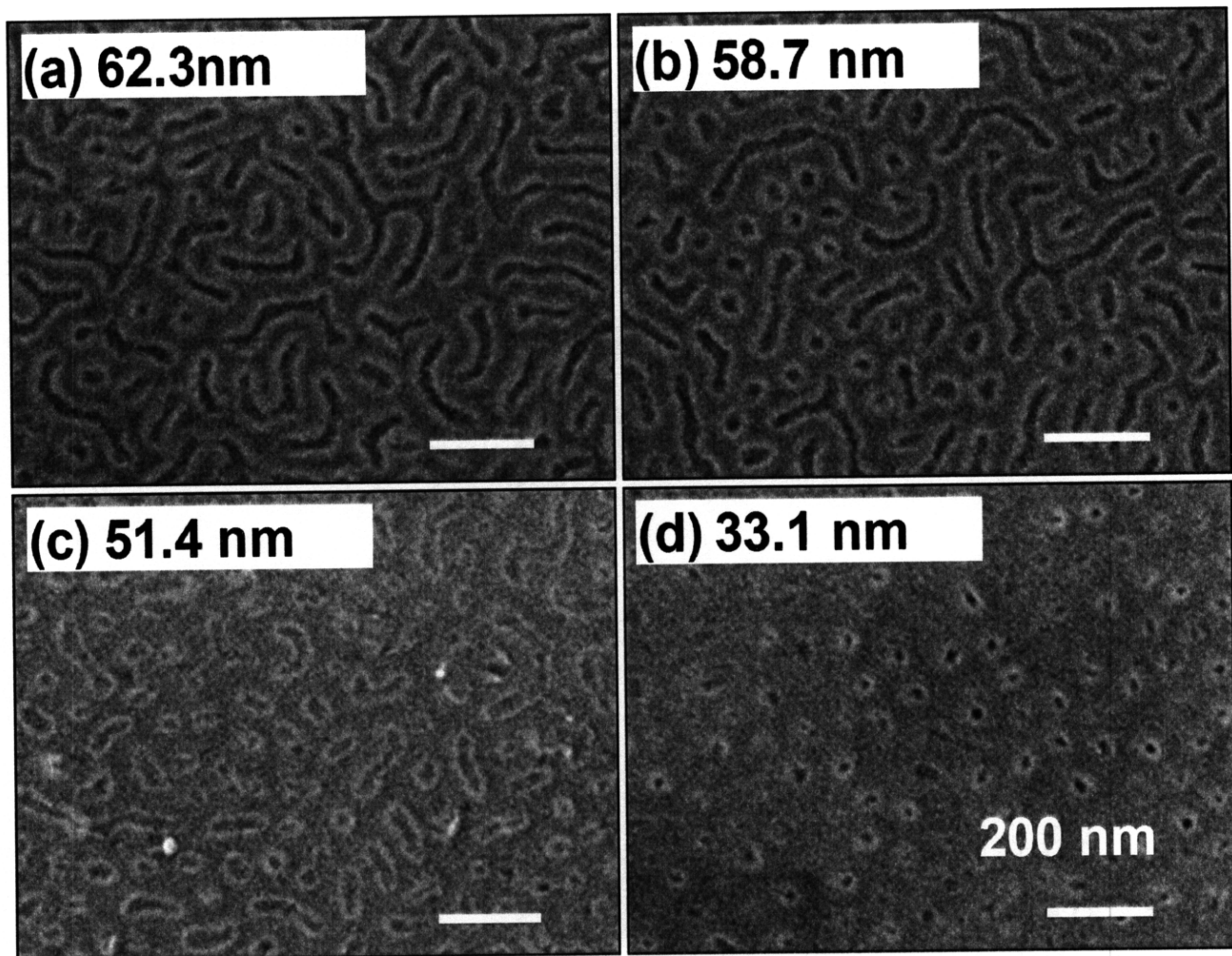

Figure 4-3 SEM images of thin films of BSM[179] with different thicknesses (labeled) after annealing in toluene vapor for 17.5 hrs at room temperature, followed by exposure with deep UV and etching with oxygen RIE to remove the PMMA, then etching with UV/O_3 and water to remove PB. The as-spun film thicknesses were (a) 62.3 nm (b) 58.7 nm(c) 51.4 nm and (d) 33.1 nm.

found to be sensitive to film thickness, but insensitive to the solvent annealing conditions. For example, Fig. 4-4 shows the period of BSM[179] as a function of film thickness. The period is approximately 78 nm for films with thickness of 50 – 65 nm, a thickness range within which in-plane cylinders form, but increases for film thicknesses below 43 nm when perpendicular cylinders form. Similarly, the period of BSM[185] decreases from 80 nm to 68 nm as the thickness

increases from 38.8 nm to 42.4 nm. However, the period is independent (within ~2nm) of the choice of toluene, tetrahydrofuran, or acetone solvent vapor for a given thickness. Thickness-dependent cylinder spacing has been observed in other systems, for example by Knoll et al.[55] for multilayered(one to five layers) in-plane cylindrical PS-*b*-PB diblock copolymers in which a unit cell stretches perpendicular to the plane of the film leading to an decreasing in period as the film thickness increases from n to n+1 layers of cylinders.

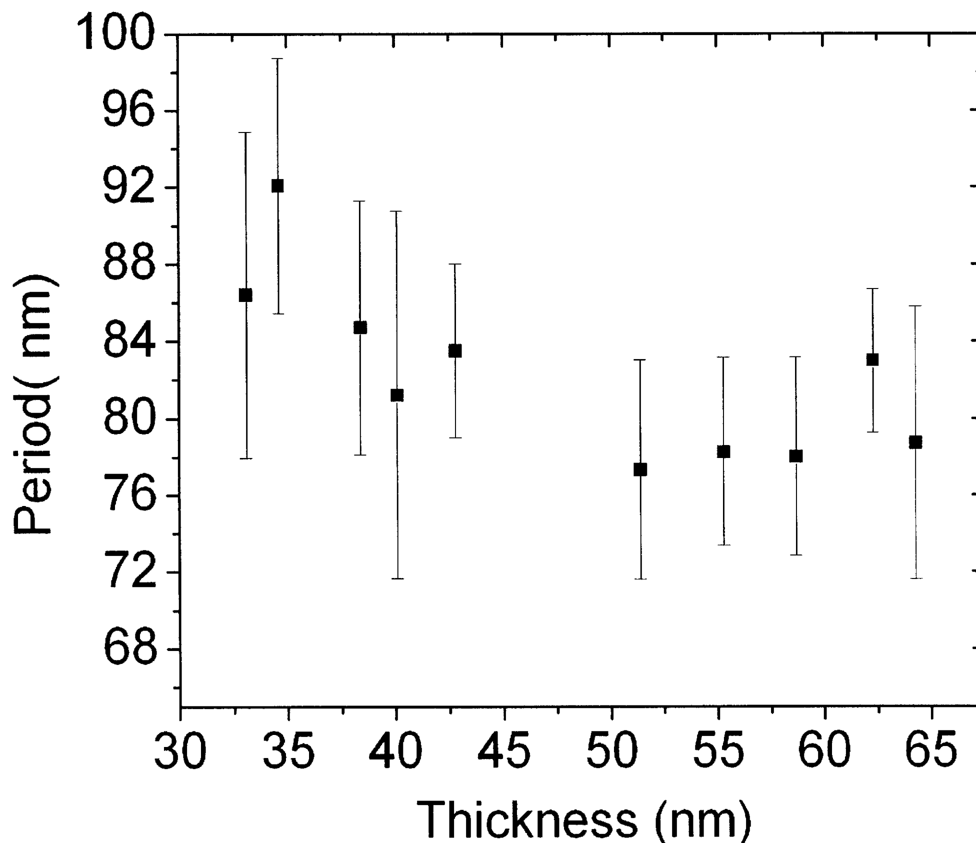

Figure 4-4 The period of the cylindrical domains in BSM[179] as a function of thickness. The error bars show one standard deviation.

Fig. 4-5 shows images of etched BSM films. The thickness of each film was within the range where perpendicular cylinders form, and corresponds to 42.4 nm, 42.8 nm and 43.0 nm for BSM^{141}, BSM^{179}, and BSM^{185}, respectively, which means the films have approximately the same thickness. Table 4-2 shows period and microdomain inner(core cylinder) and outer(core plus shell cylinder) diameters of the three triblock terpolymers. The period of BSM^{185} is comparable to that of BSM^{179} because of the similarity in their molecular weights. The accuracy of the measurement is limited by the poorly ordered microdomains and SEM edge contract effect.

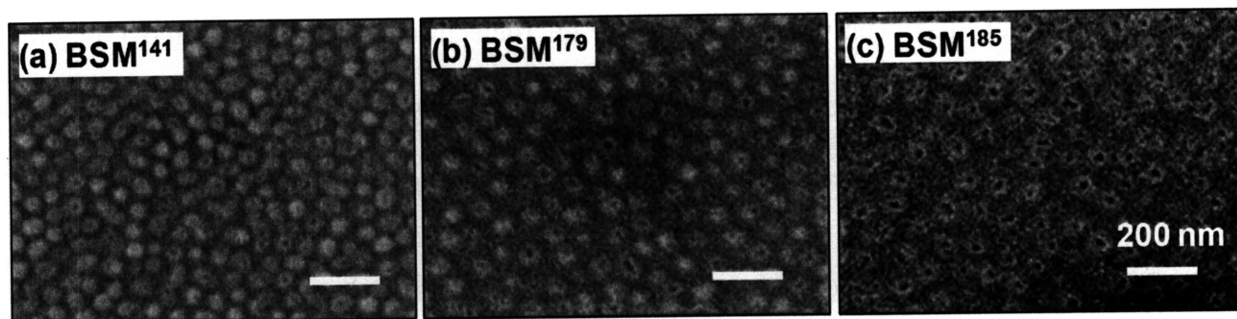

Figure 4-5 SEM images of thin films of PB-*b*-PS-*b*-PMMA (a) MW: 141 kg/mol (b) MW: 179 kg/mol (c) MW: 185kg/mol after annealing in toluene vapor, then UV exposure and etching with oxygen plasma.

	BSM^{141}	BSM^{179}	BSM^{185}
Film thickness (nm)	42.4	42.8	43.0
Period (nm)	66±5	82±8	86±7
Inner ring diameter (nm)	11±2	12±2	15±2
Outer ring diameter (nm)	44±4	56±7	55±5

Table 4-2 Period and dimensions of PS ring patterns in films of the three triblock terpolymers after annealing in toluene vapor followed by deep UV exposure and oxygen etching. The data is based on the average of approximately 20 measurements from several SEM images including those of Fig. 4-5.

4.5.3 Selective etching of the PS, PB and PMMA blocks

The etch selectivity among the three blocks is one of the essential considerations for lithographic applications. As illustrated in Fig. 4-3, in the PB-*b*-PS-*b*-PMMA triblock terpolymer, deep UV exposure degrades the PMMA domains and subsequent oxygen RIE removes the degraded PMMA to reveal the spatial arrangement of hollow PS cylinders in the PB matrix. In addition, a UV/ozone treatment degrades the 1,4 addition in the PB matrix by breaking the carbon-carbon double bonds in the polymer backbone. The combination of UV irradiation and ozone (O_3), or UVO_3, has been widely used in the microelectronics industry to remove organic contamination.[56, 57] The degraded PB can be simply washed away by immersing in water.[48] Thus in the end one is left with PS rings, which can be used as a lithographic mask.

To quantify the etch selectivity, we begin by analyzing the etch rate of homopolymer PB, PS and PMMA (hPB, hPS and hPMMA) thin films under several etching conditions. Thin films of hPB (10.7 kg/mol molecular weight) with 19%1,2-addition, hPS (17.5 kg/mol), and hPMMA (10.5 kg/mol) were spin-coated on silicon substrates with initial thicknesses of 55.1-58.3 nm, 52.5-56.9 nm, and 42.5-44.5 nm respectively. After different etch protocols, the change in film thickness was measured. The thickness of each homopolymer film that was removed is given in Table 4-3 for a range of etch conditions. hPMMA has the highest etch rate for each etching condition, suggesting that PMMA can be removed with good selectivity compared to PS and PB. The maximum etch selectivity between hPMMA and hPS was obtained by including a UVO_3/water process step at 50°C.

However, the 50°C water process leads to the production of stable intermediate compounds in hPB,[58] and the UV process can cause cross-linking of the 19% 1,2-PB present in

Etch method	Etched thickness of hPMMA (nm)	Etched thickness of hPS (nm)	Etched thickness of hPB (nm)
A. i) DUV exposure+O_2 RIE 11s	16.2	5.5	7.8
ii) followed by UV/O_3 90s +water@50°C	26.3	3	2.2
B. i) DUV exposure followed by UV/O_3 90s +water@50°C	42.5	0	3.7
C. i) UV/O_3 90s +water@50°C	30.6	4.7	9.4
ii) followed by O_2 RIE 12s	--	9.3	11.2
D. i) O_2 RIE 11s	16.9	6.2	7.7
ii) followed by UV/O_3 90s +water@50°C	10.6	1.4	1.6
iii) followed by 3 repeats of UV/O_3 90s +water@50°C	--	9.4	6.8
iv) followed by UV/O_3 90s + CHF_3 RIE 180s	--	10.2	12.2

Table 4-3 Etching of homopolymer PS (hPS), hPB and hPMMA under different etching conditions. The thickness of each film removed by each etch step is given in nm and determined by ellipsometry averaging over 1 cm^2. The initial thicknesses of the films were in the range 44 – 58 nm. The dashes indicate where the etch thickness could not be measured because the film was mostly or completely etched by previous steps.

hPB, making hPB more etch resistant. There was considerably less etch selectivity between hPB and hPS, with the hPS often etching at a similar rate to the hPB. The best process to remove

hPMMA and hPB while leaving the hPS unaffected was protocol B in Table 4-3, which involved the use of deep UV exposure followed by a UVO_3/water process step at 50°C.

4.5.4 Pattern transfer into silica

The results in the previous section demonstrate conditions under which hPMMA and hPB etch faster than hPS, as required for the formation of PS rings from the triblock terpolymer. However, when applying these etch methods to our triblock terpolymers, we found that the PMMA block could not be removed as easily as the results on the homopolymer suggest. For example, UVO_3/water was found to be ineffective by itself in removing the PMMA cores of the cylinders, and composite disks of PS/PMMA instead of rings of PS were obtained after an UVO_3/water treatment.

Several methods based on the results in Table 4-3 were explored to etch the terpolymer and to subsequently transfer the pattern from the polymer to the underlying silica film, three of which will be described here for BSM[179]. In the first method, PMMA was removed by deep UV exposure and oxygen RIE, then the PB was etched using UVO_3/water treatment, then the remaining PS pattern was etched into the silica layer using CHF_3 RIE. However, the PB was only partly removed by the UVO_3/water treatment leading to incomplete transfer of the ring pattern (Fig. 4-6(a)). There are three possible reasons for this: first, the 1,2 addition in the PB matrix may have been cross-linked under the deep UV exposure.[59] Second, after multiple or long term UVO_3/water treatment, extended ozonation may have led to nonselective etching causing the loss of the original cylindrical features.[60] Third, the PS features may not extend completely through the film due to the strong affinity of PMMA silicon with native oxide[61] and a wetting layer of PB at the silicon-polymer interface has also been observed in PS-*b*-PB diblock copolymer.[62]

The second pattern transfer method is to omit the deep UV exposure and oxygen RIE and instead use only the UVO_3/water treatment followed by CHF_3 RIE. The problem of cross-linking in the PB matrix is not an issue in this case. However, discrete dots instead of rings were formed in the silica layer, since the PS and PMMA are both etched only slowly by the UVO_3/water treatment. Ozone attacks the in-chain double bond of PB, but PS has no double bonds in the polymer chain, and it is degraded about six times more slowly than PB in ozone.[63] Besides, it was shown that the thickness of a PMMA homopolymer film did not change even after 60 min exposure to ozone while a PS homopolymer film, on the other hand, showed an exponential decrease in thickness as exposed to ozone.[64] As a result, PMMA is even more stable than polystyrene under ozone treatment.

The third method is to use only deep UV exposure followed by UVO_3/water, then a combined CHF_3 RIE and UVO_3/water treatment. The cross-sectional SEM image in Fig. 4-6(b) shows a PS ring-capped silica array. The pattern can also be transferred by applying a short oxygen RIE before the CHF_3 RIE (Fig. 4-6(c) and (d)). Fig. 4-6(c) shows a plan view of PS ring-capped silica and Fig. 4-6(d) shows a mixture of silica rings and dots after removing the PS rings by oxygen RIE. In this process, the UV exposure time also plays an important role. Underexposure leads to interconnected dots and rings, while overexposure gives isolated but partly missing rings.

In Fig. 4-6(b-d), we see that the 20 nm thick PS ring array was transferred into a 19 nm thick SiO_2 layer. However, compared to the etched BSM[179] film (Fig. 4-5(a)), the quality and uniformity of the silica pattern is degraded. For example, in Fig. 4-6(d), only about 80% of the

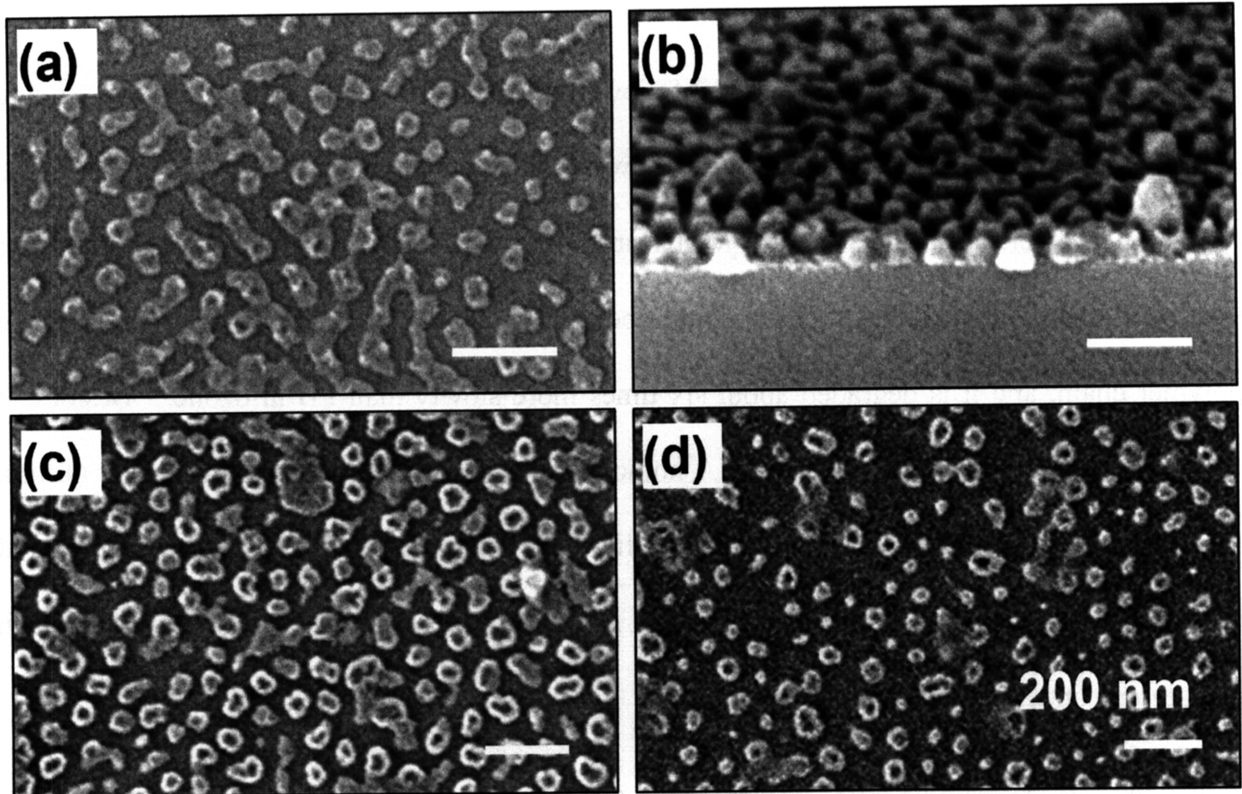

Figure 4-6 Pattern transfer into silica rings from a BSM[179] film annealed in acetone vapor for 6 hrs. (a) The PMMA was removed with deep UV exposure and O_2 RIE, the PB with UV/ozone and water treatment, then the PS pattern was etched into the silica using CHF_3 RIE. The PB was only partially removed leading to interconnected features, and overetching with CHF_3 causes missing rings. (b) Side view of PS-topped silica rings after a sequence of deep UV exposure, UVO_3/water (2x), CHF_3 RIE for 2.75 min, and an additional UVO_3/water treatment to remove the PMMA and PB, then a CHF_3 RIE for 1.85 min to transfer the pattern into silica. (c) Plan view of PS-topped silica rings after a sequence of deep UV exposure, UVO_3/water (3x), a short oxygen RIE, and a CHF_3 RIE for 2.75 min; (d) Plan view of silica rings after the sequence in (c) with an additional CHF_3 RIE for 0.85 min and oxygen RIE to remove the PS, leaving only the pattern in the silica.

PS rings transferred into silica features, and of these, only about 25% are rings instead of dots. In the etched BSM[179] film the average period, outer ring diameter, and inner ring diameter of the PS block after PB and PMMA removal were 83±7 nm, 41±5 nm and 15±2 nm respectively. For the

silica ring pattern, measurements of just the ring-shaped features gave average values of 85±8 nm, 48±12 nm, and 18±4 nm, respectively. The poor uniformity of the silica rings is attributed partly to poor uniformity of the PS domains in the etched film, and partly to degradation of the PS features during pattern transfer. The quality of the etched pattern may be improved by using a more etch-resistant block chemistry in place of the PS, for example an organometallic or Si-containing block such as poly(ferrocenyldimethylsilane) or poly(dimethylsiloxane), both of which have high etch resistance under an oxygen plasma and can serve as a good etch mask for transferring the pattern into silica.[3, 65]

4.6 Conclusion

Cylindrical core-shell morphology thin films were obtained from $PB_{1,4}$-*b*-PS-*b*-PMMA triblock terpolymers with total molecular weights of 141 kg/mol, 179 kg/mol and 185 kg/mol synthesized by anionic polymerization. Thin films of the polymers were formed by spin-coating and annealed to form self-assembled arrays of core-shell cylinders oriented perpendicular to the surface. The PMMA core and PB matrix blocks were removed using sequential etching, and the remaining PS ring pattern was transferred into an underlying silica film to form ring features. Pattern transfer from a 179 kg/mol molecular weight polymer led to pattern of silica rings with height 19 nm, although the quality of the silica ring pattern was degraded compared to that of the triblock terpolymer.

References

1. Cheng, J. Y.; Mayes, A. M.; Ross, C. A. *Nature Materials* **2004,** 3, (11), 823-828.
2. Zschech, D.; Kim, D. H.; Milenin, A. P.; Scholz, R.; Hillebrand, R.; Hawker, C. J.; Russell, T. P.; Steinhart, M.; Gosele, U. *Nano Letters* **2007,** 7, (6), 1516-1520.
3. Jung, Y. S.; Ross, C. A. *Nano Letters* **2007,** 7, (7), 2046-2050.
4. Cheng, J. Y.; Zhang, F.; Chuang, V. P.; Mayes, A. M.; Ross, C. A. *Nano Letters* **2006,** 6, (9), 2099-2103.
5. Kim, H.-C.; Cheng, J.; Rettner, C.; Park, O.-H.; Miller, R.; Hart, M.; Sundstrom, L.; Zhang, Y. *Proc. SPIE* **2007,** 6519, 65191H-8.
6. Castaño, F. J.; Morecroft, D.; Jung, W.; Ross, C. A. *Physical Review Letters* **2005,** 95, (13), 137201-4.
7. Podbielski, J.; Giesen, F.; Grundler, D. *Physical Review Letters* **2006,** 96, (16), 167207-4.
8. Miller, M. M.; Prinz, G. A.; Cheng, S. F.; Bounnak, S. *Applied Physics Letters* **2002,** 81, (12), 2211-2213.
9. Aharonov, Y.; Bohm, D. *Physical Review* **1959,** 115, (3), 485-491.
10. Yu, L. W.; Chen, K. J.; Song, J.; Xu, J.; Li, W.; Li, X. F.; Wang, J. M.; Huang, X. F. *Physical Review Letters* **2007,** 98, (16), 166102-4.
11. Lévy, L. P.; Dolan, G.; Dunsmuir, J.; Bouchiat, H. *Physical Review Letters* **1990,** 64, (17), 2074-2077.
12. Sevink, G. J. A.; Zvelindovsky, A. V.; Fraaije, J. G. E. M.; Huinink, H. P. *Journal of Chemical Physics* **2001,** 115, (17), 8226-8230.
13. Xiang, H.; Shin, K.; Kim, T.; Moon, S. I.; McCarthy, T. J.; Russell, T. P. *Macromolecules* **2004,** 37, (15), 5660-5664.
14. Yu, B.; Sun, P.; Chen, T.; Jin, Q.; Ding, D.; Li, B.; Shi, A.-C. *Physical Review Letters* **2006,** 96, (13), 138306-4.
15. Xiang, H.; Shin, K.; Kim, T.; Moon, S. I.; McCarthy, T. J.; Russell, T. P. *Macromolecules* **2005,** 38, (4), 1055-1056.
16. Pietsch, T.; Gindy, N.; Fahmi, A. *Polymer* **2008,** 49, (4), 914-921.
17. Haiying, H.; Bonghoon, C.; Jueun, J.; Hae-Woong, P.; Taihyun, C. *Angewandte Chemie International Edition* **2009,** 48, (25), 4594-4597.
18. Jung, Y. S.; Jung, W.; Ross, C. A. *Nano letters* **2008,** 8, (9), 2975-2981.
19. Stoykovich, M. P.; Kang, H.; Daoulas, K. C.; Liu, G.; Liu, C.-C.; de Pablo, J. J.; Müller, M.; Nealey, P. F. *ACS Nano* **2007,** 1, (3), 168-175.
20. Daoulas, K. C.; Muller, M.; Stoykovich, M. P.; Park, S.-M.; Papakonstantopoulos, Y. J.; de Pablo, J. J.; Nealey, P. F.; Solak, H. H. *Physical Review Letters* **2006,** 96, (3), 036104-4.
21. Bates, F. S.; Fredrickson, G. H. *Physics Today* **1999,** 52, (2), 32-38.
22. Abetz, V.; Simon, P. *Advances in Polymer Science* **2005,** 189, 125-212.
23. Hadjichristidis, N.; Iatrou, H.; Pitsikalis, M.; Pispas, S.; Avgeropoulos, A. *Progress in Polymer Science* **2005,** 30, (7), 725-782.
24. Takahashi, K.; Hasegawa, H.; Hashimoto, T.; Bellas, V.; Iatrou, H.; Hadjichristidis, N. *Macromolecules* **2002,** 35, (13), 4859-4861.
25. Brinkmann, S.; Stadler, R.; Thomas, E. L. *Macromolecules* **1998,** 31, (19), 6566-6572.
26. Ludwigs, S.; Böker, A.; Abetz, V.; Müller, A. H. E.; Krausch, G. *Polymer* **2003,** 44, (22), 6815-6823.

27. Gido, S. P.; Schwark, D. W.; Thomas, E. L.; do Carmo Goncalves, M. *Macromolecules* **1993,** 26, (10), 2636-2640.
28. Krappe, U.; Stadler, R.; Voigt-Martin, I. *Macromolecules* **1995,** 28, (13), 4558-4561.
29. Breiner, U.; Krappe, U.; Abetz, V.; Stadler, R. *Macromolecular Chemistry and Physics* **1997,** 198, (4), 1051-1083.
30. Jung, K.; Abetz, V.; Stadler, R. *Macromolecules* **1996,** 29, (3), 1076-1078.
31. Breiner, U.; Krappe, U.; Jakob, T.; Abetz, V.; Stadler, R. *Polymer Bulletin* **1998,** 40, (2), 219-226.
32. Ludwigs, S.; Boker, A.; Voronov, A.; Rehse, N.; Magerle, R.; Krausch, G. *Nature Materials* **2003,** 2, (11), 744-747.
33. Sperschneider, A.; Schacher, F.; Gawenda, M.; Tsarkova, L.; Müller, A. H. E.; Ulbricht, M.; Krausch, G.; Köhler, J. *Small* **2007,** 3, (6), 1056-1063.
34. Stocker, W.; Beckmann, J.; Stadler, R.; Rabe, J. P. *Macromolecules* **1996,** 29, (23), 7502-7507.
35. Elbs, H.; Drummer, C.; Abetz, V.; Krausch, G. *Macromolecules* **2002,** 35, (14), 5570-5577.
36. Böker, A.; Müller, A. H. E.; Krausch, G. *Macromolecules* **2001,** 34, (21), 7477-7488.
37. Elbs, H.; Abetz, V.; Hadziioannou, G.; Drummer, C.; Krausch, G. *Macromolecules* **2001,** 34, (23), 7917-7919.
38. Bang, J.; Kim, S. H.; Drockenmuller, E.; Misner, M. J.; Russell, T. P.; Hawker, C. J. **2006,** 128, (23), 7622-7629.
39. Rzayev, J.; Hillmyer, M. A. *Macromolecules* **2005,** 38, (1), 3-5.
40. Aizawa, M.; Buriak, J. M. *J. Am. Chem. Soc.* **2006,** 128, (17), 5877-5886.
41. Olszowka, V.; Hund, M.; Kuntermann, V.; Scherdel, S.; Tsarkova, L.; Böker, A.; Krausch, G. *Soft Matter* **2006,** 2, 1089-1094.
42. Guo, S.; Rzayev, J.; Bailey, T. S.; Zalusky, A. S.; Olayo-Valles, R.; Hillmyer, M. A. *Chemistry of Materials* **2006,** 18, (7), 1719-1721.
43. Hadjichristidis, N.; Iatrou, H.; Pispas, S.; Pitsikalis, M. *Journal of Polymer Science Part A: Polymer Chemistry* **2000,** 38, (18), 3211-3234.
44. Uhrig, D.; Mays, J. W. *Journal of Polymer Science Part A: Polymer Chemistry* **2005,** 43, (24), 6179-6222.
45. Sugiyama, M.; Shefelbine, T. A.; Vigild, M. E.; Bates, F. S. *Journal of Physical Chemistry B* **2001,** 105, (50), 12448-12460.
46. Nagarajan, R.; Barry, M.; Ruckenstein, E. *Langmuir* **1986,** 2, (2), 210-215.
47. Barton, A. F. M., *CRC Handbook of Polymer–Liquid Interaction Parameters and Solubility Parameters*. CRC Press: Boca Raton, FL, 1990; p 297.
48. Park, M.; Harrison, C.; Chaikin, P. M.; Register, R. A.; Adamson, D. H. *Science* **1997,** 276, (5317), 1401-1404.
49. Kim, S. H.; Misner, M. J.; Xu, T.; Kimura, M.; Russell, T. P. *Advanced Materials* **2004,** 16, (3), 226-231.
50. Elbs, H.; Krausch, G. *Polymer* **2004,** 45, (23), 7935-7942.
51. Kim, G.; Libera, M. *Macromolecules* **1998,** 31, (8), 2569-2577.
52. Xuan, Y.; Peng, J.; Cui, L.; Wang, H.; Li, B.; Han, Y. *Macromolecules* **2004,** 37, (19), 7301-7307.

53. Mark, J. E., *Physical Properties of Polymer Handbook*. AIP Press: New York, NY, 1996; p 405-406.
54. Cavicchi, K. A.; Berthiaume, K. J.; Russell, T. P. *Polymer* **2005,** 46, (25), 11635-11639.
55. Knoll, A.; Tsarkova, L.; Krausch, G., Nanoscaling of Microdomain Spacings in Thin Films of Cylinder-Forming Block Copolymers. In 2007; Vol. 7, pp 843-846.
56. Wood, P. C.; Wydeven, T.; Tsuji, O. *Mater. Res. Soc. Symp. Proc.* **1993,** 315, 237-242.
57. Kim, H.-C.; Kreller, C. R.; Tran, K. A.; Sisodiya, V.; Angelos, S.; Wallraff, G.; Swanson, S.; Miller, R. D. *Chemistry of Materials* **2004,** 16, (22), 4267-4272.
58. Zoller, D. L.; Johnston, M. V. *Macromolecules* **2000,** 33, (5), 1664-1670.
59. Raven, A. V.; Heusinger, H. *Journal of Polymer Science: Polymer Chemistry Edition* **1974,** 12, (10), 2255-2271.
60. Collins, S.; Hamley, I. W.; Mykhaylyk, T. *Polymer* **2003,** 44, (8), 2403-2410.
61. Mayes, A. M.; Russell, T. P.; Bassereau, P.; Baker, S. M.; Smith, G. S. *Macromolecules* **1994,** 27, (3), 749-755.
62. Harrison, C.; Park, M.; Chaikin, P. M.; Register, R. A.; Adamson, D. H.; Yao, N. *Polymer* **1998,** 39, (13), 2733-2744.
63. Rimmer, S.; Ebdon, J. R. *Journal of Polymer Science Part A: Polymer Chemistry* **1996,** 34, (17), 3573-3583.
64. Jeong, U.; Ryu, D. Y.; Kim, J. K.; Kim, D. H.; Russell, T. P.; Hawker, C. J. *Advanced Materials* **2003,** 15, (15), 1247-1250.
65. Cheng, J. Y.; Ross, C. A.; Chan, V. Z. H.; Thomas, E. L.; Lammertink, R. G. H.; Vancso, G. J. *Advanced Materials* **2001,** 13, (15), 1174-1178.

Chapter 5. Nanoscale ring arrays from polyferrocenylsilane containing triblock terpolymer

5.1 Introduction

Block copolymers can microphase-separate into periodic nanoscale structures with well defined geometries and length scales, making them attractive materials for self-assembled nanolithography.[1-4] Ordered arrays of block copolymer spheres, cylinders, or lamellae have been used to pattern features in functional materials with sizes of ~10-50 nm. The fabrication of a range of devices, such as silicon capacitors and transistors, discrete magnetic storage media, and photonic crystals,[5-8] have been demonstrated using block copolymer lithography.

Previous work has mainly focused on diblock copolymers, with the study of triblock or multiblock copolymers being less actively pursued, largely due to the increased level of synthetic difficulty. However, these materials offer a wider range of geometries than the line and dot patterns available from diblock copolymers, making them potentially valuable for nanolithography applications. In particular, triblock terpolymers can form ring shaped features, which are useful in the fabrication of memories or sensors,[9-11] and quantum devices.[12-14] Ring-shaped structures have been formed previously from thin films of core-shell structured linear ABC triblock terpolymers,[15-17] in which the cylinders are oriented perpendicular to the film plane during the anneal process. However, this work, as well as work on thin film triblock terpolymers of other morphologies,[18] has focused on materials in which all three blocks consist of organic segments. This can limit the utility of these materials in nanoscale lithography because the etch selectivity between the blocks, and their etch resistance for subsequent pattern transfer steps, is typically low. It is therefore interesting to examine thin film triblock terpolymers in which one of the blocks contains inorganic components which impart high etch selectivity and etch resistance.

Triblock copolymers containing inorganic blocks such as polyphosphazenes,[19, 20] polysilanes[21, 22] and polysulfides[23] have been prepared previously. However, these are symmetrical ABA type triblock copolymers, which phase separate on the nanoscale into morphologies comparable to diblock copolymers. There have been several studies on bulk ABC triblock terpolymers with an inorganic polydimethylsiloxane (PDMS) block,[24-26] such as polyisoprene-*b*-polystyrene-*b*-poly(dimethyl siloxane),[24, 25] and poly(ethyleneoxide)-*b*-poly(dimethyl siloxane)-*b*-poly(methyl oxazoline).[26]

Polyferrocenylsilane (PFS) is a metal-containing polymer with iron and silicon in the polymer backbone.[27] Synthesis of PFS with controlled molecular weights and narrow polydispersities is achieved by a living anionic mechanism.[28, 29] PFS has also been incorporated into multiblock copolymers with a variety of organic and inorganic coblocks.[28-34] These block copolymers microphase-separate to give ordered arrays of iron and silicon containing nanostructures, which have already been used in lithographic applications.[35-37] PFS possesses interesting properties including resistance to oxygen reactive ion etching,[35-38] which makes PFS containing block copolymers useful in nanolithographic applications. Despite much work being reported on the synthesis and self-assembly of PFS diblock copolymers, to date little work has been reported on PFS-containing triblock terpolymers, including polystyrene-*b*-polyferrocenylsilane-*b*-polymethylmethacrylate[39] and polyferrocenylphosphine-*b*-polyferrocenylsilane-*b*-polysiloxane.[40]

In this article, we describe the synthesis and thin film self-assembly of a new PFS-containing triblock terpolymer, polystyrene-*b*-polyferrocenylsilane-*b*-poly(2-vinylpyridine) (PS-*b*-PFS-*b*-P2VP) with a core-shell cylinder morphology consisting of a PS core with PFS shell in

a P2VP matrix. In thin PS-*b*-PFS-*b*-P2VP films, the PS and P2VP are selectively removed to leave PFS hollow cylinders, and these ring patterns are transferred into another polymeric layer by imprinting, illustrating its utility in nanolithography.

5.2 Experimental methods

5.2.1 Equipment and materials for synthesis of PS-b-PFS-b-P2VP triblock terpolymers

The synthesis and bulk morphology part of the experiment were done by Jessica Gwyther in Professor Ian Manner's group at University of Bristol. Ms. Gwyther supplied the decriptions and data in sections 5.2.1 and 5.2.2. All reactions were carried out on a glass vacuum line under purified nitrogen or in a Mbraun glove box in an inert purified argon atmosphere. Ferrocene pellets purchased from Octel Germany were crushed to a fine powder before use. N,N,N',N'-tetramethylethylenediamine (tmeda) from Fisher was dried over CaH_2 and purified by distillation under reduced pressure. ^{n}Butyllithium (^{n}BuLi) purchased from Acros (1.6 M in hexanes) was used as received. Dichloroethylmethylsilane from Aldrich was distilled prior to use. THF was distilled under reduced pressure from ^{n}BuLi and Na/benzophenone. Methanol was deoxygenated by freeze, pump and thaw method. Cyclohexane was dried over CaH_2 for 24 h before distillation. Styrene monomer was dried over CaH_2 for 24 h and subsequently distilled twice under reduced pressure prior to polymerization. ^{sec}Butyllithium (^{sec}BuLi) purchased from Aldrich (1.4 M in hexanes) was used as received. 2-Vinylpyridine monomer (97%) from Aldrich was dried over CaH_2 and purified by distillation under reduced vacuum. On the day of polymerization, 2-Vinylpyridine was distilled for a second time over trioctylaluminum purchased from Aldrich. 1-Diphenylethylene (DPE) (97%) from Aldrich was titrated with ^{n}BuLi and then distilled under reduced pressure. 1,1-Dimethylsilacyclobutane (DMSB) purchased from Aldrich was distilled

over CaH_2 twice. Lithium chloride (99.99%) purchased from Aldrich was vacuum dried at 120°C overnight.

^1H and ^{13}C spectra were obtained using JEOL Lambda 300 and ECP (Eclipse) spectrometers. Conventional Gel Permeation Chromatography (GPC) was carried out on a Viscotek GPCmax chromatograph equipped with a refractometer. A flow rate of 1.0 $mlmin^{-1}$ was used with nBu_4NBr / THF as the eluent. Alternatively, a Viscotek GPCmax chromatograph equipped with a triple detector array was used. A flow rate of 1.0 $mlmin^{-1}$ was used with THF as the eluent.

5.2.2 Synthesis and characterization of PS-b-PFS-b-P2VP triblock terpolymers

Synthesis of ethylmethylsilaferrocenophane monomer was carried out as described by Rider et al .[29] Styrene (0.57 g, 5.4 mmol) was dissolved in cyclohexane (2.5 ml) and initiated with $^{sec}BuLi$ (36 μl, 0.05 mmol) in an inert atmosphere glove box. After 1 h an aliquot of the living polystyrene solution was removed, quenched with degassed methanol and molecular weight determined by PS calibrated GPC. To the remaining living polystyrene solution, ethylmethylsilaferrocenophane (0.5 g, 2.0 mmol) in THF (3 ml) was added. After 1 h an aliquot of the living diblock copolymer solution was removed and quenched with degassed methanol. PS:PFS block ratios were determined by ^1H NMR. ^1H NMR of PS-*b*-PFS diblock copolymer (CD_2Cl_2), δ = 0.43 (s, 3H, Si-CH_3), 0.92 (q, br, 2H, Si-CH_2CH_3), 1.02 (t, br, 3H Si-CH_2CH_3), 1.53 (br, 2H, CH_2CH(Ph)), 1.78 (br, 1H, CH_2CH(Ph)), 4.00 (m, 4H, Cp), 4.21 (m, 4H, Cp), 6.57-7.05 (br, 5H, CH_2CH(*Ph*)). To the remaining living diblock copolymer solution, DPE (8.5 μl) was added, followed by DMSB (3.1 μl). The reaction was placed in a well in the glove box which had been cooled to -78 °C with dry ice and acetone. In a second vial a solution of dried

LiCl (5.1 mg, 0.12 mmol) and 2-vinylpyridine (0.26 ml, 2.4 mmol) in THF (1.5 ml) was also cooled to -78 °C before being combined with the living diblock system. The reaction was allowed to further proceed for 40 min at -78 °C before it was quenched by the addition of a few drops of degassed methanol.

The solution was precipitated into rapidly stirring hexanes followed by purification by dissolution into THF, dropwise addition of hexanes until a precipitate could be observed followed by centrifuge at 5000 rpm for 15 min. Drying overnight at 40°C under vacuum yielded the SFP_{94} triblock terpolymer as a yellow powder (0.341 g, 53%).

The synthetic procedure for the preparation of SFP_{94} triblock terpolymer is outlined in Scheme 5-1. The Manners group recently reported a new class of PFS diblock copolymer, PFS-*b*-P2VP, via a 1,1- dimethylsilacyclobutane (DMSB) mediated sequential polymerization,[41, 42] and synthesis of the SFP_{94} made use of this method.

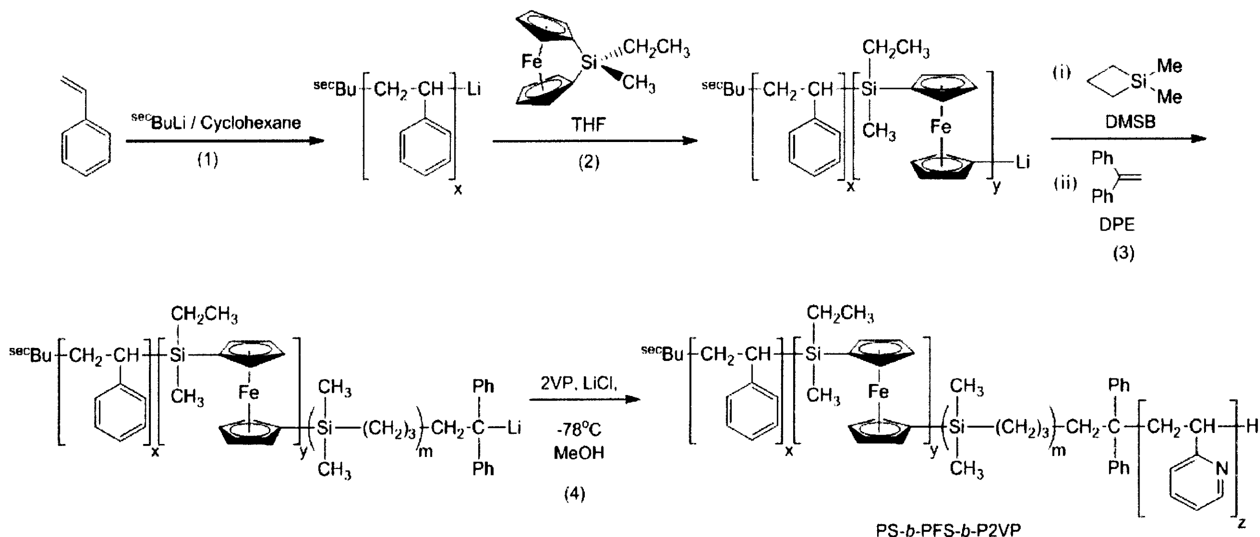

Scheme 5-1 Synthesis of PS-*b*-PFS-*b*-P2VP triblock terpolymer.

All polymers were characterized by ^1H NMR and GPC. The total molecular weight of the polymer was found to be M_n = 94,200 Da with a PDI = 1.09 and yield = 53%. A representative GPC trace of the triblock terpolymer and its precursor blocks is given in Figure 5-1.

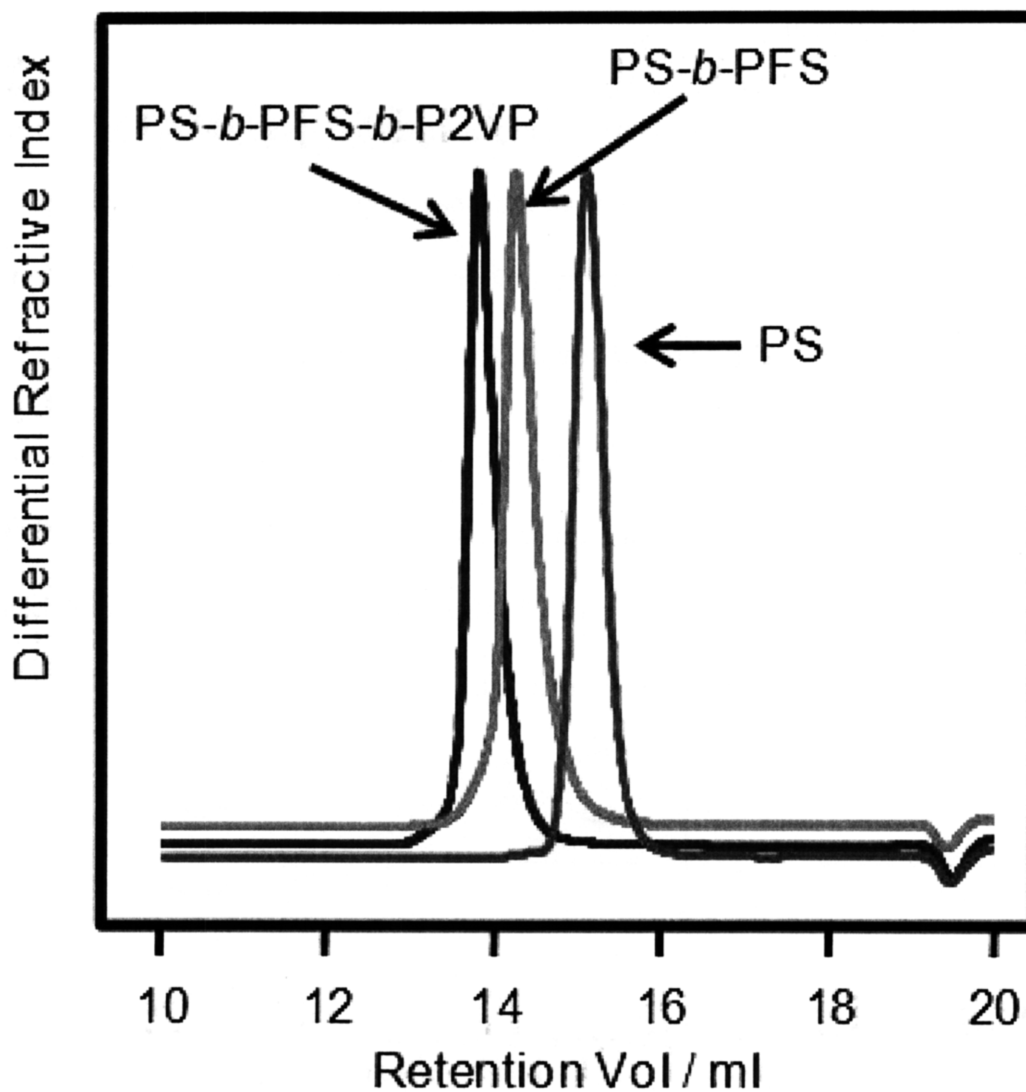

Figure 5-1 GPC trace (RI) of triblock terpolymer PS-*b*-PFS-*b*-P2VP and precursor blocks. GPC analysis: M_n = 94,200 Da, PDI = 1.09. This data is provided by Jessica Gwyther.

The ^1H NMR spectrum of the SFP_{94} triblock terpolymer, as shown in Figure 5-2, was used to determine the number of repeat units of the constituent blocks by integration.

5.2.3 Bulk morphology determination

A concentrated solution of the triblock terpolymer (~30 mgml^{-1}) was prepared in toluene. The solution was drop cast on to a glass slide over several days resulting in a bulk sample ~1 mm in thickness. Films were solvent annealed in a toluene chamber overnight before thermal annealing at 150°C under vacuum for 4 days. Rapid quenching with liquid nitrogen gave brittle orange films. Ultra thin sections (~50 nm) of the bulk films were microtomed and imaged by bright field TEM using a JEOL JEM 1200 EX microscope.

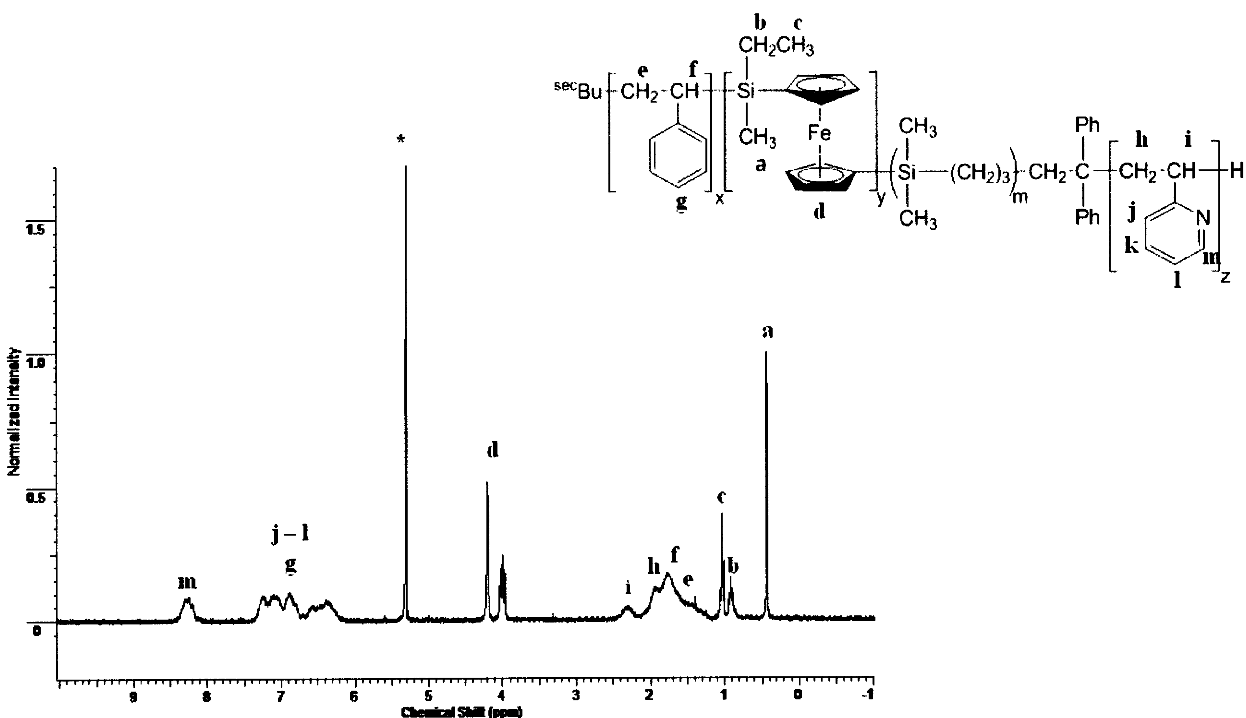

Figure 5-2 ^{1}H NMR spectrum of PS-*b*-PFS-*b*-P2VP in CD_2Cl_2, * denotes solvent peak. ^{1}H NMR (CD_2Cl_2), $\delta = 0.43$ (s, 3H, Si-C*H₃*), 0.92 (q, 2H, br, Si-CH_2CH_3), 1.03 (t, br, 3H Si-CH_2CH_3), 1.53 – 1.77 (br, 3H, CH_2CH(Ph)), 1.92 – 2.31 (br, 3H, CH_2CH(Py)) 3.99 (m, 4H Cp) 4.20 (m, 4H, Cp), 6.35 – 7.24 (br, 8H, CH_2CH(*Ph*) and CH_2CH(*Py*) (H in 4,5 and 6 position)), 8.30 (br, 1H, CH_2CH(*Py*) (H in 3 position). This data is provided by Jessica Gwyther.

5.2.4 Thin film deposition and characterization

The thin film samples were prepared by spin coating of 1.5 wt% toluene solution of PS-*b*-PFS-*b*-P2VP on the substrates to form films with thickness of 36 nm to 68 nm, as determined by ellipsometry. The chemically modified substrates were prepared from spin-coating of 1wt% of hydroxyl-terminated homopolymers (PS-OH (5k), PFS-OH (5k), P2VP-OH (5k)) solutions in toluene onto Si which was previously coated with 50 nm SiO_2 by electron beam evaporation. PS-OH and P2VP-OH are purchased from Polymer Source. PFS-OH was prepared by reduction of an aldehyde-terminated precursor.[43] The homopolymers were covalently bonded to the substrate after heating and unbonded polymers were then rinsed away with toluene.

After annealing the polymer film in chloroform vapor for 1-5 h or a mixture of chloroform and acetone vapor for 1-5 h at room temperature, oxygen reactive ion etching was used to partially remove the PS and P2VP domains to reveal the arrangement of PFS microdomains, which were imaged by SEM. The bottom view samples were prepared by dipping the annealed film into buffered HF solution for 30 s followed by 25% KOH solution at room temperature for 5 days. The PFS ring patterns were transferred into a PS layer using a cold isostatic press with a pressure of 20,000-30,000 psi for 3 min.

5.3 Polymer design

To obtain a core-shell structure in an ABC triblock terpolymer, it is necessary for the Flory-Huggins interaction parameters χ to satisfy the relation $\chi_{AC} > \chi_{BC} > \chi_{AB}$.[44] This condition is met by the PS-*b*-PFS-*b*-P2VP system, considering that the solubility parameters of PS, PFS, and P2VP are 18.5 $(MPa)^{1/2}$, 18.7 $(MPa)^{1/2}$, and 20.4 $(MPa)^{1/2}$, respectively.[45, 46] Asymmetric values between χ_{AB} and χ_{BC} stabilizes the core-shell structure.[44] A composition of $PS_{14.2k}$-*b*-

$PFS_{30.3k}$-*b*-$P2VP_{49.7k}$, where subscripts represent the block molecular weights in g/mol, was used, with a total molecular weight of 94.2 kg/mol (This 94.2 kg/mol PS-b-PFS-b-P2VP triblock terpolymer will be denoted SFP_{94}). The block volume fractions are 16%, 28%, 56%, respectively. In order to achieve the successful synthesis of triblock terpolymers via sequential living anionic polymerization, monomer should be added in order of reducing end group reactivity, limiting the possible sequencing of the blocks.[47] In this case, the relative order of reactivity of the living homopolymer chains is PS > PFS > P2VP.

The physical properties of PFS can be tuned by changing the substituents at the silicon; PFS is semicrystalline when symmetrically substituted by short n-alkyl groups, but amorphous when asymmetrically substituted. The PFS block reported here was chosen to be amorphous, with ethyl and methyl substituents on the silicon, to prevent complications during self-assembly due to crystallization.[48]

In the case of the core-shell structured triblock terpolymer with all organic segments, as discussed in Chapter 4, the remaining shell or ring was also degraded after removing core and matrix. By selecting the core-shell structured triblock terpolymer with organometallic middle block, the etch selectivity between the blocks and etch resistance for pattern transfer is improved. In addition, only oxygen plasma is needed to generate the ring pattern in the polymer layer, which simplified the etching process.

5.4 Self assembly of PS-*b*-PFS-*b*-P2VP triblock terpolymers in the bulk state

The bulk morphology of SFP_{94} was studied by slow casting a film (~1 mm in thickness) over several days, solvent annealing in a toluene chamber overnight and thermal annealing at 150°C under vacuum for 4 days. Rapid quenching with liquid nitrogen gave brittle orange films. Microtomed sections of the bulk film (~50 nm) were imaged by bright field TEM.

The bulk morphology adopted appears to show PS cylinders within PFS cylinders parallel to the surface of the film, within a P2VP matrix, as shown in Fig. 5-3(a). The centre-to-centre distance between polystyrene cylinders is 50 nm.

5.5 Thin film orientation and morphology

The bulk morphology of SFP_{94} is in agreement with the core-shell morphology expected from the volume fractions and χ-parameters of the blocks. However, in order to use such terpolymers as lithography masks for making ring arrays, the terpolymer must be produced as a thin film with the cylinders oriented perpendicular to the film plane. This orientation can be promoted by solvent annealing of the film after spin-casting.[49]

Additionally, the arrangement of cylinders at the substrate-film interface is controlled by the chemistry of the substrate, and therefore understanding the effects of the film thickness, the substrate chemistry, the surface energy of the blocks and the annealing conditions is necessary to control the morphology and orientation of the microdomains.

5.5.1 Effect of solvent annealing

Figure 5-3(b)-(e) show film morphologies for 64.6-68.8 nm thick SFP_{94} films after annealing in different solvent vapors: toluene, chloroform, acetone and an acetone-chloroform mixture. The PFS arrangement was revealed by etching the PS and P2VP in an oxygen plasma. The results can be understood by considering the solubility parameters for toluene, chloroform and acetone, which are 18.2 $(MPa)^{1/2}$, 19.0 $(MPa)^{1/2}$ and 20.3 $(MPa)^{1/2}$, respectively.[50] A disordered morphology was obtained under toluene vapor annealing, as shown in Fig. 5-3(b). Since toluene is not a good solvent for the major block, P2VP, the chain mobility is limited by solvent interaction between toluene and P2VP[51] which impedes microphase separation. Polar

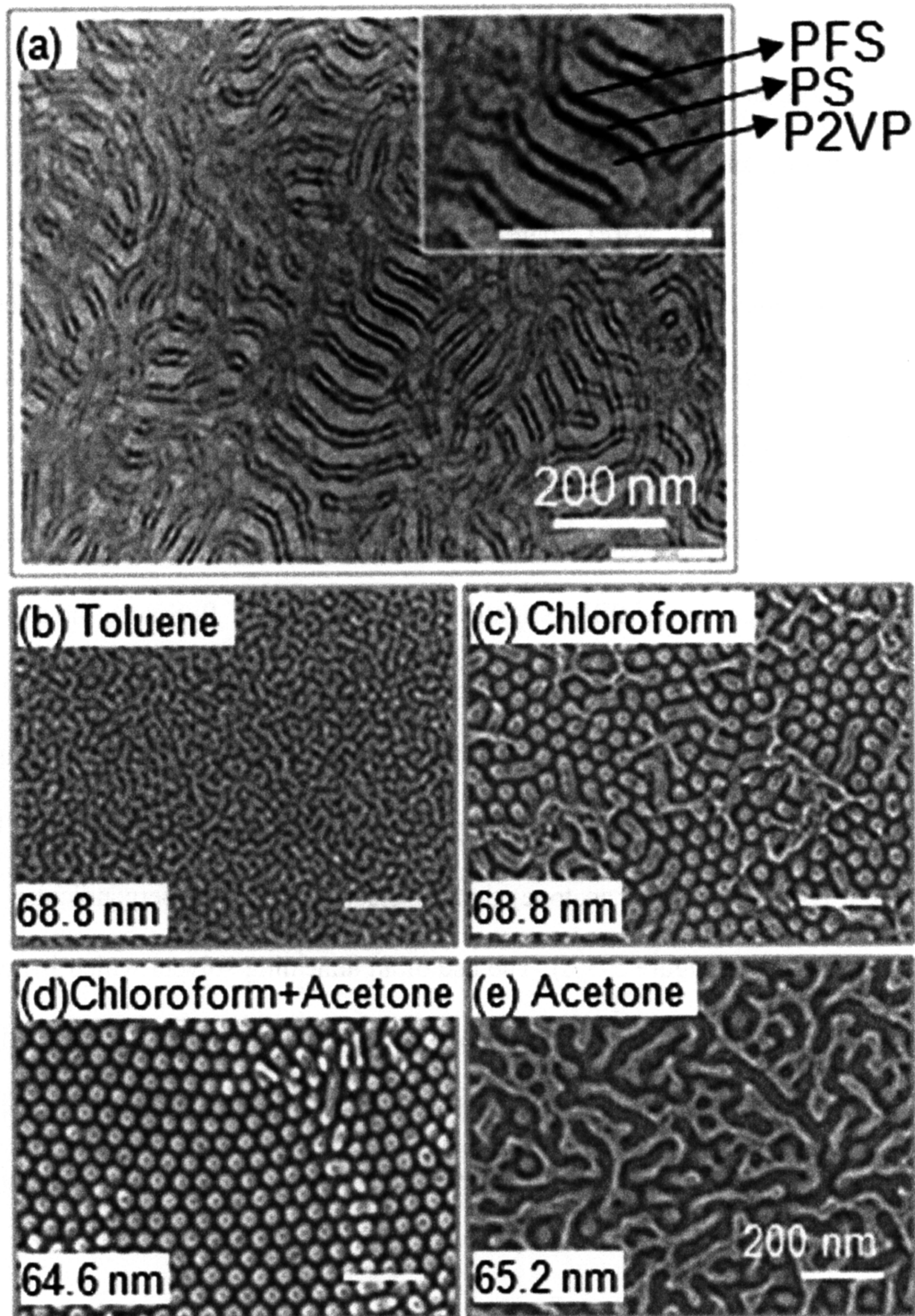

Figure 5-3 (a) Bright field TEM image of the bulk morphology of the PS-*b*-PFS-*b*-P2VP triblock terpolymer. TEM image is provided by Jessica Gwyther (b)-(e) SEM images of thin films of PS-*b*-PFS-*b*-P2VP on Si after annealing in (b) toluene vapor (c) chloroform vapor (d) mixed solvent vapor of chloroform and acetone (e) acetone vapor for 4 hours at room temperature, followed by etching with oxygen RIE to remove the PS and P2VP.

solvents, chloroform and acetone, have a preferential affinity for the P2VP block and facilitate microphase separation, as shown in Fig. 5-3(c)-(e). However, acetone is a non-solvent for PS and PFS so a pure acetone anneal gives poorly ordered microdomains (Fig. 5-3(e)). In addition, comparing Fig. 5-3(d) to Fig. 5-3(c), there are some regions in 5-3(c) that are still in the disordered state after annealing in chloroform. Acetone has a larger polar component of the solubility parameter compared to chloroform, and a mixture of acetone and chloroform (Fig. 5-3(d)) gave the best microphase separation.

The microdomain orientation at the air interface is influenced by the surface energies of the blocks. The surface energy of PS is slightly lower than that of PFS according to the XPS measurements from which show the surface enrichment of polystyrene in PS-*b*-PFS films after thermal annealing at 160°C for 2 days.[52] The surface energy of PS (39 mNm^{-1}) and much lower than P2VP (47 mNm^{-1}).[53] As a result, the air interface is selective to PS and PFS. Using an annealing solvent (chloroform plus acetone) that is selective to P2VP, perpendicular cylinders were obtained, as shown in Figure 5-3(d). The use of an annealing solvent which is preferential to the high surface energy block illustrates the balance between the polymer-solvent affinity and surface energy of the swollen blocks.[49] Solvent annealing is used both to provide the chain mobility for microphase separation and to promote orientation of the cylinders perpendicular to the film plane.

Figure 5-4 shows the three dimensional SFP_{94} microdomain structure with 64.6-65.9 nm thick films annealed in either chloroform (Fig. 5-4(a)-(c)) or a mixture of chloroform and acetone (Fig.5-4(d)-(f)) followed by etching to remove both PS and P2VP. Figures 5-4(a) and 5-4(d) show the top view, in which the ring-shaped PFS microdomains suggest a vertical alignment

of cylinders. The center-to-center distance between the cylinders is 53.9 nm, which is consistent with the bulk TEM data (Figure 5-3(a)) and the diameters of the core and shell cylinders are 10.7 nm and 33 nm, respectively.

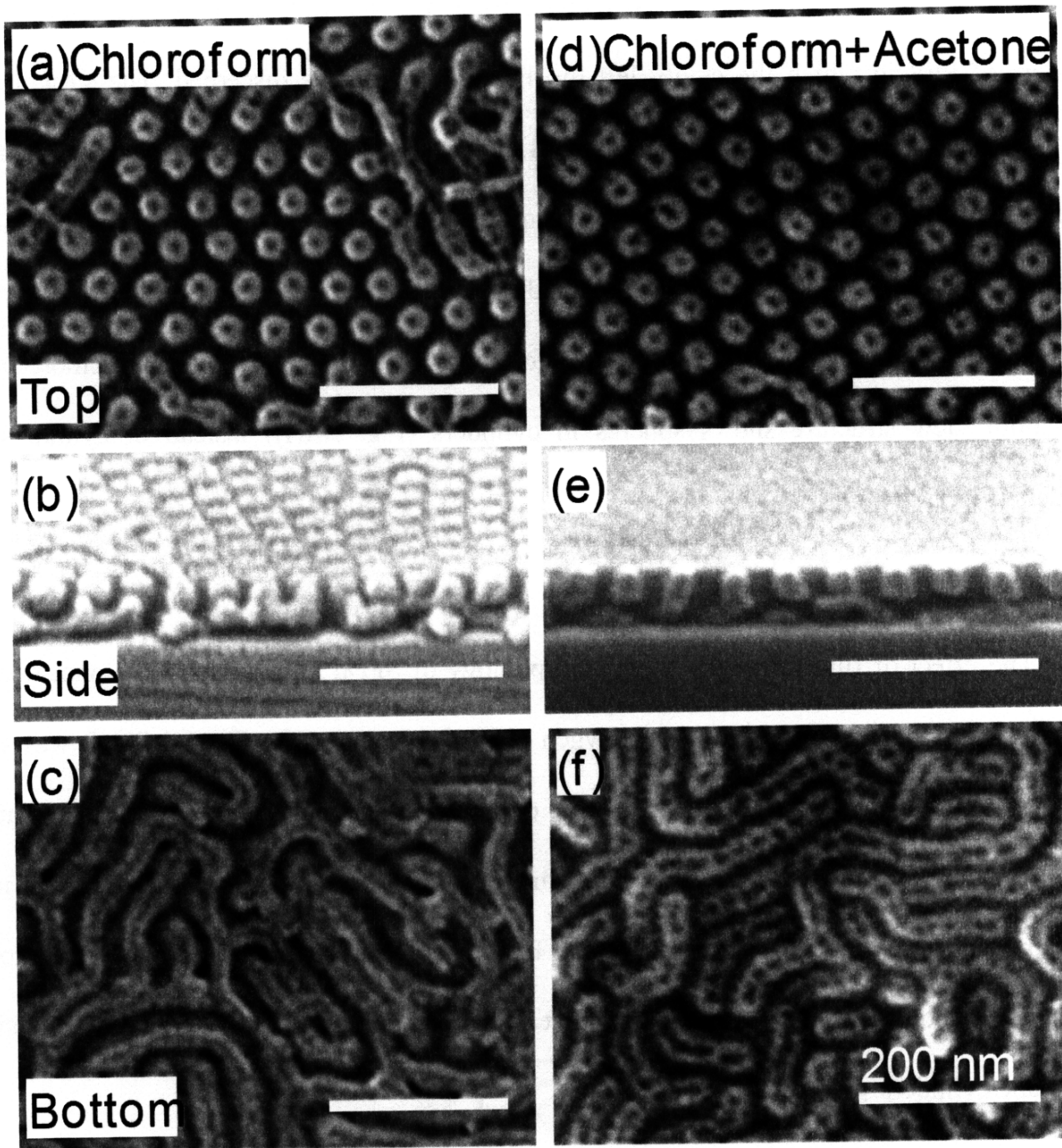

Figure 5-4 SEM images of thin films of PS-*b*-PFS-*b*-P2VP on Si after annealing in (a)-(c) chloroform and (d)-(f) a mixed solvent vapor of chloroform and acetone for 4 hrs at room temperature, followed by etching with oxygen RIE to remove the PS and P2VP. (a)(d) Plan view (b)(e) Side view (c)(f) Bottom view.

However, as shown in the cross-sectional view (Fig. 5-4(b) and Fig. 5-4(e)), the core-shell cylinders are only aligned vertically close to the top surface of the film. The film close to the substrate shows in-plane cylinders, and this is confirmed by the view of the bottom of the film in Fig. 5-4(c) and Fig. 5-4(f). This suggest that the substrate is in contact with hemi-cylinders of PFS in which the cavity left by the PS core can be discerned. The structure is therefore assumed to consist of in-plane PFS-PS cylinders at the substrate interface, with either vertical cylindrical PFS-PS 'chimneys' protruding from them (Fig. 5-4(b)), or vertical PFS-PS cylinders which terminate above the hemicylinders (Fig. 5-4(e)). Furthermore, because the PS core swells less in the mixed solvent of chloroform and acetone compared to pure chloroform, the bottom view structure shows spheres in cylinders (Fig. 5-4(f)) instead of cylinders in cylinders (Fig. 5-4(c)).

5.5.2 Effect of film thickness

The effect of film thickness on the morphology of SFP_{94} films which were annealed in chloroform vapor then etched using an oxygen plasma to remove the PS and P2VP was also studied. At 63.4 nm thickness, the cylinders are oriented perpendicular to the top surface, but as the thickness decreases to 54 and 46.9 nm, a mixed orientation is observed, and at 36.8 nm, irregular in-plane cylinders are observed (see Figure 5-5). This is consistent with the cross-sectional morphology of Fig. 5-4, indicating that in thin films the substrate wetting layer consists of in-plane cylinders.

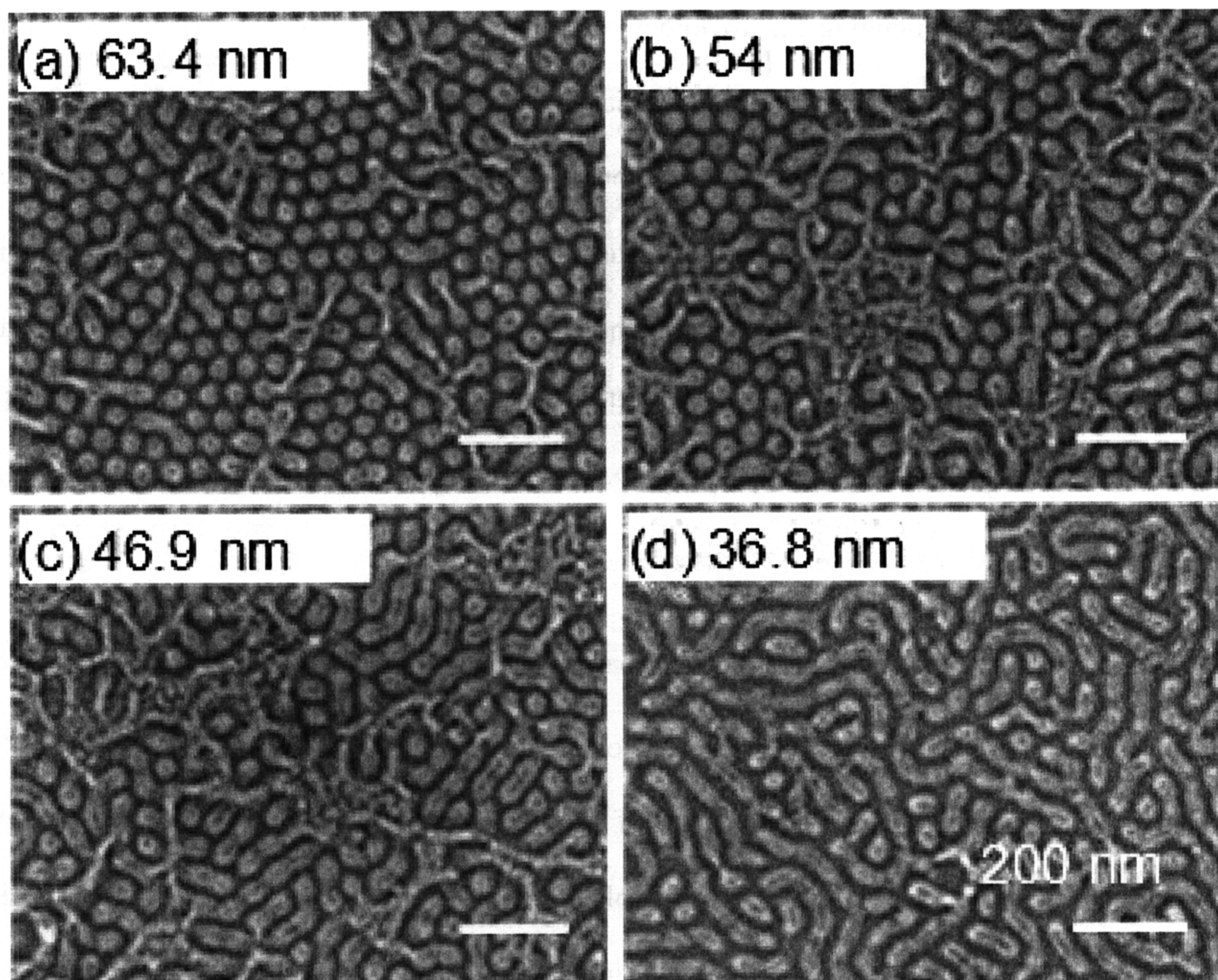

Figure 5-5 SEM images of thin PS-*b*-PFS-*b*-P2VP films with different thickness, after annealing in chloroform vapor, then etching with oxygen plasma. The as-spun film thicknesses were (a) 63.4 nm (b) 54 nm(c) 46.9 nm and (d) 36.8 nm.

5.5.3 Effect of substrate chemistry

The relative affinity of the substrate for each of the blocks is expected to control the morphology of the microdomains at the film-substrate interface, as seen in other systems such as films formed on chemically patterned substrates.[54] In order to obtain out-of-plane cylinders, the substrate should be energetically neutral to the microdomains of the block copolymer. This can be readily accomplished for a diblock copolymer, for example by the use of a random copolymer

brush[55] but is more challenging for a triblock terpolymer. Different hydroxy-terminated brush layers were employed to examine the interfacial interactions between the substrate and SFP_{94} annealed in a mixed solvent of chloroform/acetone. The substrate was SiO_2 functionalized with a PS-OH brush, a PFS-OH brush, a P2VP-OH brush layer or without a brush. A mixed orientation is formed in the substrate with the PS-OH brush layer with some out-of-plane cylinders, vertical alignment of the cylinders is primarily seen with a few short in-plane cylinders for the PFS-OH brush and only in-plane cylinders for the P2VP-OH brush layer, as does the uncoated substrate (see Figure 5-6(a)-(d)).

Surface energy is related to solubility parameter, and the order of the surface energies γ of the three different brushes is $\gamma_{PS\text{-}OH} < \gamma_{PFS\text{-}OH} < \gamma_{P2VP\text{-}OH}$. The most vertical cylinders were obtained by matching the surface energy of the PFS block, which has a surface energy intermediate between those of the other two blocks. The PFS diameter in the bottom view is slightly larger than that seen in the top view, indicating that the PFS volume fraction near the substrate is higher than that near the free surface. The similarity between using a P2VP-OH brush layer and an uncoated surface is attributed to the affinity of the polar P2VP block for both the P2VP-OH brush layer and the hydrophilic oxide surface.

5.6 Selective etching of the PS, PFS and P2VP blocks and pattern transfer

The successful use of block copolymers in lithography requires a good etch selectivity between the blocks, so that one or more of the blocks can be removed leaving the morphology of the remaining block(s) undisturbed. In the SFP_{94}, the PS and P2VP are removed easily using an oxygen reactive ion etch, leaving partly-oxidized organometallic PFS shells. This process is

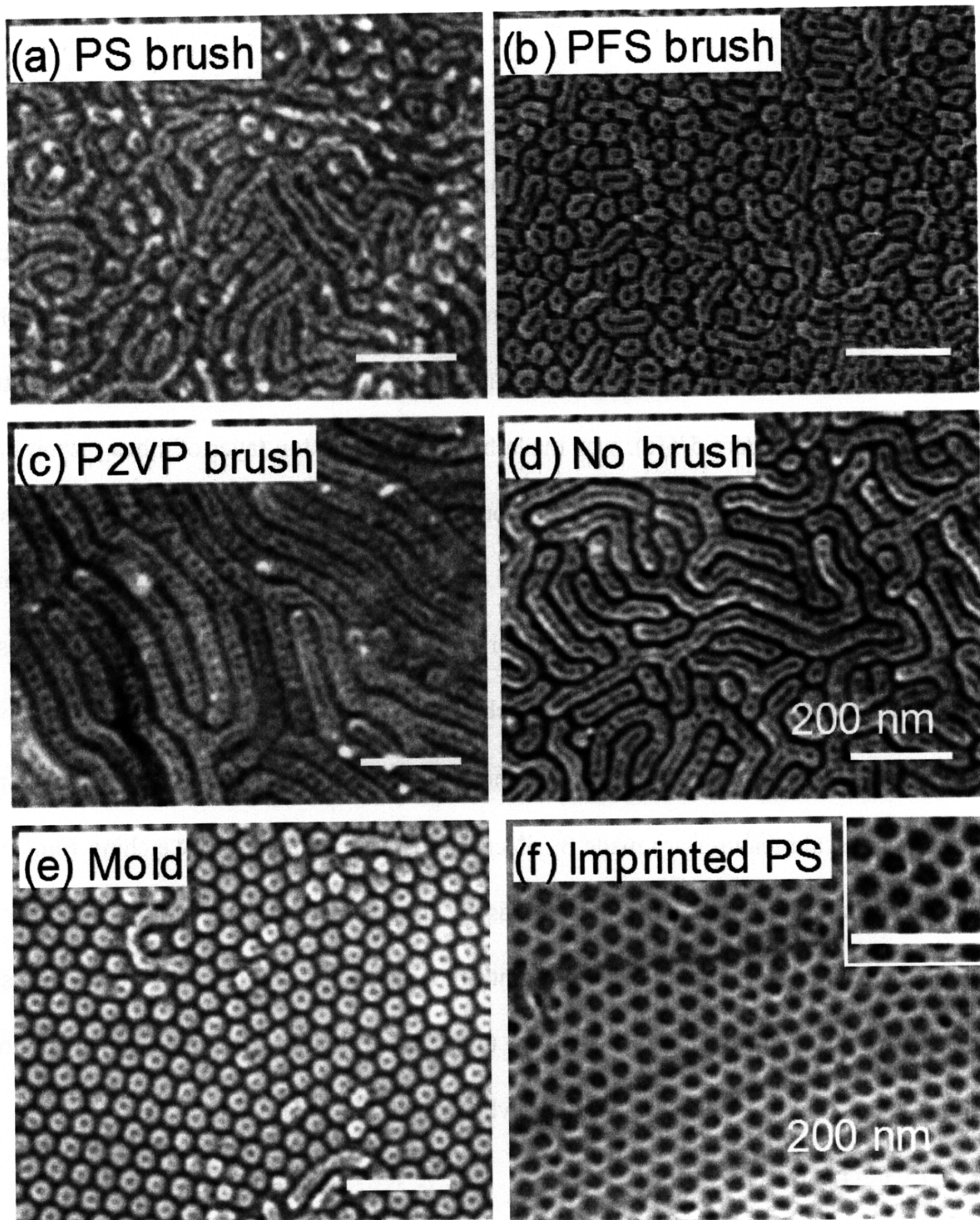

Figure 5-6 (a)-(d) SEM images of bottom view of thin films of PS-*b*-PFS-*b*-P2VP on chemically modified silica substrates after annealing in mixed vapor of chloroform and acetone, then dipping in HF, KOH and etching with oxygen plasma. (a) with PS-OH brush (b) with PFS-OH brush (c) with P2VP brush (d) without brush. (e)-(f)Pattern transfer into a PS layer from a PS-*b*-PFS-*b*-P2VP film annealed in chloroform/acetone vapor for 4 hrs. (e) Mold (f) Imprinted PS layer.

simpler than that required for selectively etching triblock terpolymers with all organic blocks.[15, 16]

The remaining PFS could be used as a mask for pattern transfer into functional materials, as already demonstrated in PS-PFS diblock copolymers.[37] However, if the PFS cylinders do not span the entire film thickness, as observed for most of the annealing conditions described here, this process cannot be used. Instead, an imprinting process was used to replicate the ring pattern. A mold, as shown in Figure 5-6(e), was made by sputtering a thin layer of silica on top of the etched triblock polymer film to provide additional mechanical stability. The mold was coated with a release layer and then pressed into a film of PS homopolymer using a cold isostatic press. Figure 5-6(f) shows holes of 29 nm in diameter with 15 nm diameter posts inside which is the inverse of the ring patterns after printing, which replicate the geometry of the mold very well. The imprinted area spans ~ 400μm^2 and the mold is reusable after printing. Typically imprint molds with nanoscale features are made by electron-beam lithography or by etching films made by molecular beam epitaxy.[56, 57] Making molds by the self-assembly of block copolymer can improve the cost and throughput of nanoimprint lithography. In addition, cold isostatic pressing requires a lower pressure (138 MPa at room temperature in this experiment) than minimum imprint pressures for polystyrene reported elsewhere, e.g. 280 MPa.[56]

5.7 Conclusion

PS-*b*-PFS-*b*-P2VP with a total molecular weight of 94,200 Da and a core-shell cylinder morphology was examined. Thin films of the polymer were formed by spin-coating and annealed to form self-assembled arrays of core-shell cylindrical structures of 50 nm period oriented perpendicular to the top surface of the film. The morphology and the microdomain orientation within the film were affected by the annealing conditions and substrate chemistry. Compared

these results to the ring arrays made from the triblock terpolymer with all organic segments, as discussed in Chapter 4, a vertical alignment of the core-shell cylinders at the air surface were both achieved by a combination of thickness control and annealing in a solvent vapor which is selective to the highest surface energy block. Although the Si substrate wetting layer consists of in-plane PS-PFS cylinders in this case, the most vertical alignment of the cylinders was obtained by applying a brush layer which has a surface energy intermediate between those of the other two blocks. The PS core and P2VP matrix blocks were partly removed simultaneously using oxygen reactive ion etching, and the pattern of 33 nm diameter, 11 nm wide PFS rings, which remained intact due to high etch resistance of the Si-containing middle block, and was transferred into a PS layer by imprinting, making this a useful system for self-assembled nanolithography.

Reference

1. Park, M.; Harrison, C.; Chaikin, P. M.; Register, R. A.; Adamson, D. H. *Science* **1997,** 276, (5317), 1401-1404.
2. Park, C.; Yoon, J.; Thomas, E. L. *Polymer* **2003,** 44, (22), 6725-6760.
3. Segalman, R. A. *Materials Science and Engineering: R: Reports* **2005,** 48, (6), 191-226.
4. Darling, S. B. *Progress in Polymer Science* **2007,** 32, (10), 1152-1204.
5. Black, C. T.; Guarini, K. W.; Milkove, K. R.; Baker, S. M.; Russell, T. P.; Tuominen, M. T. *Applied Physics Letters* **2001,** 79, (3), 409-411.
6. Naito, K. H., H.; Sakurai, M.; Kamata, Y.; Asakawa, K. *IEEE Transactions Magnetics* **2002,** 38, (5), 1949-1951.
7. Deng, T.; Chen, C.; Honeker, C.; Thomas, E. L. *Polymer* **2003,** 44, (21), 6549-6553.
8. Black, C. T. *Applied Physics Letters* **2005,** 87, (16), 163116-3.
9. Castaño, F. J.; Morecroft, D.; Jung, W.; Ross, C. A. *Physical Review Letters* **2005,** 95, (13), 137201-4.
10. Podbielski, J.; Giesen, F.; Grundler, D. *Physical Review Letters* **2006,** 96, (16), 167207-4.
11. Miller, M. M.; Prinz, G. A.; Cheng, S. F.; Bounnak, S. *Applied Physics Letters* **2002,** 81, (12), 2211-2213.
12. Aharonov, Y.; Bohm, D. *Physical Review* **1959,** 115, (3), 485-491.
13. Yu, L. W.; Chen, K. J.; Song, J.; Xu, J.; Li, W.; Li, X. F.; Wang, J. M.; Huang, X. F. *Physical Review Letters* **2007,** 98, (16), 166102-4.
14. Lévy, L. P.; Dolan, G.; Dunsmuir, J.; Bouchiat, H. *Physical Review Letters* **1990,** 64, (17), 2074-2077.
15. Guo, S.; Rzayev, J.; Bailey, T. S.; Zalusky, A. S.; Olayo-Valles, R.; Hillmyer, M. A. *Chemistry of Materials* **2006,** 18, (7), 1719-1721.
16. Chuang, V. P.; Ross, C. A.; Bilalis, P.; Hadjichristidis, N. *ACS Nano* **2008,** 2, (10), 2007-2014.
17. Bang, J.; Kim, S. H.; Drockenmuller, E.; Misner, M. J.; Russell, T. P.; Hawker, C. J. **2006,** 128, (23), 7622-7629.
18. Ludwigs, S.; Boker, A.; Voronov, A.; Rehse, N.; Magerle, R.; Krausch, G. *Nature Materials* **2003,** 2, (11), 744-747.
19. Nelson, J. M.; Primrose, A. P.; Hartle, T. J.; Allcock, H. R.; Manners, I. **1998,** 31, (3), 947-949.
20. Allcock, H. R.; Cho, S. Y.; Steely, L. B. **2006,** 39, (24), 8334-8338.
21. Rossi, N. A. A.; Jones, R. G.; Holder, S. J. *Journal of Polymer Science Part A: Polymer Chemistry* **2003,** 41, (1), 30-40.
22. Popescu, D. C.; Rossi, N. A. A.; Yeoh, C.-T.; Durand, G. G.; Wouters, D.; Leclere, P. E. L. G.; Thune, P.; Holder, S. J.; Sommerdijk, N. A. J. M. *Macromolecules* **2004,** 37, (9), 3431-3437.
23. Teodorescu, M.; Mîndru, C.; Draghici, C. *European Polymer Journal* **2006,** 42, (10), 2247-2253.
24. Shefelbine, T. A.; Vigild, M. E.; Matsen, M. W.; Hajduk, D. A.; Hillmyer, M. A.; Cussler, E. L.; Bates, F. S. *Journal of American Chemical Society* **1999,** 121, 8457-8465.
25. Hardy, C. M.; Bates, F. S.; Kim, M.-H.; Wignall, G. D. *Macromolecules* **2002,** 35, (8), 3189-3197.
26. Stoenescu, R.; Meier, W. *Chemical Communications* **2002,** 24, 3016-3017.

27. Kulbaba, K.; Manners, I. *Macromolecular Rapid Communications* **2001,** 22, (10), 711-724.
28. Ni, Y.; Rulkens, R.; Manners, I. *Journal of the American Chemical Society* **1996,** 118, (17), 4102-4114.
29. Rider, D. A.; Cavicchi, K. A.; Power-Billard, K. N.; Russell, T. P.; Manners, I. *Macromolecules* **2005,** 38, (16), 6931-6938.
30. Lammertink, R. G. H.; Hempenius, M. A.; Thomas, E. L.; Vancso, G. J. *Journal of Polymer Science Part B: Polymer Physics* **1999,** 37, (10), 1009-1021.
31. Kloninger, C.; Rehahn, M. *Macromolecules* **2004,** 37, (22), 8319-8324.
32. Resendes, R.; Massey, J.; Dorn, H.; Winnik, M. A.; Manners, I. *Macromolecules* **2000,** 33, (1), 8-10.
33. Power-Billard, K. N.; Spontak, R. J.; Manners, I. *Angewandte Chemie International Edition* **2004,** 43, (10), 1260-1264.
34. Bellas, V.; Rehahn, M. *Angewandte Chemie International Edition* **2007,** 46, (27), 5082-5104.
35. Lammertink, R. G. H.; Hempenius, M. A.; Enk, J. E. v. d.; Chan, V. Z. H.; Thomas, E. L.; Vancso, G. J. *Advanced Materials* **2000,** 12, (2), 98-103.
36. Lu, J.; Chamberlin, D.; Rider, D. A.; Liu, M.; Manners, I.; Russell, T. P. *Nanotechnology* **2006,** 17, (23), 5792-5797.
37. Cheng, J. Y.; Ross, C. A.; Chan, V. Z. H.; Thomas, E. L.; Lammertink, R. G. H.; Vancso, G. J. *Advanced Materials* **2001,** 13, (15), 1174-1178.
38. Whittell, G. R.; Manners, I. *Advanced Materials* **2007,** 19, (21), 3439-3468.
39. Kloninger, C.; Rehahn, M. *Macromolecular Chemistry and Physics* **2007,** 208, (8), 833-840.
40. Wang, X. S.; Winnik, M. A.; Manners, I. *Macromolecules* **2002,** 35, (24), 9146-9150.
41. Wang, H.; Winnik, M. A.; Manners, I. *Macromolecules* **2007,** 40, (10), 3784-3789.
42. Kloninger, C.; Rehahn, M. *Macromolecules* **2004,** 37, (5), 1720-1727.
43. Presa, A.; Manners, I. *in preparation* **2009.**
44. Sugiyama, M.; Shefelbine, T. A.; Vigild, M. E.; Bates, F. S. *Journal of Physical Chemistry B* **2001,** 105, (50), 12448-12460.
45. Kulbaba, K.; MacLachlan, M. J.; Evans, C. E. B.; Manners, I. *Macromolecular Chemistry and Physics* **2001,** 202, (9), 1768-1775.
46. Ludwigs, S.; Böker, A.; Abetz, V.; Müller, A. H. E.; Krausch, G. *Polymer* **2003,** 44, (22), 6815-6823.
47. Rider, D. A.; Manners, I. *Polymer Reviews* **2007,** 47, (2), 165-195.
48. Guérin, G.; Raez, J.; Wang, X.-S.; Manners, I.; Winnik, M., Polyferrocenylsilane Block Copolymers: Nanotubes and Nanowires through Self-Assembly. In *Progress in Colloid and Polymer Science*, Springer Berlin: Heidelberg, 2006; Vol. 132, pp 152-160.
49. Cavicchi, K. A.; Berthiaume, K. J.; Russell, T. P. *Polymer* **2005,** 46, (25), 11635-11639.
50. Brandrup, J.; Immergut, E. H.; Grulke, E. A.; Abe, A.; Bloch, D. R., *Polymer Handbook (4th Edition)*. Wiley-Interscience: New York, 1999; p III/59-III/61.
51. Jung, Y. S.; Ross, C. A. *Advanced Materials* **2009,** in press.
52. Lammertink, R. G. H.; Hempenius, M. A.; Vancso, G. J.; Shin, K.; Rafailovich, M. H.; Sokolov, J. *Macromolecules* **2001,** 34, (4), 942-950.

53. Lin, Y.; Boker, A.; He, J.; Sill, K.; Xiang, H.; Abetz, C.; Li, X.; Wang, J.; Emrick, T.; Long, S.; Wang, Q.; Balazs, A.; Russell, T. P. *Nature* **2005,** 434, (7029), 55-59.
54. Heier, J.; Kramer, E. J.; Walheim, S.; Krausch, G. *Macromolecules* **1997,** 30, (21), 6610-6614.
55. Huang, E.; Pruzinsky, S.; Russell, T. P.; Mays, J.; Hawker, C. J. *Macromolecules* **1999,** 32, (16), 5299-5303.
56. Harrer, S.; Strobel, S.; Scarpa, G.; Abstreiter, G.; Tornow, M.; Lugli, P. *IEEE Transactions on Nanotechnology* **2008,** 7, (3), 363-370.
57. Austin, M. D.; Ge, H.; Wu, W.; Li, M.; Yu, Z.; Wasserman, D.; Lyon, S. A.; Chou, S. Y. *Applied Physics Letters* **2004,** 84, (26), 5299-5301.

Chapter 6 Templated self-assembly of square arrays from an ABC triblock terpolymer

6.1 Introduction

As we have discussed, block copolymers have been used extensively to construct well-controlled nanostructures and devices. [1-8] Self-assembling systems including block copolymers often form close-packed structures with hexagonal symmetry. There are applications where it is desirable to form a square array of features, for example arrays of microelectronic vias, and a square symmetry pattern is one of the essential device geometries identified by the Semiconductor Industry Association.[9] This symmetry cannot be achieved by a coil-coil diblock copolymer, but has been observed in polymer systems with certain interactions, such as ABC triblock terpolymers[10, 11], comb-coil diblock copolymers[12], T-shaped liquid crystals[13] or DNA/dentrimer complexes[14]. However, most of these studies have been focused on bulk morphologies. Recently, self-assembled thin films with square symmetry was demonstrated by Park et al. using a diblock copolymer on a chemically nanopatterned substrate with the same periodicity as the copolymer[15], by Tang et al. using blended A-*b*-B and B'-*b*-C diblock copolymers in which the B and B' blocks interact by hydrogen bonding[16] and by BCC packing of a multilayer film of spheres in a spherical triblock terpolymer which shows a square arrangement on the top layer.[17]

In this chapter, we describe the synthesis and thin film self-assembly of a new triblock terpolymer, polyisoprene-*b*-polystyrene-*b*-polyferrocenylsilane (PI-*b*-PS-*b*-PFS), with a thin film morphology consisting of PI and PFS cylinders packed in a square symmetry in a matrix of PS. The PS and P2VP are selectively removed to leave square arrays of etch-resistant PFS dots, and these dot patterns are transferred into 30 nm thick silica. This approach generates square symmetry patterns without the requirement for substrate nanopatterning, and the high etch

selectivity between the organic and organometallic blocks simplifies pattern transfer. Moreover, we demonstrate that the square patterns can be templated using shallow topographic trenches, and the orientation of the templated patterns is controlled by the chemistry of the trench surfaces.

6.2 Experimental methods

6.2.1 Triblock Terpolymer Synthesis: Equipment and Materials

The synthesis and bulk morphology part of the experiment were done by Ms. Jessica Gwyther in Professor Ian Manner's group at University of Bristol. Ms. Gwyther supplied the text and data in section 6.2.1 and 6.2.2. Ferrocene pellets were purchased from Octel Germany and ground to a fine powder before use. N,N,N',N'-tetramethylethylenediamine (tmeda) from Fisher was dried over CaH_2 and distilled under reduced pressure. ^{n}Butyllithium (^{n}BuLi) purchased from Acros (1.6 M in hexanes) was used as received. ^{sec}Butyllithium (^{sec}BuLi) purchased from Aldrich (1.4 M in hexanes) used as received. Hexanes and diethylether were purified using Anhydrous Engineering double alumina and alumina/copper catalyst drying columns. Dichloroethylmethylsilane from Aldrich was distilled prior to use. Isoprene monomer purchased from Acros was dried over CaH_2 and distilled under reduced pressure followed by a second distillation from ^{n}BuLi. THF was distilled under reduced pressure from Na/benzopheneone. Styrene monomer purchased from Acros was dried over CaH_2 and subsequently distilled twice under reduced pressure. Cyclohexane was dried over CaH_2 before distillation. Methanol was deoxygenated by freeze, pump and thaw method.

Reagent distillations and monomer preparation was carried out on a glass vacuum line under nitrogen. Polymerisations were conducted in an Mbraun glove box in an inert argon atmosphere.

^{1}H and ^{13}C spectra were obtained using JEOL Lambda 300 and ECP (Eclipse) spectrometers.

Gel Permeation Chromatography (GPC) was carried out on a Viscotek GPCmax chromatograph equipped with a triple detector array. A flow rate of 1.0 ml/min was used with THF as the eluent.

Thin slices of bulk samples were prepared using an ultramicrotome and collected on carbon coated copper grids. Transmission electron microscopy (TEM) images were obtained using a JEOL JEM 1200 EX microscope.

6.2.2 Synthesis and Characterization of PI-b-PS-b-PFS Triblock Terpolymer

Synthesis of ethylmethylsilaferrocenophane monomer was carried out as previously described.[18, 19] Isoprene (1.26 g, 18.50 mmol) was dissolved in THF (4.15 ml) and cooled to 0°C before initiating with ^{sec}BuLi (43 µl, 0.06 mmol). After 2 h an aliquot of the living PI solution was removed from the glove box and quenched with degassed methanol. The PI homopolymer was precipitated in rapidly stirring methanol and dried at 40°C in a vacuum oven overnight. Molecular weight was determined by triple detection GPC.

The remaining living PI solution was allowed to reach room temperature before styrene (1.45 g, 13.92 mmol) dissolved in cyclohexane (5.41 ml) was added. The polymerisation was allowed to proceed for 1 h, after which time an aliquot of the living PI-*b*-PS diblock copolymer solution was removed and quenched with degassed methanol. The diblock copolymer was precipitated and dried as the PI homopolymer.

Ethylmethylferrocenophane monomer (0.15 g, 0.59 mmol) in THF (1.00 ml) was added to the remaining living PI-*b*-PS diblock copolymer solution. After 1 h the polymerisation was quenched with degassed methanol and the PI-*b*-PS-*b*-PFS triblock terpolymer precipitated into rapidly stirring methanol and dried at 40°C in a vacuum oven overnight. A yield of 1.03 g (87%) was obtained.

^{1}H NMR ($CDCl_3$ δ = 7.26 with TMS δ = 0.00) δ = 0.43 (s, Si-CH_3), 0.94 (q, br, Si-CH_2CH_3), 1.05 (t, br, Si-CH_2CH_3), 1.20 – 2.21 (br, alkyl) 4.00 (m, Cp) 4.21 (m, Cp), 4.59 – 5.68 (br, vinyl) 6.36 – 7.10 (br, $CH_2CH(Ph)$).

The preparation of PI-*b*-PS-*b*-PFS triblock terpolymer was carried out via a sequential living anionic polymerization. The synthetic procedure is outlined in scheme 6-1.

The polymer was characterized by ^{1}H NMR and GPC. The ^{1}H NMR spectrum, as shown in Figure 6-1 was used to determine the relative block ratios, and hence volume fractions, of the triblock terpolymer by integration of the vinyl peaks of the PI block, the aromatic protons of the phenyl ring of the PS block and the PFS cyclopentadienyl protons. The block volume fractions were found to be $\phi_{PI} = 0.25$, $\phi_{PS} = 0.65$ and $\phi_{PFS} = 0.10$ using densities of 0.92 g/ml for PI,[20] 1.05 g/ml for PS[20] and 1.29 g/ml for PFEMS.[18, 21] The total molecular weight of the polymer was found to be M_n = 82,000 Da, with a narrow polydispersity PDI = 1.04 and yield 87%.

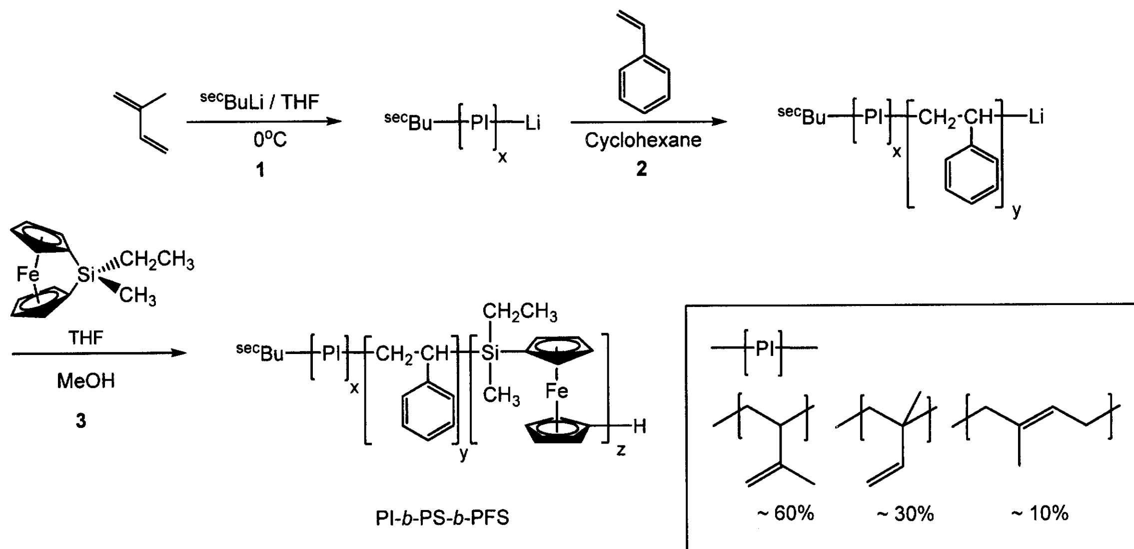

Scheme 6-1 Synthesis of PI-*b*-PS-*b*-PFS triblock terpolymer.

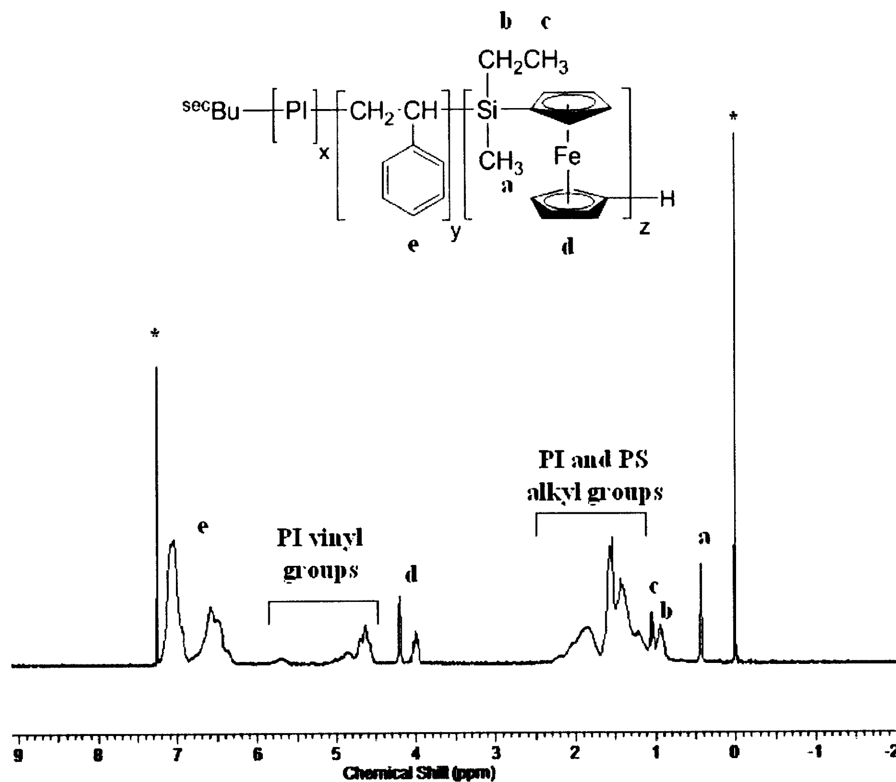

Figure 6-1 ^{1}H NMR spectrum of PI-*b*-PS-*b*-PFS in $CDCl_3$ and TMS, solvent denoted by *. This data is provided by Jessica Gwyther.

6.2.3 Thin film deposition and characterization

The thin film samples were prepared by spin coating of 0.8-1 wt% toluene solution of PI-*b*-PS-*b*-PFS on the Si substrates to form films with thickness of 29.7 nm to 68.1 nm, as determined by ellipsometry. Some substrates were chemically modified by spin-coating of 1wt% of hydroxyl-terminated PS (PS-OH (5kg/mol)) toluene solution onto Si which was previously coated with 50 nm SiO_2 by electron beam evaporation. PS-OH was purchased from Polymer Source. The PS homopolymer was covalently bonded to the substrate after heating and the remaining unbonded polymers were then rinsed away with toluene. The 30 nm deep Si gratings were made by recording a periodic pattern in a trilayer resist using a Lloyd's Mirror interference lithography system with a 325-nm-wavelength helium-cadmium laser,[22] combined with a series of reactive ion etching steps. The period of the grating was varied between 200 and 380 nm by changing the angle of incidence of the expanded laser beam on the substrate and an adjacent mirror.

After annealing the polymer film in chloroform vapor for 2.5 h at room temperature, oxygen reactive ion etching was used to partially remove the PI and PS domains to reveal the arrangement of PFS microdomains, which were imaged by SEM. To reveal the PI domains in SEM images, the samples were prepared by first staining in OsO_4 to increase the etch resistance of PI domains and then etching the polymer in an oxygen plasma.

6.3 Polymer design

Square-packed cylinders are expected to form in an ABC triblock terpolymer when the Flory-Huggins interaction parameter χ_{AC} between the A and C blocks is greater than χ_{AB} and χ_{BC}, and B is the major block.[23] This condition is met by the PI-*b*-PS-*b*-PFS system with volume fractions of 25%, 65%, 10%, considering that the solubility parameters of PI, PS, and PFS are 17

$(MPa)^{1/2}$, 18.5 $(MPa)^{1/2}$, 18.7 $(MPa)^{1/2}$, respectively.[24, 25] The total molecular weight of the material in this study is 82 kg/mol, and the triblock terpolymer will be denoted ISF_{82}.

6.4 Self assembly of PI-*b*-PS-*b*-PFS triblock terpolymers in bulk

Figure 6-2(c) shows a TEM image of the bulk morphology of pure PI-*b*-PS-*b*-PFS. The center-to-center distance between PFS domains is 41.1 nm. Without staining, there is very little contrast between PI and PS and thus all the dark dots in the image represent cross-sections through PFS cylinders. Every third one looks darker. The reason is unclear but it may be an artifact of microtoming. All of the images would have been taken from microtomed slices cut at the same angle. Therefore, it may be that due to the cutting angle some of the PFS domains were cut as different thickness to others making thicker regions look darker.

6.5 Thin film morphology on Si substrate

Figure 6-2(a,b,d,e) shows SEM images of the thin film morphologies of ISF_{82} after spin-coating and annealing. The PI and PS blocks were removed simultaneously by etching in an oxygen plasma to leave oxidized PFS features. For the pure triblock terpolymer, a film with a thickness of 29.4 nm showed regions of both hexagonal and square-packed PFS arrays (Fig. 6-2(a)). However, by blending the ISF_{82} with 17.9% by volume of PS homopolymer, square packed patterns were formed over the entire sample area studied (Fig. 6-2(b)). To confirm the locations of the PI microdomains in the ISF_{82}/PS blend, Figure 6-2(d) shows a sample that was stained with OsO_4 before etching in oxygen plasma. The alternating PI (grey) and PFS (white) domains form a checkerboard arrangement. Figure 6-2(f) shows an unstained sample in which only PFS domains remain after oxygen etching. The period of the PFS microdomains measured

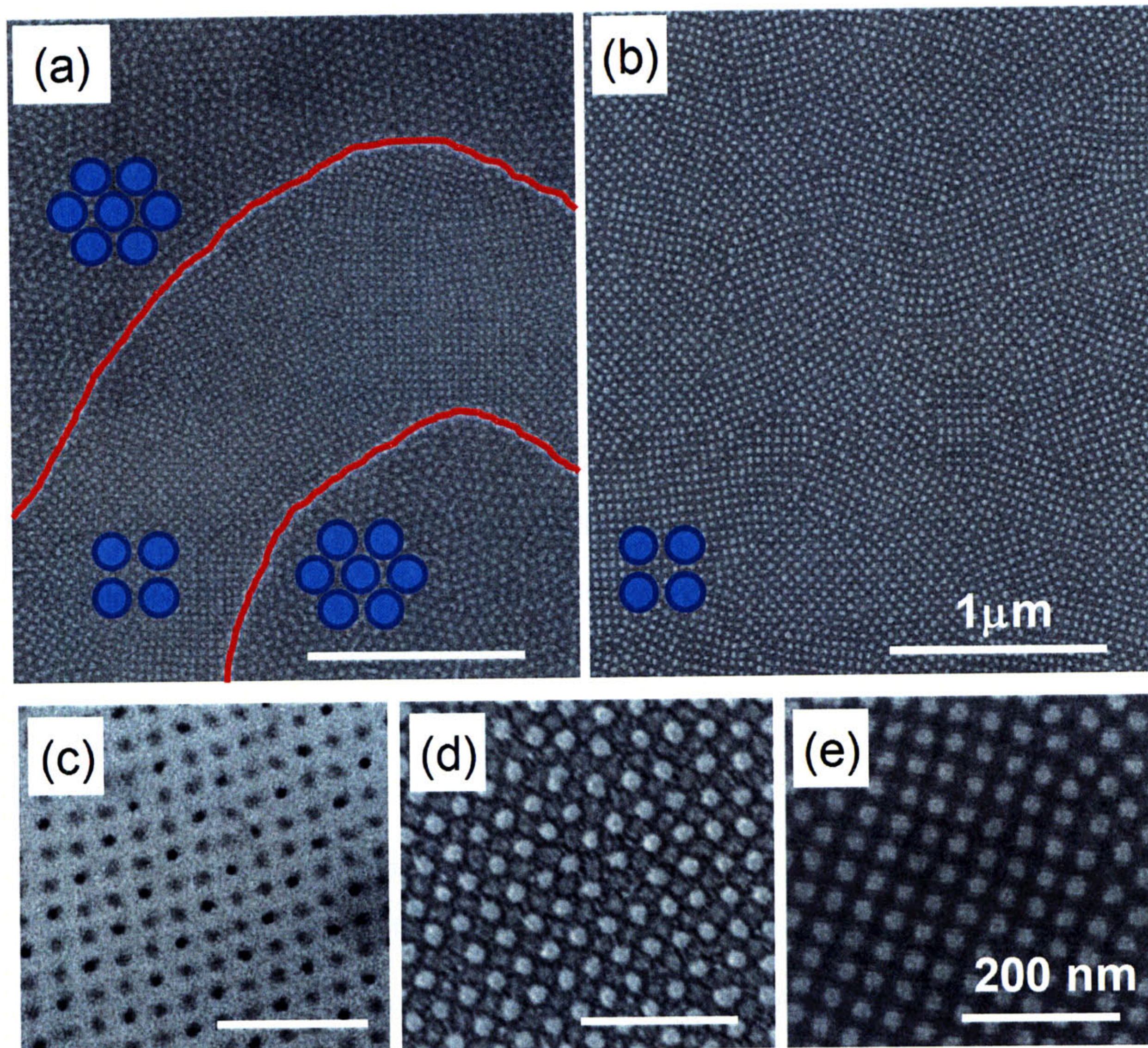

Figure 6-2 (c) Bright field TEM image of the bulk morphology of the pure PI-*b*-PS-*b*-PFS triblock terpolymer. (a)(b)(d)(e) SEM images of thin films of (a) pure PI-*b*-PS-*b*-PFS (b)(d)(e) blended PI-*b*-PS-*b*-PFS on Si after spin-coating and annealing in chloroform vapor for 2.5 hours at room temperature, followed by etching with oxygen RIE to remove both PI and PS blocks. (d) with an additional step of OsO_4 staining for 4 hrs before oxygen RIE, giving the PI higher resistance to an oxygen etch.

from the blended ISF thin film on Si is 40.5 nm, which is larger than that measured from the thin film unblended ISF_{82}(39.1 nm) due to the additional homopolymer.

ABC triblock terpolymers with a bulk morphology of interpenetrating square-packed A and C cylinders embedded in a B matrix have been studied theoretically[26, 27] and experimentally[10, 11]. Although hexagonal packing is optimum for a cylindrical morphology diblock copolymer, in a triblock terpolymer an alternating arrangement of A and C cylinders reduces the stretching of the chains and is more favorable in bulk.[27] However, in thin films of cylindrical ABC triblock terpolymers with vertical cylinders, both hexagonal and square packing were found, suggesting that the energy difference between them is small and sensitive to film thickness. The blending of PS homopolymer stabilizes the square array by filling the volume that otherwise would be filled by highly stretched terpolymer chains.[28]

To more closely examine the square array and hexagonal array, PI domains were preserved by staining in order to see their morphology. In Figure 6-3(a), the bright features represent PFS, the grey features represent PI and the dark features are PS. This figure shows that the square-packed PFS microdomains form an alternating arrangement with square-packed PI microdomains, as shown schematically in Figure 6-3(b). However, in the parts of the film with hexagonal packing, the film forms core-shell cylinders with a PFS core and PS shell in a PI matrix. (This sample also shows regions of in-plane orientation where alternating PFS and PI cylinders occur.) The formation of core-shell cylinders instead of alternating square-packed cylinders is attributed to the asymmetry between the χ parameters for PI-PS and PFS-PS. The interfacial energy can be lowered by having different curvatures of the two interfaces, stabilizing core-shell structures at the expense of alternating structures.[23, 29] Measurements of the area fractions of blended PI:PS:PFS from TEM images of stained samples prepared on membranes show that, for the square array PI:PS:PFS = 16.5:67:16.5 while for the hexagonally-packed core-shell cylinders PI:PS:PFS = 35:51:14. The volume fraction in the pure triblock terpolymer is

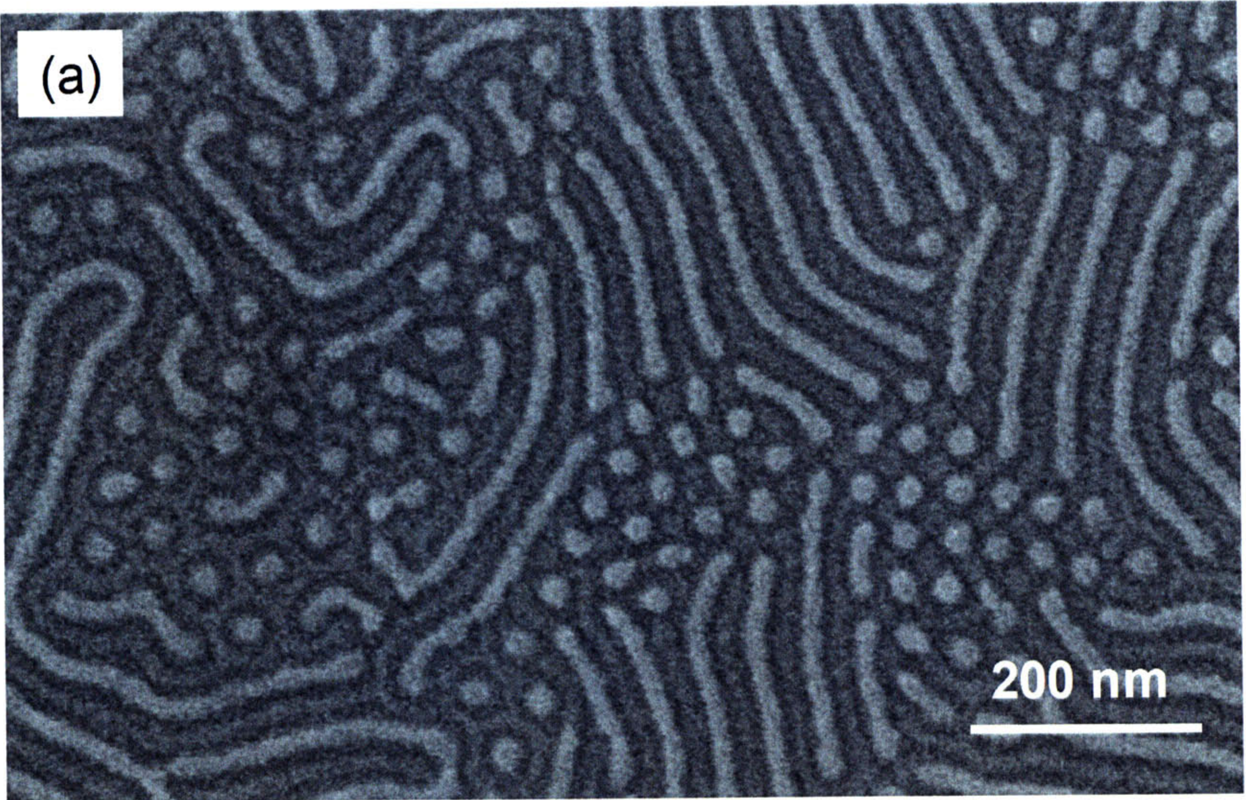

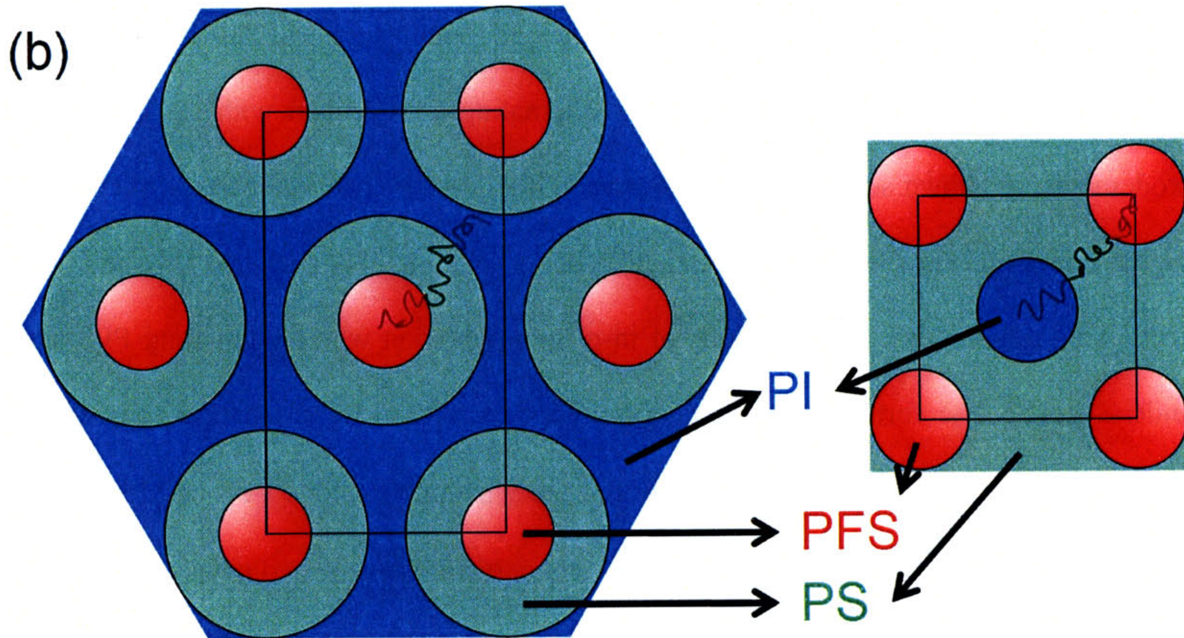

Figure 6-3 (a) a SEM image of pure PI-*b*-PS-*b*-PFS on Si after spin-coating and annealing in chloroform vapor for 2.5 hours at room temperature, followed by OsO_4 staining for 4 hrs and etching with oxygen RIE. The bright features represent PFS, the grey features represent PI and the dark features are PS.(b) schematic of hexagnol packed core-shell structure and square array.

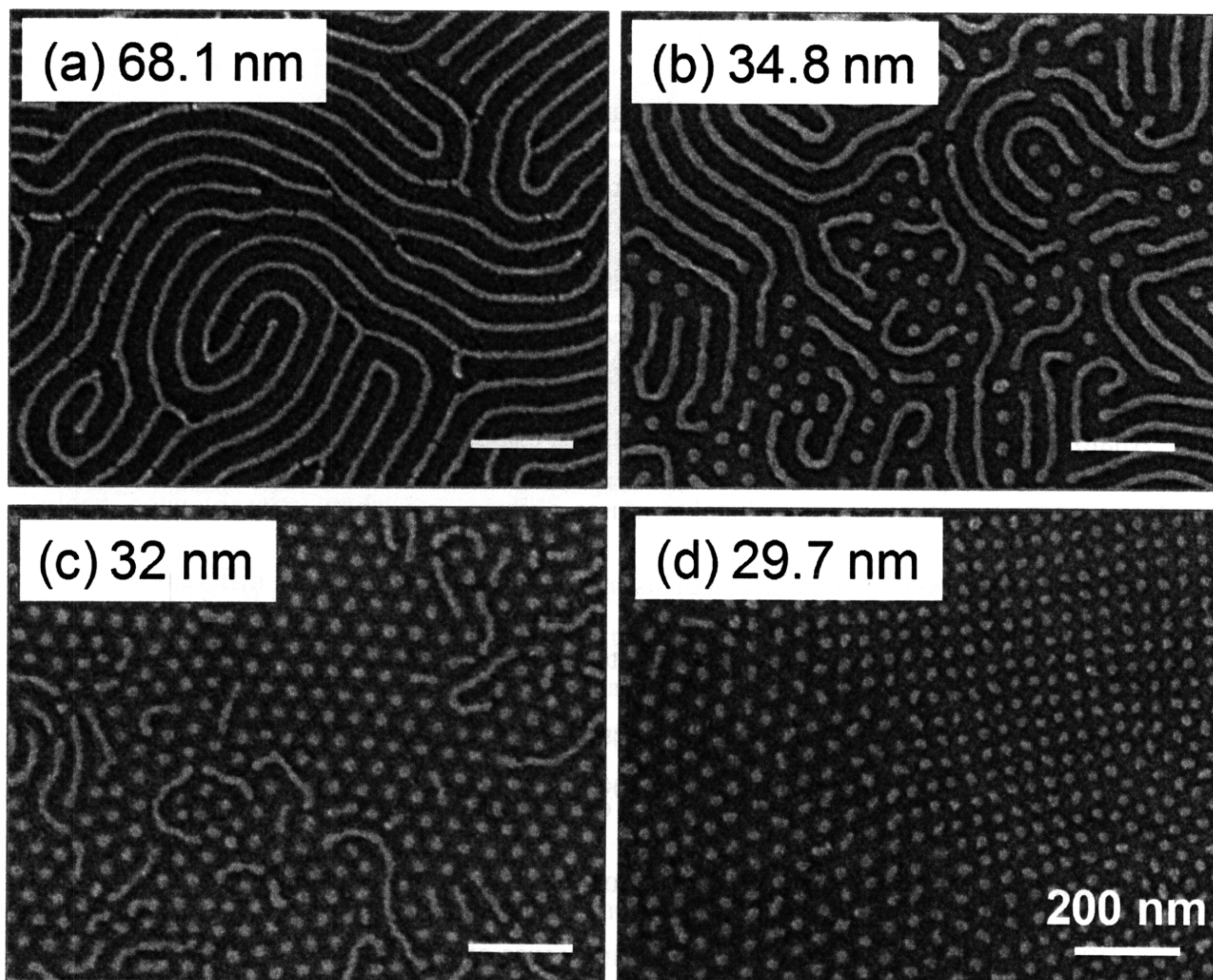

Figure 6-4 SEM images of pure PI-*b*-PS-*b*-PFS thin films on Si at different thickness after annealing, followed by etching with oxygen RIE. (a) 68.1 nm; (b) 34.8 nm;(c) 32 nm;(d) 29.7 nm.

25:65:10 while for the blend it is 16:78:6. By adding PS homopolymer, the square arrangement is promoted because it can accommodate more PS homopolymer.

Furthermore, the thickness effect was investigated in 68.1-29.7 nm thick films of unblended ISF_{82} which were spin-coated on oxidized Si substrates and annealed in chloroform vapor then etched with oxygen plasma to remove the PI and PS. The orientation of the microdomains depends on the film thickness. At 68.1 nm thickness, in-plane PFS cylinders are

obtained, but as the thickness decreases to 34.8 and 32 nm, a mixed orientation of in-plane cylinders and hexagonally-packed perpendicular cylinders is observed, and at 29.7 nm, perpendicular cylinders with both arrays of square and hexagonal symmetry are seen, as shown in Figure 6-4.

6.6 Templated assembly of blended PI-*b*-PS-*b*-PFS triblock terpolymer

Analogously to the topographical templating of diblock copolymers,[30] we templated the triblock terpolymer within topographical features. Figure 6-5 shows the blended triblock terpolymer self-assembled in templates consisting of shallow grooves of different widths. In contrast to a templated diblock copolymer,[31] the templated triblock terpolymer can vary not only the periodicity of its microdomains but their orientation within the trench. In templates without chemical functionalization, square arrays of PFS cylinders formed with the square axis primarily at 90° to the walls of the trench (Fig. 6-5(a)). However, when the templates were coated with a PS-brush, Figure 6-5(b), the PFS microdomain array was oriented primarily at 45° to the trench wall, although there is an increasing amount of 90° (less than 16% for widths of 235 nm) and other orientations as the groove width increases. The uncoated silica template attracts both PI and PFS, favoring an arrangement with the end blocks at the walls, while the PS-coated substrate favors an arrangement with the PS blocks present at the walls, illustrated in Fig. 6-5(c).

As the trench width increases, the number of rows of PFS microdomains increases in a stepwise manner. This is plotted vs. confinement width (W/P_0) for both the 90° and the 45° orientations in Fig. 6-5(d). P_0 is the equilibrium row spacing, which is 40.5 nm for this blended polymer in the 90-degree orientation and $40.5/\sqrt{2}$ in the 45-degree orientation. Both sets of data fit to a slope of 1, as expected, but the intercept on the horizontal axis is smaller for the 90° orientation. This intercept includes the thickness of the non-repeating brush layer(s) at the trench

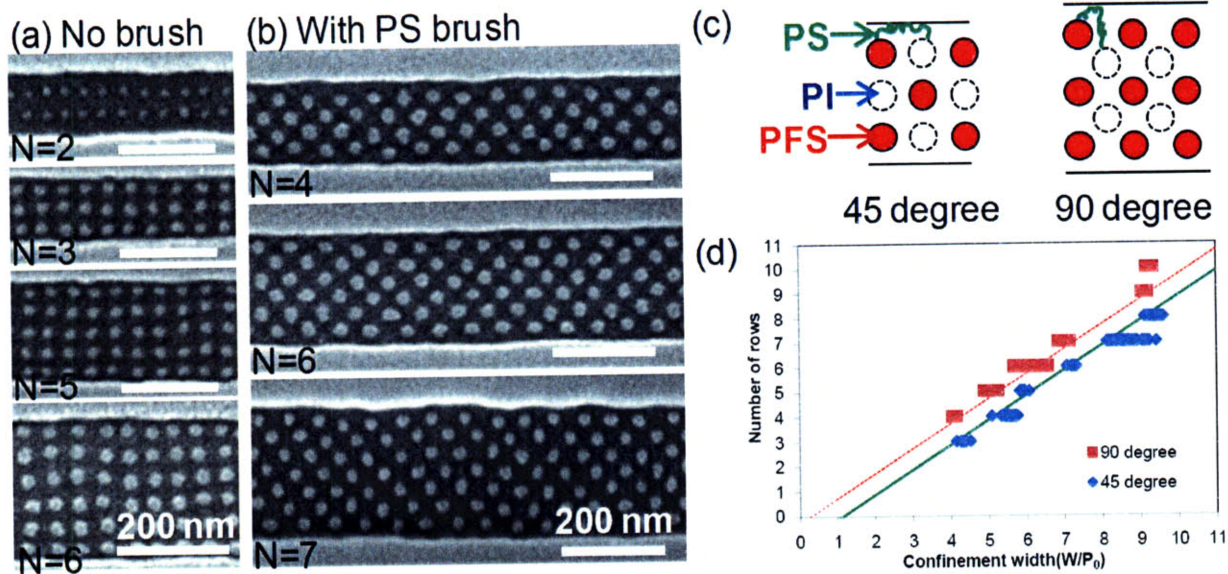

Figure 6-5 (a)(b) SEM images of templated assembly of blended PI-*b*-PS-*b*-PFS triblock terpolymer after annealing in chloroform vapor for 2.5 hours at room temperature, followed by etching with oxygen RIE to remove PI and PS domains.(a) with uncoated templates (b) with PS brushed templates. (c) Schematic of packing orientation of blended PI-*b*-PS-*b*-PFS triblock terpolymer in PS brushed templates. (d) A plot of number of rows vs. confinement width for both the 90° and the 45° orientations.

edge, which is expected to be only a few nm. The intercept for the 45° is larger than P_0 because it includes 2 half-row-spacings plus PS brush layers (~3-4 nm) at the two trench edges. The intercept for 90° is smaller than P_0 due to the presence of fewer triblock terpolymer chains at the trench edge, which also leads to a smaller domain size at the trench wall. In addition, in the 45° orientation, both end-blocks are at the same distance from the wall while in the 90° orientation, one of the blocks do not locate to the wall. Because the PS block in triblock terpolymer has to connect to the end blocks and wet the wall, the row of end-block microdomains forms close to the wall to minimize stretching of the PS block in the 90° orientation.

The period for the 45° orientation was measured at 41.6-45.9 nm. On the other hand, the measured period for 90-degree is 38.6-42.1 nm in the direction perpendicular (y) to the wall and

42.5-44.1 nm in the direction parallel (x) to the wall. The uneven compression or expansion in x and y directions is observed in the packing of 90-degree orientation since PFS domains still distribute equally to the PI domains. This behavior is also seen in templated diblock copolymers.[30] However, this orthorhombic distortion is less seen in the case of 45 degree orientation because two neighboring PI(PFS) domains would be closer to PFS(PI) than the other two PI(PFS) domains when the chain is compressed or expanded in y direction which leads to an uneven stretch of the middle block PS. It has been theoretically demonstrated that the orientation of the minority A and C domains in an ABC triblock terpolymer can be controlled by tuning the wetting behavior of the wall and thickness of the film.[32] As shown in the schematic in Figure 6-5(c), there is high elastic free energy cost for the middle block polystyrene to arrange in the case of 90-degree orientation.

In addition to square arrays, the ISF_{82} was found to microphase separate to form cylinders oriented in plane for film thicknesses greater than approximately 35 nm, as discussed in section 6.5. Templating of in-plane cylinders is shown in Figure 6-6(a) for the blended triblock terpolymer packed in a PS-brushed template. The in-plane cylinders were aligned perpendicular to the wall but the cylinder ends do not contact the wall, due to the preference for the PS block to wet the brush layer. In contrast, for templates without the PS brush, cylinders align parallel to the wall to maximize the contact between the silica and the end-blocks, PI or PFS. Due to thickness variation in the unbrushed substrate, mixed parallel and perpendicular cylinders were also observed, as shown in Figure 6-6(b). This experimental result demonstrates that by tuning the relative affinity of the trench wall for each of the blocks, the in-plane orientation of the microdomains can be controlled in thicker films.

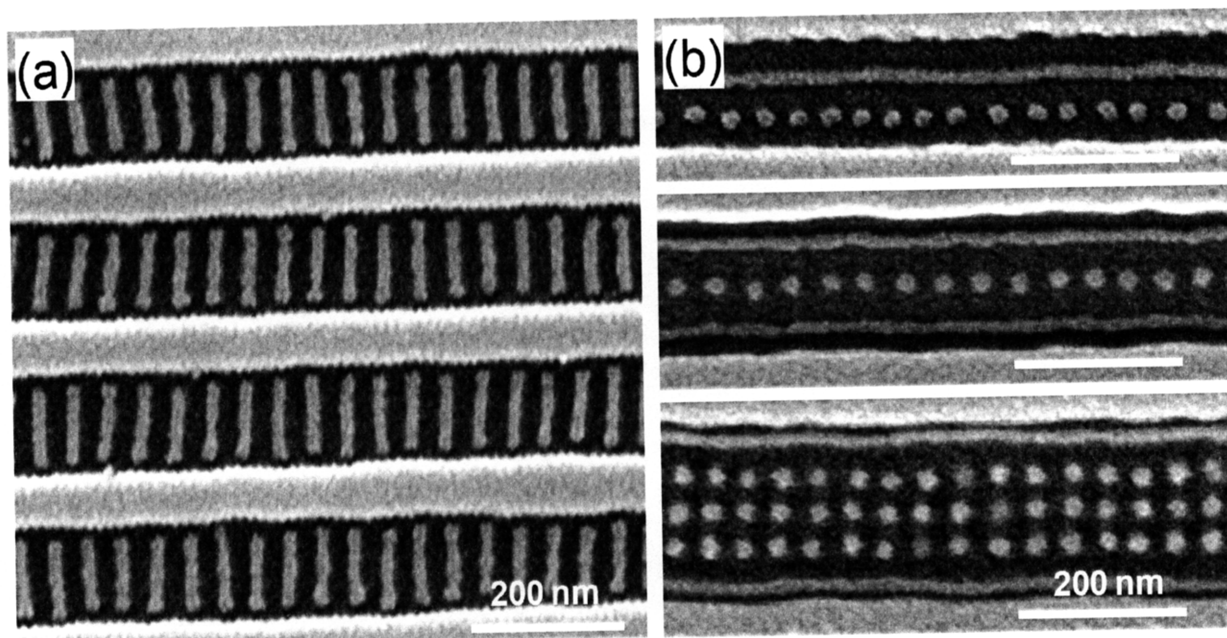

Figure 6-6 SEM images of relatively thick film of blended PI-*b*-PS-*b*-PFS triblock terpolymer assembled in (a) PS brushed template (b) unbrushed substrate after annealing and etching with oxygen RIE.

6.7 Pattern transfer

A good etch selectivity between the blocks is one of the essential requirement for block copolymer lithography, so that one or more of the blocks can be removed leaving the morphology of the remaining block(s) intact. As found earlier for PS-*b*-PFS-*b*-P2VP,[33] the organic blocks are removed easily using an oxygen reactive ion etch (RIE), leaving partly-oxidized organometallic PFS shells. The remaining PFS can be used as a lithographic mask for pattern transfer into functional materials, as already shown in PS-PFS diblock copolymers.[34] Figure 6-7 shows fabrication steps for pattern transfer of a square-pattern of vertical PFS cylindrical microdomains into a 30 nm thick silica layer. The PFS features were transferred into silica pillars by CF_4 RIE and the remaining PFS caps were removed by O_2 RIE.

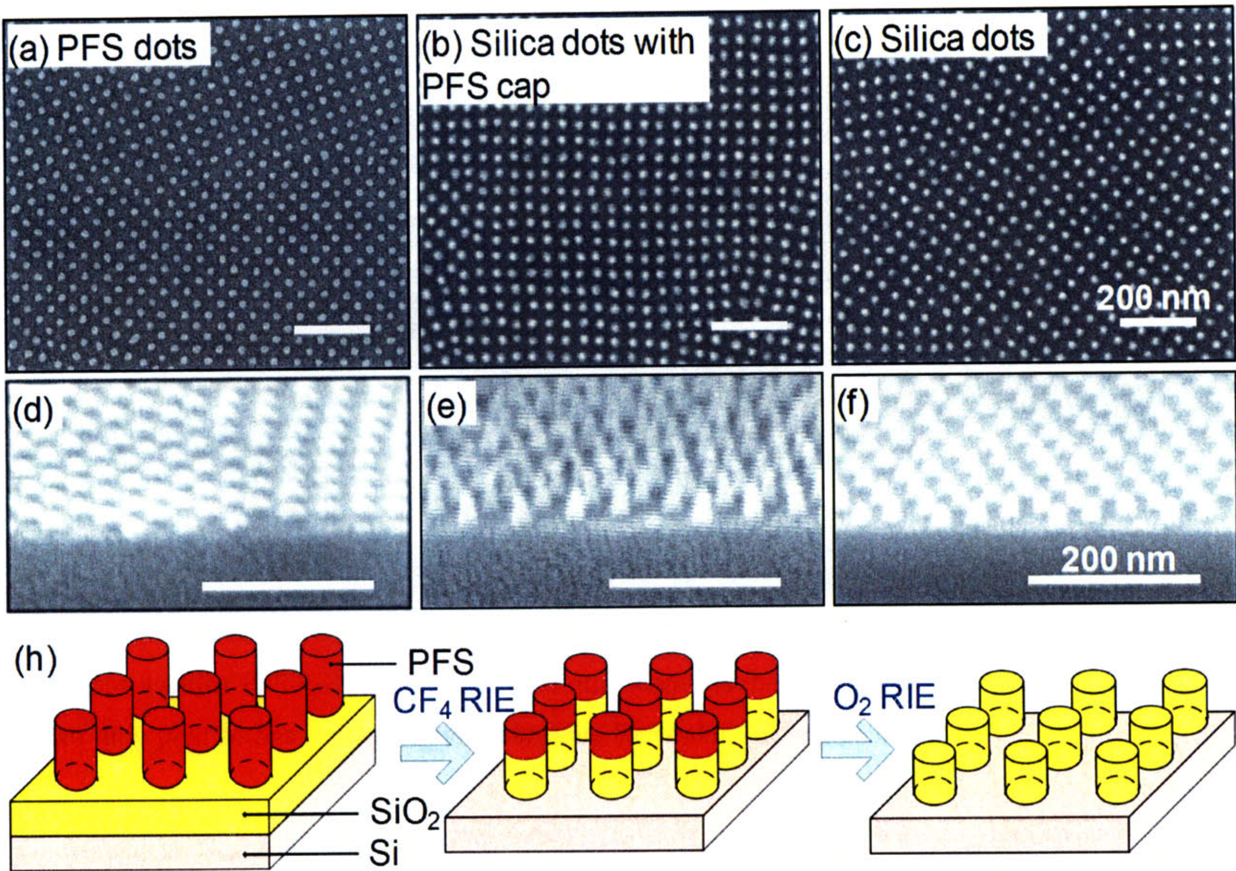

Figure 6-7 (a)-(f) SEM images of (a)-(c)top view and (d)-(f)side view of (a)(d) PFS dots after PI and PS removal;(b)(e) silica dots with PFS cap;(c)(f)silica dots. (h) Schematic of pattern transfer process.

6.8 Conclusion

A new class of PI-*b*-PS-*b*-PFS triblock terpolymers was developed that microphase separates to form an arrangement of interpenetrating square-symmetry cylinders of PI and PFS. A blend of the triblock terpolymer with PS homopolymer yielded thin films with square packed PFS microdomains, after removal of the PS and PI blocks. The square arrays could be templated within trenches, forming a square pattern that could be oriented at either 45° or 90° to the trench wall, depending on the chemical functionalization of the substrate. The square symmetry PFS arrays were transferred into 30 nm tall silica pillars by a series of RIE steps, making this a useful system for self-assembled nanolithography.

Reference

1. Park, M.; Harrison, C.; Chaikin, P. M.; Register, R. A.; Adamson, D. H. *Science* **1997,** 276, (5317), 1401-1404.
2. Park, C.; Yoon, J.; Thomas, E. L. *Polymer* **2003,** 44, (22), 6725-6760.
3. Segalman, R. A. *Materials Science and Engineering: R: Reports* **2005,** 48, (6), 191-226.
4. Darling, S. B. *Progress in Polymer Science* **2007,** 32, (10), 1152-1204.
5. Black, C. T.; Guarini, K. W.; Milkove, K. R.; Baker, S. M.; Russell, T. P.; Tuominen, M. T. *Applied Physics Letters* **2001,** 79, (3), 409-411.
6. Naito, K. H., H.; Sakurai, M.; Kamata, Y.; Asakawa, K. *IEEE Transactions Magnetics* **2002,** 38, (5), 1949-1951.
7. Black, C. T. *Applied Physics Letters* **2005,** 87, (16), 163116-3.
8. Deng, T.; Chen, C.; Honeker, C.; Thomas, E. L. *Polymer* **2003,** 44, (21), 6549-6553.
9. Garner, C. M.; Herr, D.; Krautschik, C. Directed Self-Assembly Requirements for Sub 20nm Lithography. www.itrs.net/Links/2007ITRS/LinkedFiles/ERM/DSAR11%20082107.DOC
10. Mogi, Y.; Kotsuji, H.; Kaneko, Y.; Mori, K.; Matsushita, Y.; Noda, I. *Macromolecules* **1992,** 25, (20), 5408-5411.
11. Mogi, Y.; Nomura, M.; Kotsuji, H.; Ohnishi, K.; Matsushita, Y.; Noda, I. *Macromolecules* **1994,** 27, (23), 6755-6760.
12. Chen, H.-L.; Lu, J.-S.; Yu, C.-H.; Yeh, C.-L.; Jeng, U. S.; Chen, W.-C. *Macromolecules* **2007,** 40, (9), 3271-3276.
13. Chen, B.; Baumeister, U.; Pelzl, G.; Das, M. K.; Zeng, X.; Ungar, G.; Tschierske, C. *Journal of American Chemical Society* **2005,** 127, (47), 16578-16591.
14. Evans, H. M.; Ahmad, A.; Ewert, K.; Pfohl, T.; Martin-Herranz, A.; Bruinsma, R. F.; Safinya, C. R. *Physical Review Letters* **2003,** 91, (7), 075501.
15. Park, S.-M.; Craig, G. S. W.; La, Y.-H.; Solak, H. H.; Nealey, P. F. *Macromolecules* **2007,** 40, (14), 5084-5094.
16. Tang, C.; Lennon, E. M.; Fredrickson, G. H.; Kramer, E. J.; Hawker, C. J. *Science* **2008,** 322, (5900), 429-432.
17. Tang, C.; Bang, J.; E. Stein, G.; Fredrickson, G. H.; Hawker, C. J.; Kramer, E. J.; Sprung, M.; Wang, J. *Macromolecules* **2008,** 41, (12), 4328-4339.
18. Rider, D. A.; Cavicchi, K. A.; Power-Billard, K. N.; Russell, T. P.; Manners, I. *Macromolecules* **2005,** 38, (16), 6931-6938.
19. Eloi, J. C.; Rider, D. A.; Wang, J. Y.; Russell, T. P.; Manners, I. *Macromolecules* **2008,** 41, (23), 9474-9479.
20. Mark, J. E., *Physical Properties of Polymers Handbook.* Second ed.; Springer: 2007.
21. Paquet, C.; Cyr, P. W.; Kumacheva, E.; Manners, I. *Chem. Mater.* **2004,** 16, (24), 5205-5211.
22. Ross, C. A.; Haratani, S.; Castao, F. J.; Hao, Y.; Hwang, M.; Shima, M.; Cheng, J. Y.; Vgeli, B.; Farhoud, M.; Walsh, M.; Smith, H. I. *Journal of Applied Physics* **2002,** 91, 6848.
23. Zheng, W.; Wang, Z.-G. *Macromolecules* **1995,** 28, (21), 7215-7223.
24. Kulbaba, K.; MacLachlan, M. J.; Evans, C. E. B.; Manners, I. *Macromolecular Chemistry and Physics* **2001,** 202, (9), 1768-1775.
25. Brandrup, J.; Immergut, E. H.; Grulke, E. A.; Abe, A.; Bloch, D. R., *Polymer Handbook (4th Edition).* Wiley-Interscience: New York, 1999; p VII/703-VII/707.

26. Tang, P.; Qiu, F.; Zhang, H.; Yang, Y. *Physical Review E* **2004,** 69, (3), 031803.
27. Matsen, M. W. *The Journal of Chemical Physics* **1998,** 108, (2), 785-796.
28. Matsen, M. W. *Physical Review Letters* **1995,** 74, (21), 4225.
29. Sugiyama, M.; Shefelbine, T. A.; Vigild, M. E.; Bates, F. S. *Journal of Physical Chemistry B* **2001,** 105, (50), 12448-12460.
30. Cheng, J. Y.; Mayes, A. M.; Ross, C. A. *Nature Materials* **2004,** 3, (11), 823-828.
31. Cheng, J. Y.; Ross, C. A.; Thomas, E. L.; Smith, H. I.; Vancso, G. J. *Advanced Materials* **2003,** 15, (19), 1599-1602.
32. Chen, H.-Y.; Fredrickson, G. H. *The Journal of Chemical Physics* **2002,** 116, (3), 1137-1146.
33. Chuang, V. P.; Ross, C. A.; Gwyther, J.; Manners, I. *Advanced Materials* **2009**, in press.
34. Cheng, J. Y.; Ross, C. A.; Chan, V. Z. H.; Thomas, E. L.; Lammertink, R. G. H.; Vancso, G. J. *Advanced Materials* **2001,** 13, (15), 1174-1178.

Chapter 7 Applications

7.1 Multilayer magnetic antidot arrays from block copolymer templates[1]

7.1.1 Introduction

Magnetic films with periodic arrays of holes (antidot arrays) are interesting materials for the study of magnetism in confined structures, and have been proposed for applications such as magnetic data storage.[2, 3] To date, magnetic antidot arrays have been fabricated using several methods including electron-beam lithography,[2, 4-6] optical lithography,[7, 8] self-assembled anodized alumina templates,[9-12] colloidal crystals,[13] and block copolymers.[14, 15] Much of this work has been carried out on antidot arrays with micron-scale periodicity. On these length scales, novel magnetic domain configurations and geometrically-induced magnetic anisotropies have been observed, and the effect of lattice symmetry has been also investigated.[16-18] Commonly, the coercivity is found to increase with decreasing hole period at fixed hole size[8, 19] or decreasing period when hole size/period is constant[4, 17] due to the pinning of the domain walls at the antidots.

Antidot arrays with sub-100 nm period have been made over large areas using anodized alumina templates,[10, 11, 20-27] and less commonly by using block copolymer lithography.[14, 15] Sub-100 nm antidot structures may also be made over small areas using electron-beam lithography.[28] In the case of anodic alumina templating, the magnetic material of interest is typically sputter-deposited over the alumina to form a porous network. A method using electrodeposition has also been demonstrated.[26] In the case of block copolymer lithography, a self-assembled and etched block copolymer film is used as a mask through which the magnetic film is ion-beam etched,[14, 15] although a liftoff technique may be possible, as demonstrated in Cr films.[29] Several groups have investigated the magnetic properties of sub-100 nm period antidot arrays. Barnard et al.[20-23]

studied Co, Fe, and $Co_{35}Fe_{65}$ antidot arrays made on anodized alumina with hole diameter 20 nm. The antidot array showed a thickness- and temperature-dependent coercivity that was considerably higher than that of the continuous film, and reversal was interpreted in terms of domain wall motion or nanoparticle-like reversal, depending on the film thickness. Tofail et al. [25] demonstrated a complex thickness-dependent coercivity in Fe antidot films, while Rahman et al. examined perpendicularly magnetized antidot arrays made of TbFeCo with coercivity over 4 kOe.[24] Heyderman et al.[28] showed that reversal propagated in chains along the rows of dots in square Co antidot arrays of period 200 nm. Liu et al.,[27] Xiao et al.[10] and Ma et al.[11] examined the thickness-dependent magnetoresistance and magnetic properties of Fe and NiFe, Ni, and Co-Al_2O_3 antidot arrays respectively.

In contrast, there has been little work on multilayered magnetic antidot arrays. Liu et al. described FeF_2 (20nm)/Fe (10nm) bilayer antidot arrays with 40 nm periodicity, which show exchange bias effects at low temperature.[14] Castaño et al. described NiFe/Cu/CoFe 'pseudo spin-valve' antidot arrays with 200 nm periodicity and long-range order;[9] the coercivity and magnetoresistance show in-plane symmetries corresponding to the symmetry of the ordered pores. Wang et al. fabricated multilayer Co 30nm/Cu/NiFe 30 nm antidot arrays with 400 nm period and investigated the effect of the Cu layer thickness on the transport properties.[30] In this study, we examine both single layer 3.5 nm Co antidot arrays and pseudo-spin-valve (PSV) Co 3.5nm /Cu 5nm /NiFe 3nm close-packed antidot arrays with periodicity of 26 nm and 40 nm and hole sizes of 12 nm and 17 nm. These periods and hole sizes are smaller than previously reported for multilayer antidot arrays, and allow trends in behavior to be followed as the hole sizes decrease below 20 nm. We will describe the role of the holes in the reversal process, and the changes in magnetic properties that can be expected by manipulating the hole sizes.

7.1.2 Experimental methods

Nanoporous substrates were made by Dr. Joy Cheng, Dr. Oun-Ho Park, and Dr. Ho-Cheol Kim at IBM Almaden Research Center and were prepared from a solution containing polystyrene-*b*-poly(ethylene oxide) (PS-*b*-PEO) block copolymer and organosilicates (OS), in which the OS is selectively miscible with the PEO.[31, 32] The PS-b-PEO+OS, which was spin-coated on top of a polydimethylglutarimide (PMGI) film, self-assembled into a close-packed array of PS domains within the PEO+OS matrix. As shown in Fig. 7-1, the PS domains extend from the top surface of the film through to the PMGI layer.[33]

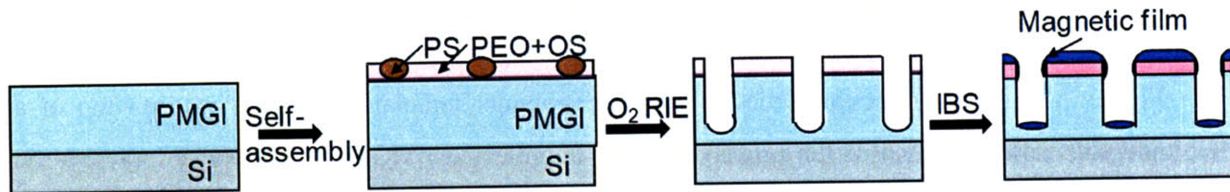

Figure 7-1 Schematic of the fabrication process for the antidot magnetic film.

An oxygen reactive ion etch removed the PS and the underlying PMGI to create channels perpendicular to the substrate with period 26 nm or 40 nm and diameters 12 nm or 17 nm respectively. These length scales correspond to two different PS-*b*-PEO copolymers with molecular weights of $PS_{9.5k}$-*b*-$PEO_{9.5k}$ and PS_{19k}-*b*-$PEO_{12.3k}$.[33] The antidot arrays were fabricated over large area (> 1 sq. cm) substrates by ion-beam sputtering (IBS) of Co 3.5 nm films and Co 3.5nm /Cu 5nm /NiFe 3nm multilayers on the etched block copolymer films (Fig. 7-2(a)-(c)), while continuous films were made on thermally oxidized (100) Si wafers for comparison. The base pressure was below 5×10^{-9} Torr and the argon pressure during IBS deposition was 2×10^{-5} Torr. This low deposition pressure ensures a non-conformal coverage, such that there is

relatively little sidewall deposition and the pores in the film remain open as seen in Fig. 7-2(b) and (c). The material deposited at the bases of the pores is electrically isolated from the antidot film, and likely to be superparamagnetic. A capping layer of 2 nm Cu was deposited on all the samples to minimize oxidation.

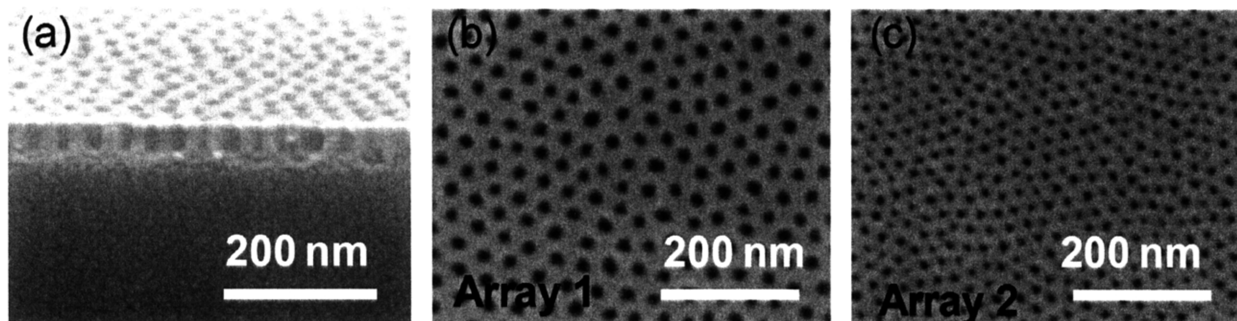

Figure 7-2 (a) Cross-sectional view of block copolymer templated organosilicate on top of a PMGI underlayer after removal of the polystyrene and unprotected PMGI with an oxygen reactive ion etch. (b) Scanning electron micrograph of antidot array 1. (c) Scanning electron micrograph of antidot array 2.

The magnetic hysteresis loops of antidot arrays and continuous films were measured at room temperature using an alternating gradient magnetometer (AGM) with a gradient field of 0.1 Oe, and magnetotransport properties were obtained using the four-point probe technique with an external in-plane magnetic field. The magnetoresistance is defined as the difference between the maximum resistance and the resistance at saturation. Minor loop measurements, starting from a field of 200 Oe for the antidot arrays or 100 Oe for the continuous film, were performed by AGM. A micromagnetic simulation was performed using the 3D NIST OOMMF code for 450 nm x 560 nm films containing holes. Co (4 nm) and Co (4 nm) /Cu (4 nm) /NiFe (4 nm) films were modeled. The shapes, sizes and locations of holes were input from SEM images of the two samples. Two patterns were used: 40 nm period with 17 nm diameter holes (referred to as array 1)

and 26 nm period with 12 nm diameter holes (array 2). The structures were discretized into 4 nm x 4 nm x 4 nm cubic elements and hysteresis loops were calculated starting from 5000 Oe saturation, using the standard parameters for bulk Co and NiFe with random magnetocrystalline anisotropy directions assigned to each cell.

7.1.3 Magnetic properties of single-layer Co antidot arrays

We describe first the single-layer Co films. Experimentally, all the films showed an in-plane anisotropy due to a magnetic field of order 20 Oe present during film deposition. Along the in-plane easy axis, the continuous film of 3.5 nm Co had a coercivity of 16.7 Oe, compared to 28.3 Oe for a film with 17 nm hole diameter (array 1) and 25.4 Oe for a film with 12 nm holes (array 2). The holes therefore raise the coercivity. Much higher coercivity values, up to ~600 Oe, have been reported for Co antidot arrays 15 – 20 nm thick with ~20 nm hole diameters,[20-23] but the coercivity decreased rapidly with decreasing film thickness; our data are consistent with this trend. Fig 7-3 shows calculated micromagnetic domain states for each array at two different fields, and the half-hysteresis loops. The model predicts a higher coercivity for array 1 (538 Oe) compared with array 2 (263 Oe), as shown in fig. 7-3(b), but the magnitude of the coercivity is much higher than that found experimentally. This suggests that reversal may be initiated by features not captured in the model, for example by edge features in the holes or at oxidized regions of lower anisotropy, or at features that act as reverse domain nucleation sites located outside the small area of film that was modeled. The model suggests that reversal in array 1

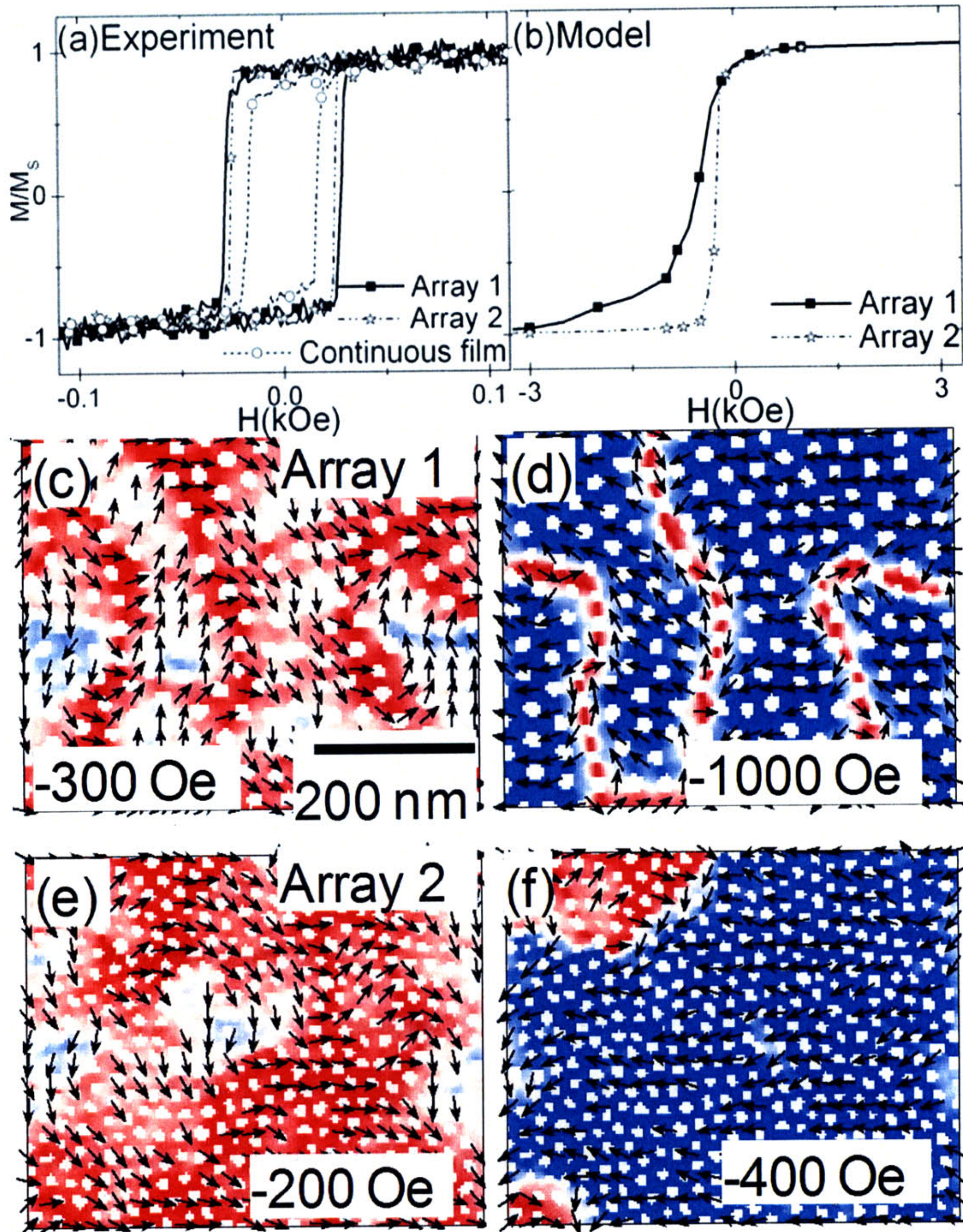

Figure 7-3 (a) Measured hysteresis loops of single-layer Co antidot arrays. (b) Half hysteresis loops of single-layer Co arrays based on micromagnetic modeling. [(c)–(f)] Magnetic configuration calculated for single-layer Co antidot arrays: (c) array 1 at −300 Oe reverse field, (d) array 1 at −1000 Oe, (e) array 2 at −200 Oe, and (f) array 2 at −400 Oe. The reverse field was applied from right to left. The red (lighter shade) color indicates the original left-to-right magnetization direction and blue (darker shade) indicates the reversed regions. Arrows show the magnetization directions of some of the cells.

occurs by the rotation of areas of the film larger than the antidot period. When adjacent regions rotate in opposite directions, 360° walls form along rows of antidots, and the walls are eliminated only at large fields, giving a slow approach to saturation. In array 2, the smaller antidots appear less effective at pinning domain walls. The domain walls are more easily annihilated to give a rapid saturation at 500 Oe applied field.

7.1.4 Magnetic behavior of multilayer antidot arrays

We now consider the multilayer film. In the continuous film, Fig. 7-4(a), two distinct steps can be seen in the easy-axis major hysteresis loop corresponding to the reversals of the NiFe layer at ~2 Oe and the Co at 17 Oe. The two multilayer antidot arrays also show two steps in their major loops, but notably the NiFe reversal occurs at positive fields so that the two layers are magnetized antiparallel at remanence (Fig. 7-4(b) and (c)). This antiparallel remanent state has also been observed in multilayer dot arrays[34] and bar arrays[35] and is attributed to the magnetostatic interaction between the layers.

Comparing arrays 1 and 2, as the hole size and spacing is decreased the Co layer switching field is reduced as seen in the single layer films, but unlike the behavior seen in multilayer antidot films with micron-sized holes.[4, 6, 8, 17, 19] Coercivity values are given in Table 7-1 for the three samples.

Figure 7-4 also shows minor loops for the continuous film and the two arrays, from which the coercivities of the NiFe layers and the interaction fields between the NiFe and Co may be calculated. The shapes of the major and minor loops can be understood by considering the four possible magnetic configurations A, B, C and D of the layers, which are shown schematically in Fig. 7-4(d), where positive saturation corresponds to state A. For the continuous

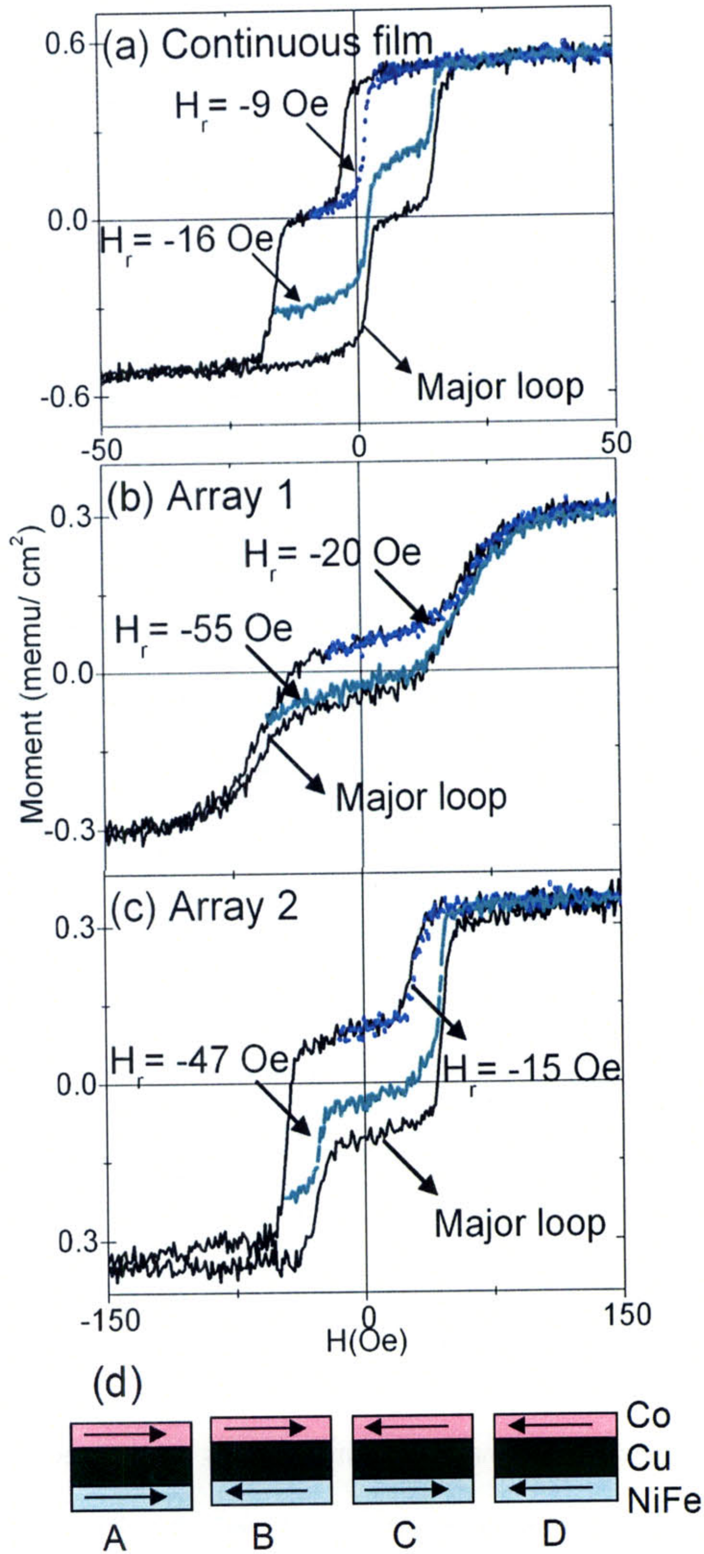

Figure 7-4 Major and minor hysteresis loops of the Co(3 nm)/Cu(5 nm)/NiFe(3.5 nm) multilayers measured for (a) continuous film, (b) array 1, and (c) array 2. (d) A schematic representation of the four possible magnetic configurations for the Co and NiFe layers.

Switching field	Continuous film, Oe	Array 1, Oe (40 nm period)	Array 2, Oe (24 nm period)
Multilayer: H_{int}	0.6	-66	-29
H_C of NiFe	2	2.5	2.5
H_C of Co	16.2	63	46.8
Single layer: H_C of Co	16.7	28.3	25.4

Table 7-1 The switching fields and interaction field of the NiFe and Co layers in the antidot arrays and in the continuous films.

film, as the field is reduced to a reverse value H_r= -9 Oe then increased back to positive saturation, the configuration has changed from state A to B and then back to state A as the NiFe layer reverses. The NiFe minor loop shows a coercivity of 2 Oe, and a negligible interaction field (measured from the field offset of the NiFe minor loop) of approximately 0.6 Oe, showing that the layers are almost entirely decoupled. A minor loop measured down to H_r= -16 Oe shows complete reversal of the NiFe and of 60% of the Co film area (state D), while the remaining 40% of the film area is in state B. The return branch of the minor loop shows the superposed D -> C and B->A transitions near zero field, followed by the C->A transition at 17 Oe.

The minor loops of the antidot arrays can be interpreted similarly, and resemble those measured for Co/Cu/NiFe bar-shaped elements.[35] The A->B transitions occur at positive fields so B is the remanent state. As an example, for array 2, as shown in fig. 7-4(c), 60% of the film area had switched from state A to D and 40% of the film area to state B at H_r = -47 Oe. When the

field is increased back to positive saturation, three steps are seen, corresponding to D->C at -30 Oe, B ->A occuring gradually around 30 Oe, and C ->A at 47 Oe. The NiFe layer coercivities are all small (2 – 3 Oe), while the interaction fields are significant, and higher for array 1. The Co layer switching field exceeds that of the single layer film, which may be partly due to the effect of the interaction field from the NiFe, which opposes the Co layer reversal.

The magnetoresistance of the samples is shown in Fig. 7-5. These films show giant magnetoresistance (GMR), although the magnitude of the GMR is modest due to the current-shunting effects of the copper capping layer and the relatively thick copper spacer. The high resistance plateaux correspond to the existence of states B or C in the hysteresis loop, while the low resistance state corresponds to states A or D. The GMR is 0.24% for the continuous film and 0.26% and 0.21% for arrays 1 and 2 respectively. The switching fields shown from the GMR data in Fig. 7-5 and the hysteresis data of Fig. 7-4 differ slightly because the measurements were made at different times. The GMR data was measured soon after sample deposition, while the hysteresis was measured 20 days after film deposition. Atmospheric oxidation of the samples leads to a gradual increase in the coercivity of the films.

Fig. 7-6 shows results of micromagnetic modeling of the two multilayer arrays. The magnetic configurations of the Co and NiFe layers are shown at different field values. The model shows the NiFe layer reversal at positive fields as a result of the magnetostatic field of the Co layer, for both arrays, in agreement with the measurements. In array 1, a residual 360° wall in the NiFe influences the reversal of the Co, and leads to a 360° wall of opposite sense in the Co layer located adjacent to the wall in the NiFe. In comparison, the NiFe layer in array 2 was fully reversed before the Co layer started to reverse, and subsequently no paired walls were observed

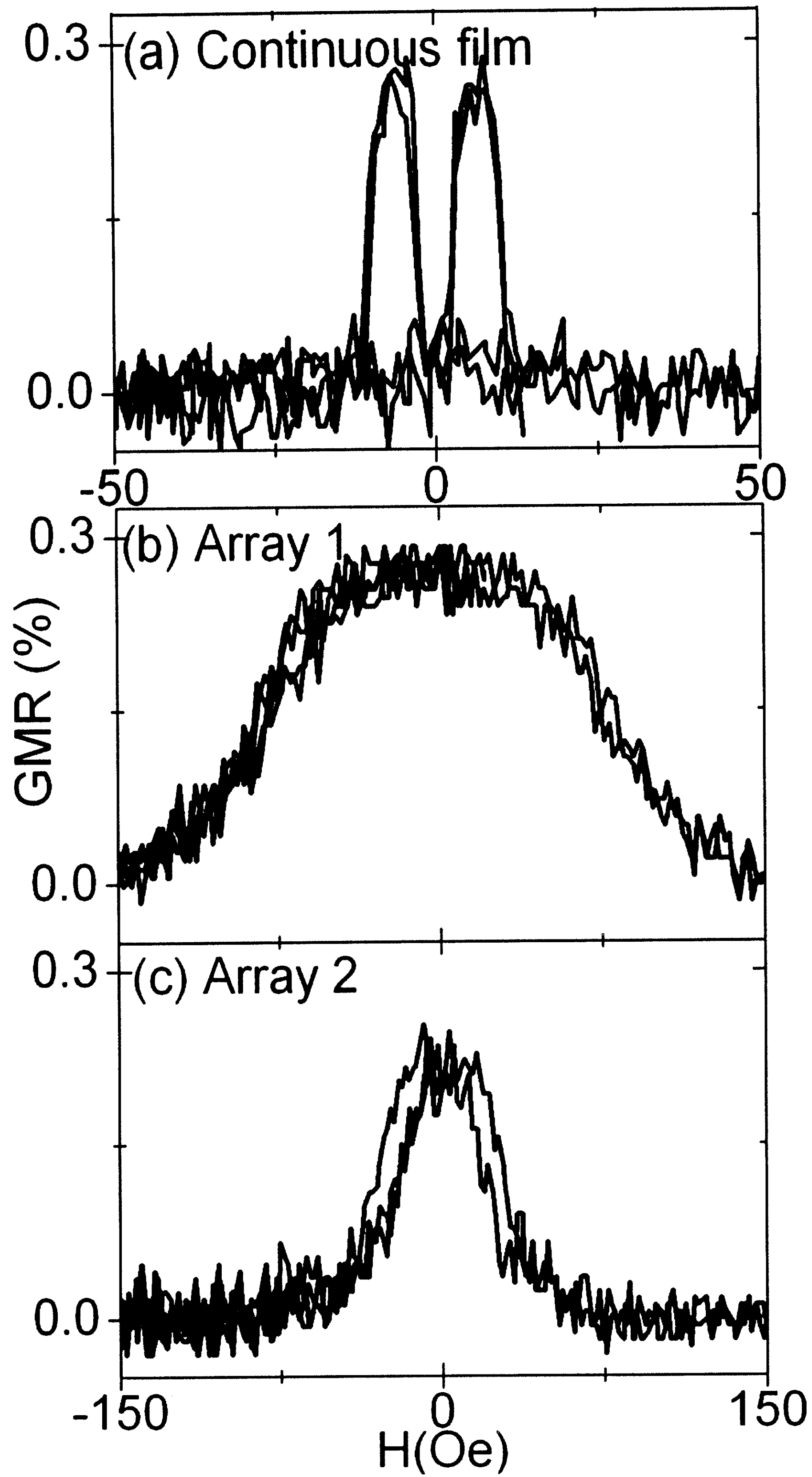

Figure 7-5 Magnetoresistance data for (a) Continuous film; (b) Array 1; (c) Array 2.

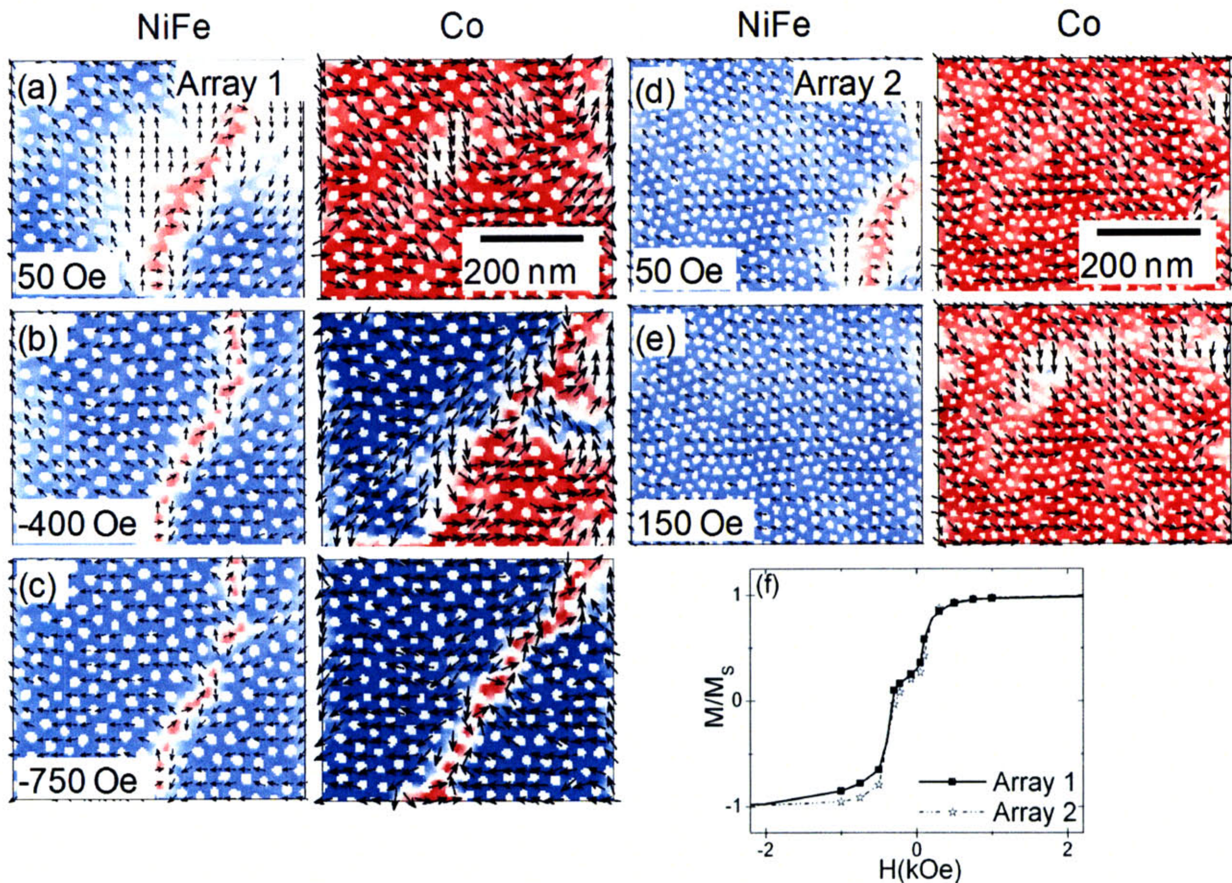

Figure 7-6 (a-e) Snapshots of domain structures and (f) half hysteresis loop of the Co(4 nm)/Cu(4 nm)/NiFe(4 nm) multilayers based on results of simulations at a field of (a) 50 Oe (b) –400 Oe and (c) –750 Oe for array 1, and (d) 50 Oe and (e) –150 Oe for array 2, after positive saturation. The Co and NiFe layers have been separated for clarity. The reverse field was applied from right to left. Color scheme as in Fig. 2.

in the two layers in the model. As in the single-layer modeling, the switching fields are much higher than those measured experimentally.

Both the single-layer films and the multilayers show an increase in switching field with increasing hole spacing and diameter. This effect is modest for the single-layer Co film, and larger for the Co within the multilayer, which may indicate the influence of the magnetostatic interactions on the reversal. The trend of increasing coercivity with hole size can be interpreted

in terms of the pinning effects of well-defined defects,[36-39] i.e. regions within which the magnetic parameters change abruptly compared to the bulk of the material. The films are sufficiently thin that the domain walls are Néel type,[36, 40] with magnetization in plane (as found in the micromagnetic modeling described above).

An estimate of domain wall width (δ) in a thin film may be calculated from the relation[36]

$$\delta^2[K/2+(2\mu_0M^2/\pi)\tan^{-1}(t/\delta)]-(2\mu_0M^2/\pi)[t\delta/(1+t/\delta)]-A\pi^2=0,$$

where A is the exchange constant, of order 10^{-6} erg/cm, K is the (uniaxial) magnetocrystalline anisotropy, μ_0 is the permeability of free space, M is the saturation magnetization and t is the thickness of the film. Bulk values of $K_u = 4.1 \times 10^6$ erg/cm^3 and M= 1440 emu/cm^3 for uniaxial hcp Co and $K_1 = -3 \times 10^3$ erg/cm^3 and M= 800 emu/cm^3 for cubic NiFe lead to estimated wall widths of 21 nm and 680 nm in 3 nm Co and 3.5 nm thick NiFe films respectively. However, the films are polycrystalline, with grain sizes of the order of the film thickness and therefore much smaller than the domain wall width, so the net anisotropy of the material within the walls will be smaller than the bulk values, and the walls correspondingly wider. For example in evaporated hcp Co, measured wall widths extrapolate to ~400 nm at zero film thickness.[41] Therefore for both magnetic layers in the multilayers studied here, the wall widths δ are considerably larger than the antidot diameters *D*. In the regime of $D/\delta \ll 1$, the coercivity is expected to increase linearly with *D* because larger defects occupy more of the domain wall volume and therefore pin it more effectively.[35] The trend may be partly countered by the smaller density of antidots in the larger period array. The expected increase in coercivity with antidot size is consistent with the higher coercivities seen in array 1, but differs from observations on films with micron-sized antidots, where coercivity decreases with increasing

period or antidot size.[4, 8, 17, 19] Modeling suggests that for well-defined defects in the regime of $D/\delta > 1$, the coercivity would be independent of defect size,[36 37] but in most reports of experimental work the number of antidots decreases as their size increases, giving fewer pinning sites and easier reversal. We may expect a maximum coercivity for $D/\delta \sim 1$, as observed by Dijkstra et al.[38] and O'Handley et al.[39] in bulk magnetic alloys.

7.1.5 Conclusions

The magnetic reversal and magnetotransport behavior of multilayer Co/Cu/NiFe antidot arrays with hole diameters below 20 nm has been described, and compared with the behavior of single layer Co films. The holes are smaller than the domain wall widths, and therefore an increase in switching field with antidot dimensions is observed. This differs qualitatively from the behavior of antidot films with larger holes reported elsewhere, in which coercivity is found to decrease with increasing dimensions. In the multilayer antidot arrays, the reversal of the NiFe is dominated by magnetostatic interactions between the Co and NiFe leading to an antiparallel remanent state. This behavior was reproduced in micromagnetic simulations. In addition, depending on the hole geometry, coupled 360° walls are predicted to form in the multilayer which are stable up to high fields. The modeling suggests these are more prevalent in the larger period antidot array, in which the holes are more effective pinning sites, and the interlayer interactions are stronger. The interplay between the domain wall pinning by the antidots and the magnetostatic coupling between the magnetic layers enables the switching properties of the film to be tailored for magnetic or magnetoelectronic device applications.

7.2 Densely-packed arrays of ultrahigh-aspect-ratio silicon nanowire fabricated using block copolymer lithography and metal-assisted etching

7.2.1 Introduction

Semiconductor nanowires have attracted considerable attention due to potential applications arising from their quasi-one-dimensional nature,[42] including their high surface to volume ratio. In particular, silicon nanowires (SiNWs) are candidates for applications in nanoscale optoelectronics, sensors, and other devices.[43-45] Much effort has been devoted to the fabrication of vertically-aligned epitaxial Si nanowires with highly controlled diameter, length, and placement.

The most commonly used method for the fabrication of SiNWs is the vapor-liquid-solid (VLS) technique in which metal nanoparticles are used as catalysts for growth by chemical vapor deposition.[46, 47] Catalysts for NW growth include gold nanodot arrays patterned by nanosphere lithography,[48] and gold colloidal particles.[49] One major concern for VLS-grown wires is the diffusion of catalyst metal, typically gold, into the wires at the high temperatures usually required for wire growth. This poses a serious problem for the realization of SiNW electronic and optical devices because gold contamination in silicon creates carrier traps and reduces minority carrier lifetimes. Another challenge for VLS SiNW growth is orientation control. In particular, VLS SiNWs preferentially grow in the <111> direction but the orientation varies with wire dimension.[50] Vertical epitaxial growth on Si(100) wafers is therefore rarely observed and mixed growth in the four crystallographically equivalent <111> directions is observed instead. This limits integration of VLS nanowires with current CMOS technology.

Other methods for nanowire creation through etching processes have also been investigated. Examples include the fabrication of high aspect ratio silicon nanopillars using deep reactive ion etching (DRIE) using a polystyrene colloidal mask[51] and the fabrication of densely packed silicon nanopillar arrays using a Cr mask made by block copolymer lithography.[52] Oxidation-etch cycles have also been used to create lithographically defined Si nanowires with both in-plane and vertical orientations.[53, 54] Although these techniques are effective, the spacings of nanowires created through oxidation-etch processes are limited to those of the pre-oxidation Si structures, and fabrication of high-aspect ratio 1-D silicon nanostructures using DRIE is limited by mask degradation.

Metal-assisted etching in combination with various film patterning techniques has recently been demonstrated as a promising alternative for SiNW fabrication. Metal-assisted etching has the advantage of being a room temperature process, and can produce features oriented in the <100> direction.[55] In this approach, metal particles or films are used to locally catalyze Si etching in a mixture of hydrofluoric acid (HF) and an oxidant. Although the exact dissolution chemistry of silicon in HF is not well understood, it is generally accepted that the silicon surface is passivated against dissolution unless a hole carrier is available.[56] According to the local reduction-oxidation reaction scheme proposed by Li et al.,[57] hole injection is provided by the reaction of the oxidant solution at the catalyst metal. Since injected holes diffuse rapidly away from the catalyst, etching is confined to areas near the metal. This localized behavior makes metal-assisted etching a simple and effective method for preparing arrays of high-aspect ratio silicon nanostructures.

Several SiNW fabrication methods employing metal-assisted etching have been recently reported. For example, large-area silicon nanowire and nanoribbon arrays were obtained by etching Si in HF and $Fe(NO_3)_3$, using a catalyst consisting of interconnected networks of silver nanoparticles deposited by galvanic displacement from a solution of HF and $AgNO_3$.[58] SiNW size uniformity is limited by the distribution of Ag catalyst sizes, and wire diameters ranged from 20 to 300nm.[59] Nanosphere lithography based on polystyrene or silica colloidal spheres was used[55] to create antidot arrays in a silver film deposited on Si, from which close-packed SiNW arrays were made. The minimum SiNW diameter is limited by the colloid size, and full areal coverage of colloidal particles over large areas was difficult to achieve. Recently, Huang et al. used a method based on an anodic aluminum oxide mask to pattern SiNW arrays with diameter as small as 9 nm.[60] However, the resulting nanowires had aspect ratios only up to 10, and broadly distributed diameters.

Here we describe a new technique that employs a catalyst film patterned using block copolymer (BCP) lithography to fabricate ~20nm diameter SiNWs with high monodispersity over large areas. Block copolymers microphase separate to form self-organized patterns with lamellar, cylindrical or spherical morphologies and a characteristic length scale that depends on the volume ratio and chain length.[61] Block copolymer lithography has been used to pattern catalysts for the fabrication of vertical arrays of carbon nanotubes[62] and metal nanowires.[63] The self-organized patterns generally have local close-packed order, but when phase separation is templated with lithographically defined features, they can also have long-range close-packed order.[64, 65] Although the block copolymer we used showed less uniform ordering, improved long range order can be attained through graphopitaxy of other copolymers. We chose a polystyrene (PS)-*block*- polyferrocenyldimethylsilane (PFS) block copolymer that forms spherical PFS

microdomains surrounded by a PS matrix on annealing.[66, 67] The organometallic PFS block has a high etch resistance, allowing for good pattern transfer into an underlying film. Using topographical templating, we demonstrate patterning of SiNWs at lithographically defined locations over cm-sized substrates.

7.2.2 Experiment Method

All the etching procedures were carried out under ambient conditions at room temperatures. Si(100) wafers (p-type, Boron-doped, resistivity = 1-25Ωcm) were purchased from Silicon Valley Microelectronics Inc. HF and H_2O_2 were purchased from BDH Laboratory Supplies. Ethyl alcohol (200 proof), used as an intermediate fluid for critical point drying, was acquired from AAPER Alcohol and Chemical. Silicon substrates were used without further cleaning. All chemicals listed above were used without further purification.

7.2.2.1 Anti-reflection coating trench preparation

First the silicon substrate was coated with e-beam evaporated silicon oxide (60 nm), BARLi anti-reflection coating (50 nm, AZ Electronic Materials), sputter-deposited silicon oxide (7 nm), PFI-88 photoresist, (200 nm, Sumitomo Chemical Co.), sputter-deposited silicon oxide (7 nm), and BARLi ARC (200 nm). The top three layers (photoresist-oxide-ARC) comprised a trilayer stack for interference lithography, and the bottom three layers were for pattern transfer. The resist stack was then exposed using a Lloyd's mirror interference lithography system equipped with a 325 nm wavelength helium-cadmium laser. The period and duty cycle of the gratings was controlled by the incident angle and exposure time, respectively. After a series of RIE steps (He-O_2 plasma for ARC, and CF_4 plasma for silicon oxide), the resulting grating

pattern was transferred into the bottom ARC layer which was used as the template for BCP self-assembly.

7.2.2.2 Critical point drying

Critical point drying was done by Ms. Shih-Wei Chang in Professor Carl Thompson's group at MIT and was carried out in a Tousimmis AutoSamDri 815 Critical Point Drier. Prior to drying, the samples were rinsed consecutively in 50%, 75%, and 90% alcohol for 3 min each, followed by 3 rinses in 100% ethanol for 3 min each before critical point drying for 1 h.

7.2.2.3 Silicon Nanowire Fabrication: Carpets and Carpeted Channels

The experimental procedure for the fabrication of a continuous carpet of vertically-aligned silicon nanowires is illustrated schematically in Figure 7-7, and resulting structures are shown in Figure 7-8. Au deposition was done by Mr. Jim Daley. Part of dry etching, lift-off and metal-assistant etching and were done by Ms. Shih-Wei Chang. TEM images were taken by Mr. Steven T. Boles in Professor Carl Thompson's group at MIT. First, 60nm of SiO_2 was deposited by electron beam (e-beam) evaporation on a (100)-oriented silicon substrate. A diblock copolymer, PS-*b*-PFS was then spin-coated from a 1 to 1.5 wt% toluene solution onto the SiO_2 layer. Two diblock copolymers with differing molecular weights were used: 47kg/mol for PS and 15kg/mol for PFS (denoted as PS-*b*-PFS 47/15), and 42kg/mol for PS and 12kg/mol for PFS (denoted as PS-*b*-PFS 43/12). The film thicknesses were 51-55 nm for PS-*b*-PFS 47/15, and 42-45 nm for PS-*b*-PFS 43/12. To achieve microphase separation into arrays of PFS spheres, the spin-coated samples were vacuum-annealed at 140°C for 44 hours. The PS matrix was removed using oxygen plasma (6 mTorr, 90 W, 52 s). Subsequently, the PFS pattern was transferred into

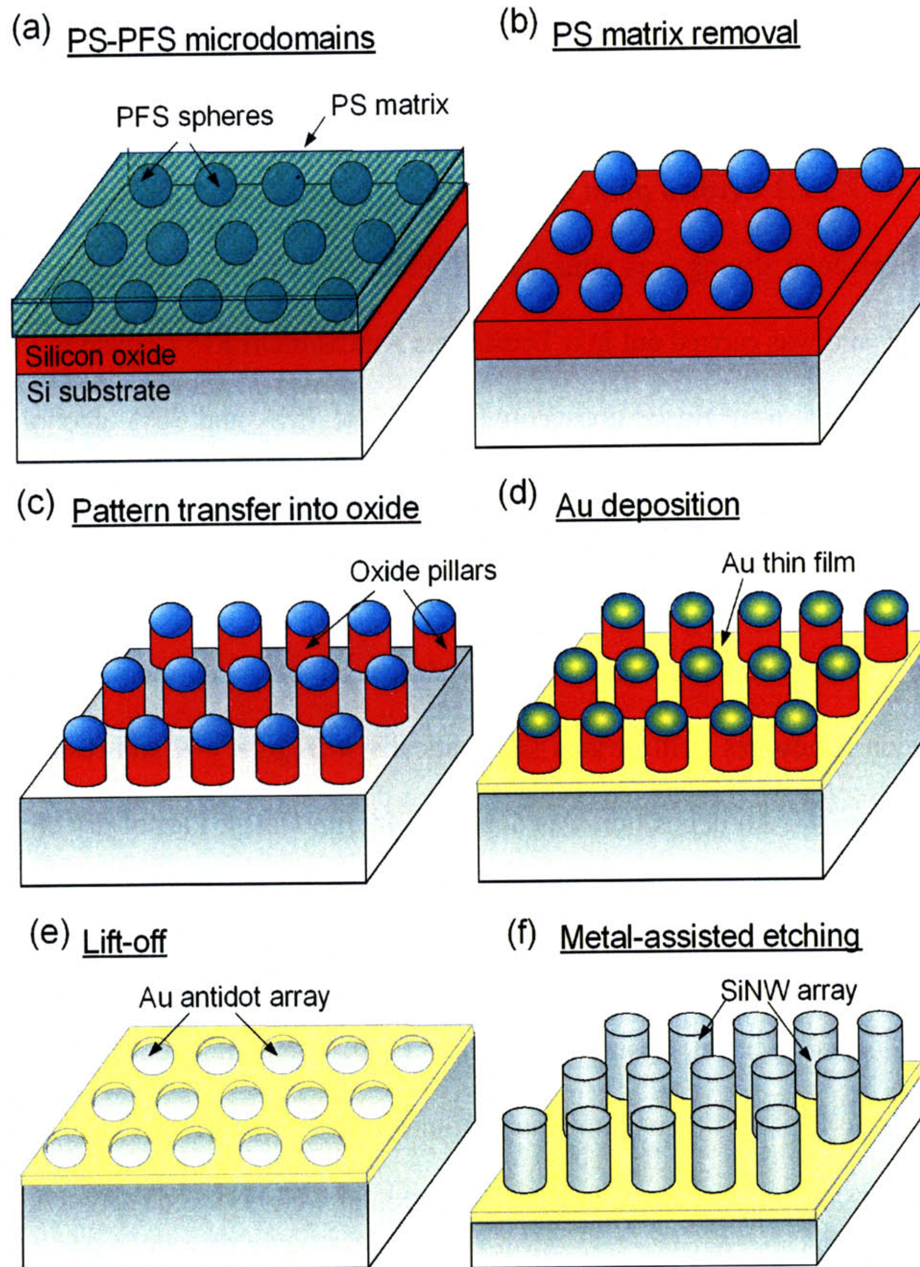

Figure 7-7 Schematic of the SiNW fabrication process: (a) Phase-separated polystyrene (PS)-*block*- polyferrocenyldimethylsilane (PFS) domains after spinning a block copolymer film onto a silicon substrate coated with silicon oxide and vacuum annealing; (b) Partly oxidized PFS spherical domains after the PS matrix is removed using oxygen reactive ion etching; (c) Pattern transferred into the oxide layer to form silicon oxide pillar arrays; (d) Au deposition over the oxide pillars; (e) Au antidot array after HF lift-off; (f) Silicon nanowire array after etching in a solution of hydrofluoric acid and hydrogen peroxide.

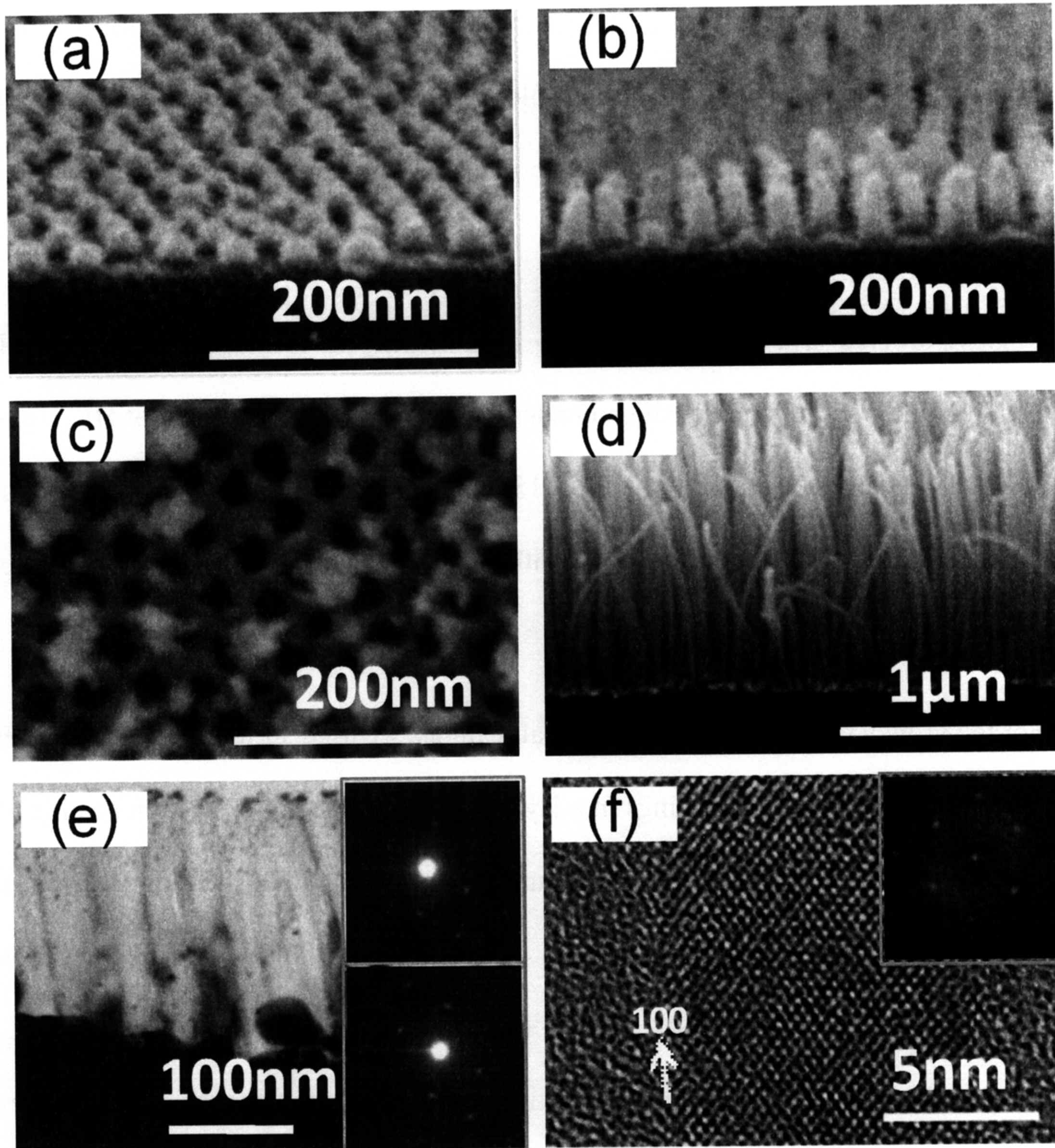

Figure 7-8 Scanning electron microscope images showing steps in the SiNW fabrication process flow: (a) PS-*b*-PFS 47/15 on a silicon substrate coated with silicon oxide after PS matrix has been removed by oxygen RIE; (b) Oxide pillars after CF_4 RIE; (c) 12 nm thick Au anti-dot array after liftoff of the pillars. Some silica material remains (bright contrast); (d) Silicon nanowire array after metal-assisted etching; (e) TEM image of a wire array (made from PS-*b*-PFS 43/12). Inset shows the selected-area diffraction (SAD) pattern on the [011] zone axis of different regions. The upper inset corresponds to a region encompassing mostly the substrate, and the lower inset corresponds to a region encompassing mostly the wire array; (f) TEM image of a single wire. Inset is the fast Fourier transform (FFT) pattern corresponding to a region in the nanowire showing the [011] zone axis.

the oxide layer by reactive ion etching (RIE) in CF_4 (10 mTorr, 150 W, 65 s) to form SiO_2 nanopillar arrays on the substrate. 12 nm of gold was deposited by electron-beam evaporation onto the oxide pillar arrays, and the pillars were removed by immersion in dilute HF for a short time, leaving an Au antidot array.

Finally, ordered arrays of SiNWs with good fidelity to the original block copolymer pattern were obtained by etching the silicon under the gold in a mixed solution of HF, H_2O_2, and water (10 wt. % HF and 1.5 wt. % H_2O_2) for 5-15 minutes in ambient light. Post-etching drying was done in a critical point drier after rinsing with an intermediate fluid (alcohol or isopropanol) several times.

For the growth of SiNWs in topographical features, we used a Lloyd's mirror interference lithography system[68] to fabricate gratings in a layer of a polymeric anti-reflection coating (ARC) which served to order the PFS sphere array (Figure 7-9(a)). PS-*b*-PFS 47/15 was spin-coated into the ARC gratings and annealed under vacuum at 140°C for 44 hours. During annealing, the polymer flows from the grating mesas into the trenches, leaving the mesas polymer-free. The spherical PFS microdomain pattern and the grating pattern were transferred into the oxide layer by RIE to form arrays of oxide pillars inside oxide gratings. Lift-off of a 10 nm Au film was performed in HF to obtain narrow stripes of Au containing ordered arrays of nano-sized holes. Finally, SiNW arrays inside Si trenches were achieved by immersing the samples in a mixture of 10 wt. % HF and 1.5 wt. % H_2O_2. A resulting wire-in-trench structure is shown in Figure 7-10. The curved bottom, as shown in Figure 7-10(f), may be the result of poor mixing of the etchant solution at the bottom of the trenches.

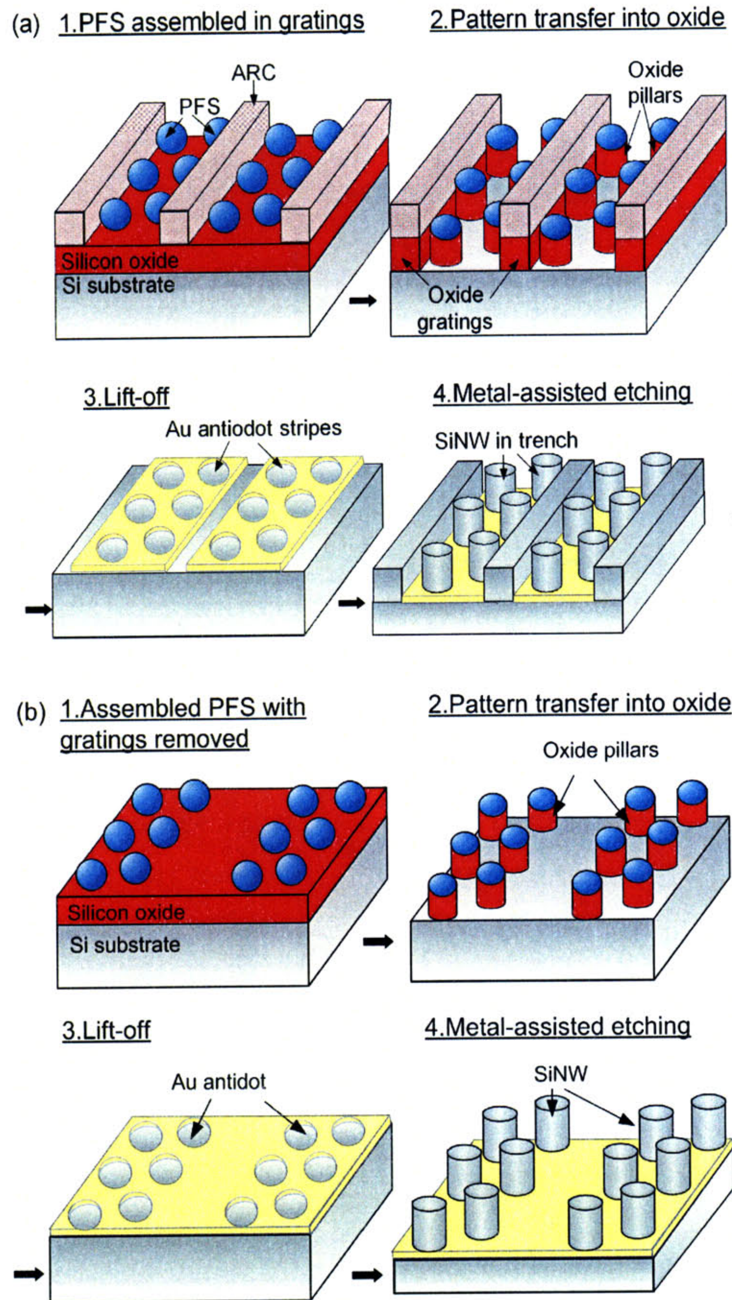

Figure 7-9 Schematic of the process flow for templated wire fabrication: Fabrication of SiNW-in-trench structure: PFS spherical domains after annealing and removal of the PS matrix; Oxide grating and oxide pillars after RIE using the PFS spheres and ARC grating as etch masks; Au thin film stripes with nanohole arrays after lift-off in HF; SiNW arrays inside trenches after metal-assisted etching; (b) Fabrication of ordered SiNW array using a removable ARC grating: Removal of ARC grating; oxide pillar arrays after RIE using the PFS spheres as etch masks; Continuous Au thin film with stripes of nanohole arrays; SiNW clusters on a flat substrate.

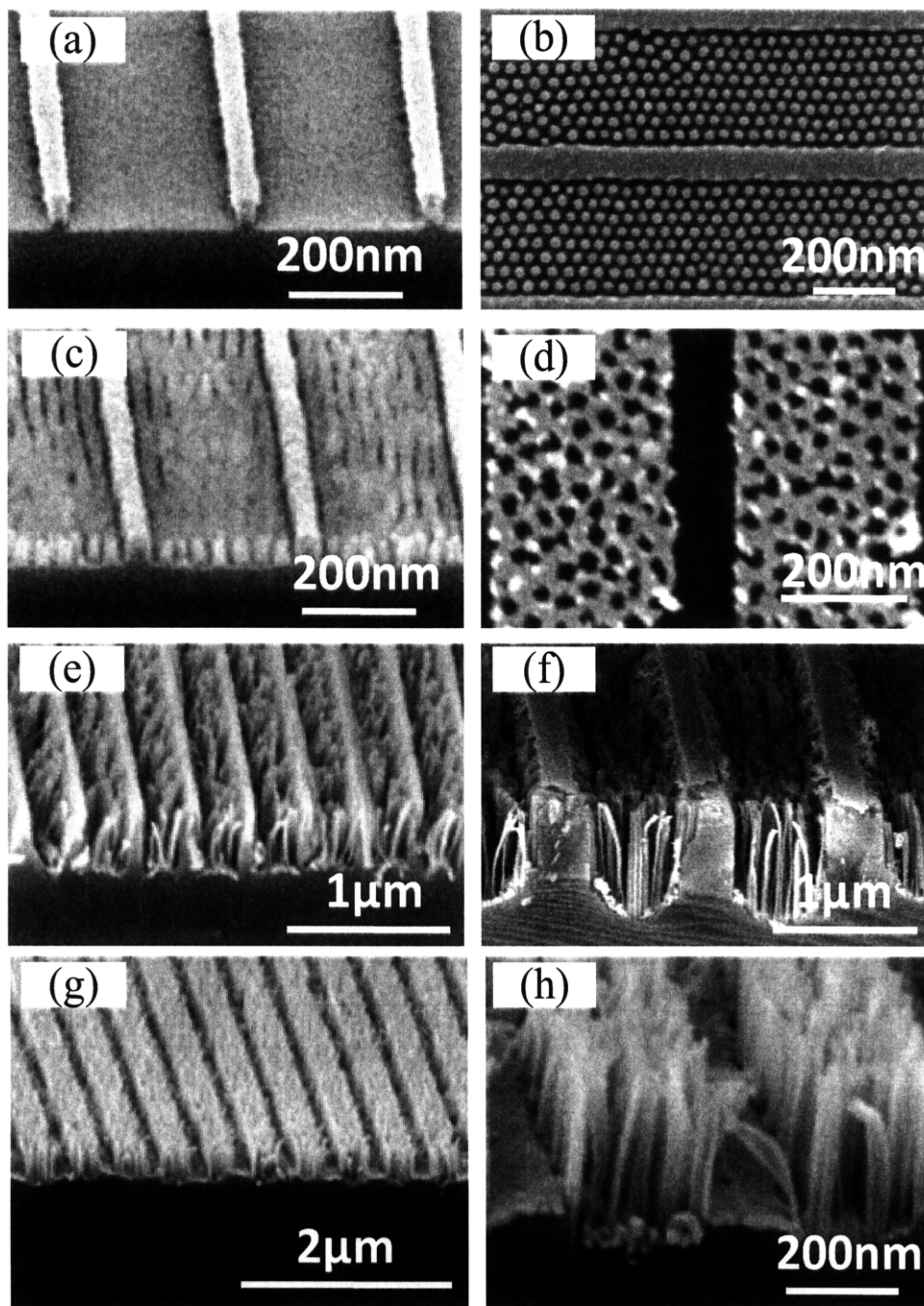

Figure 7-10 SEM images of templated SiNW fabrication: (a) ARC gratings (period = 350 nm) fabricated using interference lithography; (b) PS-*b*-PFS 47/15 self-assembled inside gratings, shown after the PS matrix has been removed by oxygen RIE; (c) Oxide pillar arrays in oxide gratings; (d) 10 nm thick Au antidot arrays after HF lift-off; (e) Final wire-in-trench structure after etching in a solution of hydrofluoric acid and hydrogen peroxide; (f) Wires etched in a different grating with a 1000 nm period (made from PS-*b*-PFS 47/15); (g) Strips of SiNW arrays patterned using a removable ARC grating (made from PS-*b*-PFS 43/12); (c) Higher magnification image of wire arrays without the trench structure.

A variation of this process was used to form SiNW arrays without the trench structure (Figure 7-9(b)). After templated self assembly of PS-*b*-PFS microdomains in ARC gratings and removal of the PS matrix, the ARC gratings were removed by soaking in n-methyl pyrrolidone to leave behind only rows of PFS spherical microdomains.[69] The polymer was protected against dissolution in solvents by an inorganic oxide shell formed during the oxygen RIE process. A 12nm-thick Au thin film was then deposited and antidot arrays were created using HF lift-off. Etching in HF/H_2O_2 led to formation of rows of free-standing silicon nanowire clusters on a flat substrate, as shown in Figure 7-10(g) and (h).

7.2.3. Control of Size Distributions, Aspect Ratios, Densities and Locations

The control of the size, density, and location of nanowires is critical for array-type device applications. In our process, the monodispersity of the SiNWs is governed both by the size distribution of the PFS spheres, and by the fidelity of pattern transfer into the gold and subsequently into the Si. The size distributions of wires patterned using PS-*b*-PFS 47/15 and PS-*b*-PFS 43/12 are plotted in Figure 7-11.

The wire diameters were measured from SEM images taken at several locations on the sample. The average and standard deviation of the diameters measured for wires made using PS-*b*-PFS 47/15 and PS-*b*-PFS 43/12 were 22.06 nm $\pm$14.14% and 19.55 nm $\pm$18.11%, respectively, while the average diameter and standard deviation of the etched PFS domains were 24.92 nm $\pm$12.24% for 47/15 and 21.68$\pm$16.01% for 43/12, and the period was 35 nm for 47/15 and 29.5 nm for 43/12. The average diameters of the wires were 2-3 nm smaller than that of the PFS spheres due to shrinkage of spheres during the subsequent dry etching steps.

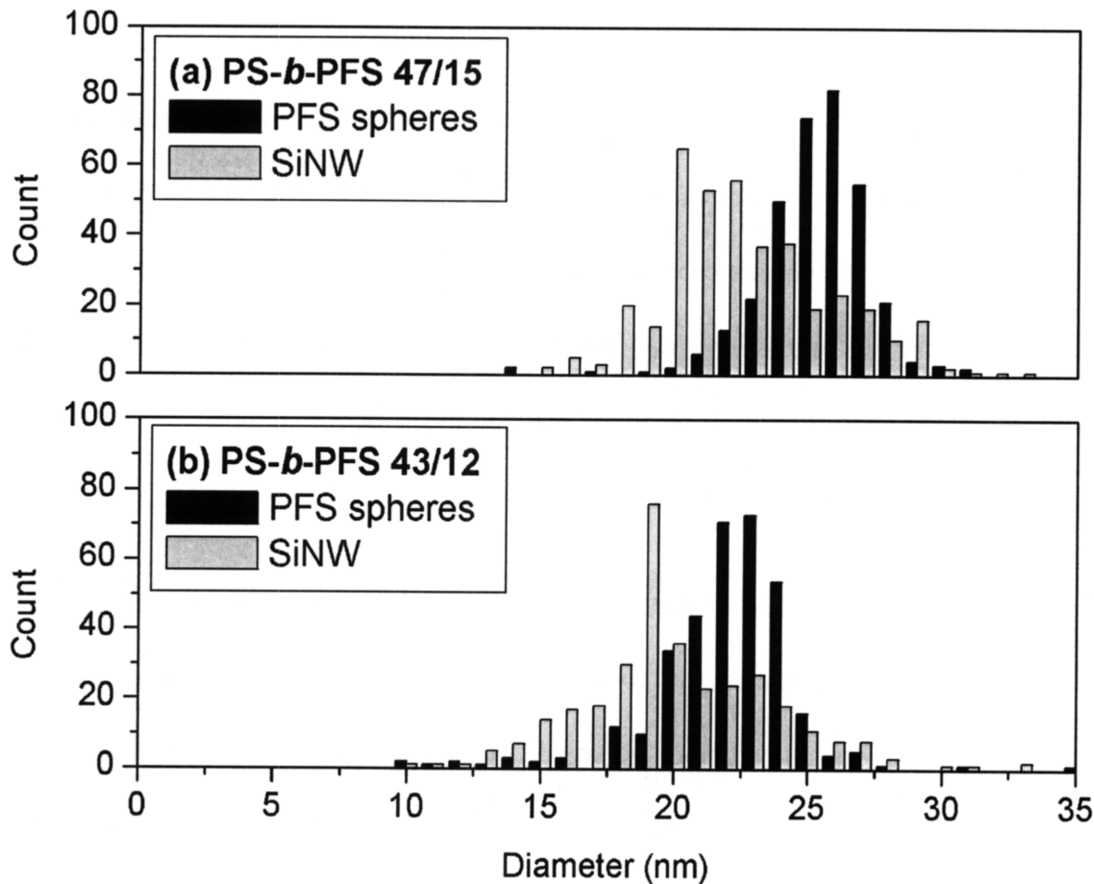

Figure 7-11 Diameter distributions for the wires and the PFS spherical microdomains. (a) PS-*b*-PFS 47/15 diblock copolymer, and (b) PS-*b*-PFS 43/12 diblock copolymer (bottom).

Comparing the standard deviations in PFS sphere and SiNW diameters, it is clear that the variability in NW diameters originates primarily from dispersity in the PFS sphere sizes, and the subsequent liftoff and metal-assisted etching processes lead to only a minor broadening in NW diameter distribution. The distribution in sphere sizes is attributed to kinetic limitations during the microphase segregation of the PS-*b*-PFS. The polymers used in this study have a larger molecular weight than the PS-*b*-PFS 33/10 used in our previous work, and a correspondingly

lower diffusivity and higher dispersity in sphere sizes. For comparison, a PS-*b*-PFS 91/21 spherical morphology block copolymer with period 56 nm, annealed at a higher temperature of 180°C for 48 hr, was used as an etch mask to form metal 'dots' with a standard deviation in of the diameter distribution of 9%.[70] The low diffusivity of PS-*b*-PFS 47/15 and 43/12 is also believed responsible for the relatively poor long range ordering of the PFS spheres within the topographical templates (Fig. 7-10(b)) compared to previous work on PS-*b*-PFS 33/10, which can order in grooves over defect-free distances of several microns.[71]

The SiNWs made by this method are distinguished by a very high aspect ratio. It is commonly observed that high aspect-ratio structures cluster at their tips, due to van der Waals or electrostatic charges on the newly formed surfaces,[72] facilitated by capillary forces present during drying after liquid immersion.[73] If the attractive forces between wires are greater than the force required to bend the wires, sheaf-like structures result as the wires stick together, as shown in Figure 7-12(a). The capillary force present during drying results primarily from surface tension at the solid-liquid interface as the liquid evaporates. To circumvent this problem, the sample is subjected to critical point drying (CPD) in which the liquid-to-vapor phase transition occurs continuously at the critical point. This is accomplished by heating a liquid in a closed system to reach the critical pressure at the critical temperature. The liquid and gas states of a substance are no longer distinguishable at this point. The liquid within the specimen can therefore pass from the liquid to gas phase with zero surface tension. In our system, CO_2 serves as the medium for the CPD procedure. Since it is not miscible with water, the water is first replaced with alcohol as an intermediate fluid. The result of the CPD process is shown in Figure 7-12(b). Silicon nanowires with aspect ratios as high as 220 with very little clustering were fabricated using this technique.

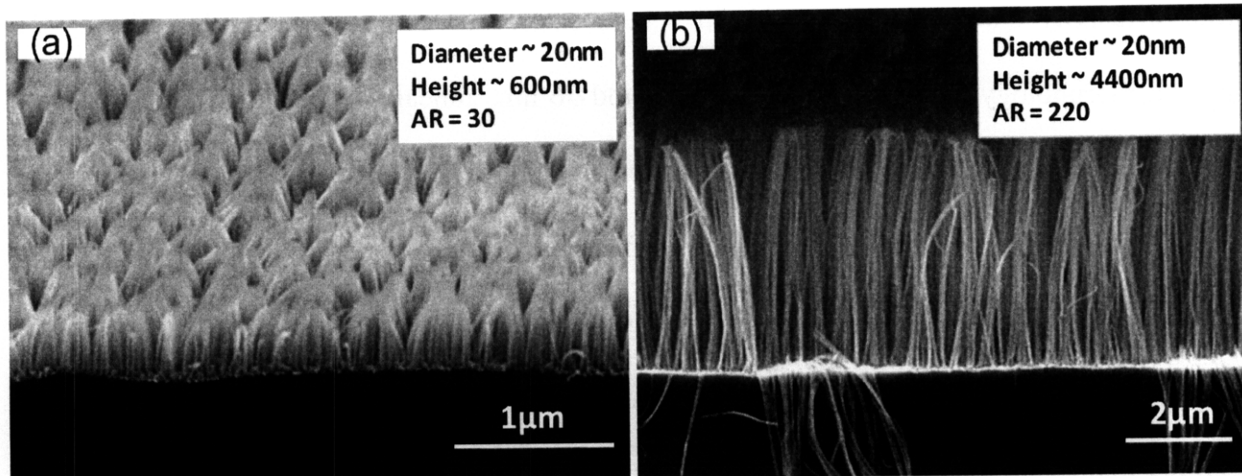

Figure 7-12 (a) SiNW arrays without critical point drying show clustering at the wire tips at a relatively low aspect ratio of 30; (b) SiNW arrays with critical point drying show much less bending at aspect ratios as high as 220. PS-*b*-PFS 47/15 was used in both cases.

7.2.4 Properties of nanowires

The crystallinity of the SiNWs was investigated using high resolution transmission electron microscopy (HRTEM). Figure 7-8(e) shows a typical TEM image of a wire array and Figure 7-8(f) shows a HRTEM image of a single SiNW. The single crystallinity and crystallographic orientation of the wires were investigated by selected area diffraction (SAD) of regions encompassing both the wires and the substrate, and fast Fourier transform (FFT) of a single wire. As shown in the insets of 7-8(e), the SAD patterns of the Si (100) substrate (upper inset) and the wires (lower inset) are nearly identical. The smearing of the diffraction patterns of the wires can be attributed to wire bending from the embedded epoxy. The FFT pattern also shows that the axial orientation of the SiNW is along the [100] direction. The result was expected as the wires were directly etched from the [100] single-crystal silicon substrate. In addition to the good crystallinity of the nanowires, we also expect little diffusion of gold into the wires because the complete wire forming process is carried out at room temperature. The gold

catalyst film can be readily removed by immersing the sample in commercially available iodine-based gold etchants.

7.2.5 Conclusions

We fabricated dense arrays of high-aspect ratio, single crystalline silicon nanowires using a combined approach consisting of metal-assisted etching and block copolymer lithography. The high aspect ratio was made possible through use of critical point drying, which significantly reduced clustering at the wire tips. We also demonstrated fabrication of silicon nanowire arrays at lithographically defined locations by first assembling the block copolymer in topographic features. Although the process was demonstrated using gratings, it can be easily applied to other physical template geometries. The excellent control that is possible in the placement accuracy, size, and geometry of block copolymer microdomains,[62, 69, 74] which includes the formation of both square symmetry[75] and close packed arrays, allows for extensive flexibility in the placement of wires at desired locations over a large area. This will facilitate broad use of such arrays in photonic and sensing devices, in which high device densities and/or high surface-to-volume ratios are critical for optimum performance.

Reference

1. Chuang, V. P.; Jung, W.; Ross, C. A.; Cheng, J. Y.; Park, O.-H.; Kim, H.-C. *Journal of Applied Physics* **2008,** 103, (7), 074307-5.

2. Cowburn, R. P.; Adeyeye, A. O.; Bland, J. A. C. *Applied Physics Letters* **1997,** 70, (17), 2309-2311.

3. Torres, L.; Lopez-Diaz, L.; Iniguez, J. *Applied Physics Letters* **1998,** 73, (25), 3766-3768.

4. Heyderman, L. J.; Nolting, F.; Backes, D.; Czekaj, S.; Lopez-Diaz, L.; Klaui, M.; Rudiger, U.; Vaz, C. A. F.; Bland, J. A. C.; Matelon, R. J.; Volkmann, U. G.; Fischer, P. *Physical Review B (Condensed Matter and Materials Physics)* **2006,** 73, (21), 214429-12.

5. Yu, M.; Malkinski, L.; Spinu, L.; Zhou, W.; Whittenburg, S. *Journal of Applied Physics* **2007,** 101, 09F501-3.

6. Tanaka, M.; Saitoh, E.; Miyajima, H.; Yamaoka, T.; Iye, Y. *Physical Review B (Condensed Matter and Materials Physics)* **2006,** 73, (5), 052411-4.

7. Wang, C. C.; Adeyeye, A. O.; Singh, N.; Huang, Y. S.; Wu, Y. H. *Physical Review B* **2005,** 72, (17), 174426.

8. Wang, C. C.; Adeyeye, A. O.; Wu, Y. H. *Journal of Applied Physics* **2003,** 94, (10), 6644-6648.

9. Castaño, F. J.; Nielsch, K.; Ross, C. A.; Robinson, J. W. A.; Krishnan, R. *Applied Physics Letters* **2004,** 85, (14), 2872-2874.

10. Xiao, Z. L.; Han, C. Y.; Welp, U.; Wang, H. H.; Vlasko-Vlasov, V. K.; Kwok, W. K.; Miller, D. J.; Hiller, J. M.; Cook, R. E.; Willing, G. A.; Crabtree, G. W. *Applied Physics Letters* **2002,** 81, (15), 2869-2871.

11. Ma, Y. G.; Lim, S. L.; Ong, C. K. *Journal of Physics D: Applied Physics* **2007,** 40, (4), 935-941.

12. Jaafar, M.; Navas, D.; Asenjo, A.; Vazquez, M.; Hernandez-Velez, M.; Garcia-Martin, J. M. *Journal of Applied Physics* **2007,** 101, 09F513-3.

13. Kiziroglou, M. E.; Li, X.; Gonzalez, D. C.; de Groot, C. H.; Zhukov, A. A.; de Groot, P. A. J.; Bartlett, P. N. *Journal of Applied Physics* **2006,** 100, (11), 113720-5.

14. Liu, K.; Baker, S. M.; Tuominen, M.; Russell, T. P.; Schuller, I. K. *Physical Review B* **2001,** 63, (6), 060403-4.

15. Kubo, T.; Parker, J. S.; Hillmyer, M. A.; Leighton, C. *Applied Physics Letters* **2007,** 90, (23), 233113-3.

16. Yu, C. T.; Jiang, H.; Shen, L.; Flanders, P. J.; Mankey, G. J. *Journal of Applied Physics* **2000,** 87, 6322-6324.

17. Adeyeye, A. O.; Bland, J. A. C.; Daboo, C. *Applied Physics Letters* **1997,** 70, (23), 3164-3166.

18. Vavassori, P.; Gubbiotti, G.; Zangari, G.; Yu, C. T.; Yin, H.; Jiang, H.; Mankey, G. J. *Journal of Applied Physics* **2002,** 91, 7992-7994.

19. Torres Bruna, J. M.; Bartolomé, J.; García Vinuesa, L. M.; Garcia Sanchez, F.; Gonzalez, J. M.; Chubykalo-Fesenko, O. A. *Journal of Magnetism and Magnetic Materials* **2005,** 290-291, (Part 1), 149-152.

20. Barnard, J. A.; Fujiwara, H.; Inturi, V. R.; Jarratt, J. D.; Scharf, T. W.; Weston, J. L. *Applied Physics Letters* **1996,** 69, (18), 2758-2760.

21. Butera, A.; Weston, J. L.; Barnard, J. A. *Journal of Applied Physics* **1997,** 81, (11), 7432-7436.

22. Barnard, J. A.; Butera, A.; Fujiwara, H.; Inturi, V. R.; Jarratt, J. D.; Klemmer, T. J.; Scharr, T. W.; Weston, J. L. *Journal of Applied Physics* **1997,** 81, 5467-5469.
23. Butera, A.; Weston, J. L.; Barnard, J. A. *IEEE Transactions on Maganetics* **1998,** 34, (4), 1024-1026.
24. Rahman, M. T.; Liu, X.; Morisako, A. *Journal of Applied Physics* **2006,** 99, 08G904-3.
25. Tofail, S. A. M.; Rahman, I. Z.; Rahman, M. A. *Journal of Applied Physics* **2002,** 91, 7998-8000.
26. Navas, D.; Hernandez-Velez, M.; Asenjo, A.; Jaafar, M.; Baldonedo, J. L.; Vazquez, M. *IEEE Transactions on Magnetics* **2006,** 42, (10), 3057-3059.
27. Liu, K.; Chien, C. L. *IEEE Transactions on Magnetics* **1998**, 1021-1023.
28. Heyderman, L. J.; Solak, H. H.; Nolting, F.; Quitmann, C. *Journal of Applied Physics* **2004,** 95, 6651-6653.
29. Shin, K.; Leach, K. A.; Goldbach, J. T.; Kim, D. H.; Jho, J. Y.; Tuominen, M.; Hawker, C. J.; Russell, T. P. *Nano Letters* **2002,** 2, (9), 933-936.
30. Wang, C. C.; Adeyeye, A. O.; Singh, N. *Applied Physics Letters* **2006,** 88, (22), 222506-3.
31. Sundstrom, L.; Krupp, L.; Delenia, E.; Rettner, C.; Sanchez, M.; Hart, M. W.; Kim, H.-C.; Zhang, Y. *Applied Physics Letters* **2006,** 88, (24), 243107-3.
32. Freer, E. M.; Krupp, L. E.; Hinsberg, W. D.; Rice, P. M.; Hedrick, J. L.; Cha, J. N.; Miller, R. D.; Kim, H.-C. *Nano Letters* **2005,** 5, (10), 2014-2018.
33. O.-H. Park; Cheng, J. Y.; Hart, M.; Topuria, T.; Rice, P. M.; Krupp, L. E.; Miller, R. D.; Ito, H.; Kim, H. C. *Advanced Materials* **2008,** 20, (4), 738-742.
34. Cheng, J. Y.; Jung, W.; Ross, C. A. *Physical Review B* **2004,** 70, (6), 064417.
35. Castaño, F. J.; Hao, Y.; Hwang, M.; Ross, C. A.; Vogeli, B.; Smith, H. I.; Haratani, S. *Applied Physics Letters* **2001,** 79, (10), 1504-1506.
36. O'Handley, R. C., *Modern Magnetic Materials: Principles and Applications* Wiley: New York, NY, 1999; p 192, 290, and 332-335.
37. Paul, D. I. *Journal of Applied Physics* **1982,** 53, (3), 1649-1654.
38. Dijkstra, L. J.; Wert, C. *Physical Review* **1950,** 79, (6), 979-985.
39. O'Handley, R. C.; Megusar, J.; Sun, S. W.; Hara, Y.; Grant, N. J. *Journal of Applied Physics* **1985,** 57, (8), 3563-3565.
40. Middelhoek, S. *Journal of Applied Physics* **1963,** 34, (4), 1054-1059.
41. Suzuki, T.; Wilts, C. H. *Journal of Applied Physics* **1969,** 40, (3), 1216-1217.
42. Wu, Y.; Yan, H.; Huang, M.; Messer, B.; Song, J. H.; Yang, P. *Chemistry: A European Journal* **2002,** 6, (8), 1261-1268.
43. Cui, Y.; Zhong, Z.; Wang, D.; Wang, W. U.; Lieber, C. M. *Nano letters* **2003,** 3, (2), 149-152.
44. Cui, Y.; Wei, Q.; Park, H.; Lieber, C. M. *Science* **2001,** 293, (5533), 1289-1292.
45. Goldberger, J.; Hochbaum, A. I.; Fan, R.; Yang, P. *Nano letters* **2006,** 6, (5), 973-977.
46. Westwater, J.; Gosain, D. P.; Tomiya, S.; Usui, A. *J. Vac. Sci. Technol. B* **1997,** 15, 554-557.
47. Wu, Y.; Yang, P. *J. Am. Chem. Soc.* **2001,** 123, (13), 3165-3166.
48. Fuhrmann, B.; Leipner, H. S.; Höche, H.-R.; Schubert, L.; Werner, P.; Gösele, U. *Nano letters* **2005,** 5, (12).
49. Gudiksen, M. S.; Lieber, C. M. *J. Am. Chem. Soc.* **2000,** 122, 8801-8802.

50. Schmidt, V.; Senz, S.; Gösele, U. *Nano letters* **2005,** 5, (5), 931-935.
51. Cheung, C. L.; Nikolic, R. J.; Reinhardt, C. E.; Wang, T. F. *Nanotechnology* **2006,** 17, 1339-1343.
52. Gowrishankar, V.; Miller, N.; McGehee, M. D.; Misner, M. J.; Ryu, D. Y.; Russell, T. P.; Drockenmuller, E.; Hawker, C. J. *Thin Solid Films* 513, (1-2), 289-294.
53. Liu, H. I.; Biegelsen, D. K.; Johnson, N. M.; Ponce, F. A.; Pease, R. F. W. *J. Vac. Sci. and Tech. B* **1993,** 11, (6), 2532-2537.
54. Kedzierski, J.; Bokor, J.; Kisielowski, C. *J. Vac. Sci. Technology B* **1997,** 15, (6), 2825-2828.
55. Peng, K.; Zhang, M.; Lu, A.; Wong, N.-B.; Zhang, R.; Lee, S.-T. *Applied Physics Letters* **2007,** 90, 13123.
56. Lehmann, V.; S. Rönnebeck. *J. Electrochem. Soc.* **1993,** 140, (10), 2836-2843.
57. Li, X.; Bohn, P. W. *Applied Physics Letters* **2000,** 77, 2572-2574.
58. Peng, K.; Wu, Y.; Fang, H.; Zhong, X. Y.; Xu, Y.; Zhu, J. *Angew. Chem. Int. Ed.* **2005,** (44), 2737-2742.
59. Hochbaum, A. I.; Chen, R.; Delgado, R. D.; Liang, W.; Garnett, E. C.; Najarian, M.; Majumdar, A.; Yang, P. *Nature* **2008,** 451, 163-167.
60. Huang, Z.; Zhang, X.; Reiche, M.; Liu, L.; Shimizu, T.; Senz, S.; Lee, W. *Nano letters* **2008,** 8, (9), 3046-3051.
61. Bates, F. S.; Fredrickson, G. H. *Annu. Rev. Phys. Chem.* **1990,** 41, (1), 525-557.
62. Lee, D.-H.; Shin, D.-O.; Lee, W.-J.; Kim, S. O. *J. Nanoscience and Nanotech.* **2008,** 8, 5571-5575.
63. Thurn-Albrecht, T.; Schotter, J.; Kastle, G. A.; Emley, N.; Shibauchi, T.; Krusin-Elbaum, L.; Guarini, K.; Black, C. T.; Tuominen, M. T.; Russell, T. P. *Science* **2000,** 290, (5499), 2126-2129.
64. Bita, I.; Yang, J. K. W.; Jung, Y. S.; Ross, C. A.; Thomas, E. L.; Berggren, K. K. *Science* **2008,** 321, (5891), 939-943.
65. Cheng, J. Y.; Mayes, A. M.; Ross, C. A. *Nature Materials* **2004,** 3, (11), 823-828.
66. Manners, I. *Chemical Communications* **1999,** 10, 857-865.
67. Lammertink, R. G. H.; Hempenius, M. A.; Chan, V. Z. H.; Thomas, E. L.; Vancso, G. J. *Chemistry of Materials* **2001,** 13, (2), 429-434.
68. Farhoud, M.; Hwang, M.; Smith, H. I.; Schattenburg, M. L.; Bae, J. M.; Youcef-Toumi, K.; Ross, C. A. *IEEE Trans. Magn.* **1998,** 34, (4), 1087-1089.
69. Ilievski, F. Magneticnanostructures patterned by block copolymer lithography. Massachusetts Institute of Technology, Cambridge, MA, 2008.
70. Cheng, J. Y.; Jung, W.; Ross, C. A. *Physical Review B* **2004,** 70, 064417.
71. Cheng, J. Y.; Ross, C. A.; Smith, H. I.; Thomas, E. L. *Advanced materials* **2006,** 18, (19), 2505-2521.
72. Zhang, M.-L.; Peng, K.-Q.; Fan, X.; Jie, J.-S.; Zhang, R.-Q.; Lee, S.-T.; Wong, N.-B. *J. Phys. Chem. C* **2008,** 112, 4444-4450.
73. Ahn, M.; Heilmann, R. K.; Schattenburg, M. L. *J. Vac. Sci. Technol. B* **2007,** 25, (6), 2593-2597.
74. Stoykovich, M. P.; Muller, M.; Kim, S. O.; Solak, H. H.; Edwards, E. W.; de Pablo, J. J.; Nealey, P. F. *Science* **2005,** 308, (5727), 1442-1446.

75. Tang, C.; Lennon, E. M.; Fredrickson, G. H.; Kramer, E. J.; Hawker, C. J. *Science* **2008,** 322, (5900), 429-432.

Chapter 8 Conclusions and Future Work

8.1 Conclusions

Block copolymer lithography provides a simple and cost-effective route to overcome the limitations of optical lithographic techniques and to create features down to below 10 nm. While block copolymer lithography has made considerable progresss, several challenges exist.[1] One of the main challenges is to assemble appropriate patterns for targeted applications. In this thesis, we have demonstrated two routes to broaden the range of accessible geometries: templated assembly of diblock copolymers and the use of triblock terpolymers.

1D arrays with well-controlled size, ellipticity and period of the domains and 3D arrays with square symmetry on the top surface have been made from templating spherical diblock copolymer polystyrene-*b*-polyferrocenylsilane (PS-*b*-PFS) within top-down defined templates. Due to the geometric constraints, the block copolymer self-assembled in FCC packing in V-shaped grooves. In 1D arrays, the spheres distorted into ellipsoids and the aspect ratio was tuned by the groove width. Although there has been extensive work on the use of self-assembled diblock copolymers for nanolithography, there are few reports of the use of multiblock copolymers, which can form a more diverse range of nanoscale pattern geometries. Pattern transfer from thin films of a self-assembled poly(butadiene-*b*-styrene-*b*-methyl methacrylate) (PB-*b*-PS-*b*-PMMA) triblock terpolymer with all organic segments was demonstrated. Polymers of different total molecular weight were synthesized with a predicted morphology consisting of PMMA-core/PS-shell cylinders in a PB matrix. By adjusting the solvent-annealing conditions and the film thickness, thin films with vertically oriented cylinders were formed. The PMMA cylinder cores and the PB matrix were then removed using selective etching to leave an array of PS rings, and the ring pattern was transferred into a silica film by reactive ion etching to form 19

nm high silica rings. The quality of the closepacked rings was improved by using another core-shell structured triblock terpolymer, polystyrene-b-polyferrocenylsilane-b-poly(2-vinylpyridine) (PS-*b*-PFS-*b*-P2VP) in which one of the blocks contains inorganic components which impart high etch selectivity and etch resistance. By spin-coating and solvent annealing, thin films of the polymers were self-assembled into arrays of core-shell structures oriented perpendicular to the top surface of the film. The morphologies were controlled by substrate chemistry and the choice of solvent annealing vapors. Finally, directed assembled triblock terpolymer polyisoprene-*b*-polystyrene-*b*-polyferrocenylsilane (PI-*b*-PS-*b*-PFS) forms square array of nanostructures with controlled packing orientation. The square symmetry array, which is not found in diblock copolymers, has applications in via formation, magnetic patterned media, and other applications. The square array pattern was successfully transferred into 30 nm high silica dots.

Single layer Co and multilayer Co/Cu/NiFe pseudo-spin-valve antidot arrays were made using a block copolymer templating method. The holes raise the coercivity of single-layer Co films, and in the multilayers lead to an antiparallel alignment of the moments in the Co and NiFe layers at remanence, as a result of the strong magnetostatic interactions between the layers. Micromagnetic modeling was performed to confirm the results, and the trend in coercivity was explained in terms of the interactions between the nanoscale holes and the domain walls in the films.

Silicon nanowires with aspect ratio up to 220 from block copolymer lithography in conjunction with metal-assisted etching were demonstrated. The distribution of wire diameters is narrow and closely follow the size distribution of the block-polymer, with a standard deviation of 3.12 nm for wires of mean diameters 22.06 nm. The wire placement was controlled by templated assembly of a block copolymer.

8.2 Future work

The use of templated assembly of diblock copolymer and triblock terpolymer thin films provide rich opportunities to explore novel structures. Besides the morphologies discussed in the thesis, linear ABC triblock polymers have other interesting morphologies as well. These include lamellae-with-cylinders-at-the-interface-phase and three-phase four-layer-lamellae, as shown in fig. 8-1, and have been observed in bulk films of poly(styrene-b-ethylene-co-butylene-b-methyl methacrylate), PS-PEB-PMMA.[2] For this polymer, $\chi_{AC} < \chi_{AB} \approx \chi_{BC}$ so contact between A and C is favorable. If the middle block is short, B domains would form in the interface of A and B. In addition to this, by keeping the end-block ratio equal (A/C~1) and making the volume ratio of the middle block larger than 0.3, cylinders or spheres of A and C on a square lattice in a matrix of B can be formed. Lamellae-with-cylinders-at-the-interface-phase may be used as a template for a magnetic domain wall memory device and three-phase four-layer-lamellae can be used to create nanolines with different mesa/trench width ratio. The middle block can be designed to be the lowest surface energy block to form perpendicular lamellae spontaneously.

In contrast to linear terpolymers, miktoarm (star) terpolymers are hard to synthesize but have even more interesting morphologies due to their complex architecture. Abetz and collaborators have studied the morphologies of star terpolymers of PS, PB, and P2VP by changing the volume fraction of three components.[3] A novel structure of concentric rhombohedra has been obtained from star terpolymers PS/PI/PMMA. This rhombohedral structure is a consequence of minimization of interfacial area and chain stretching.[4]

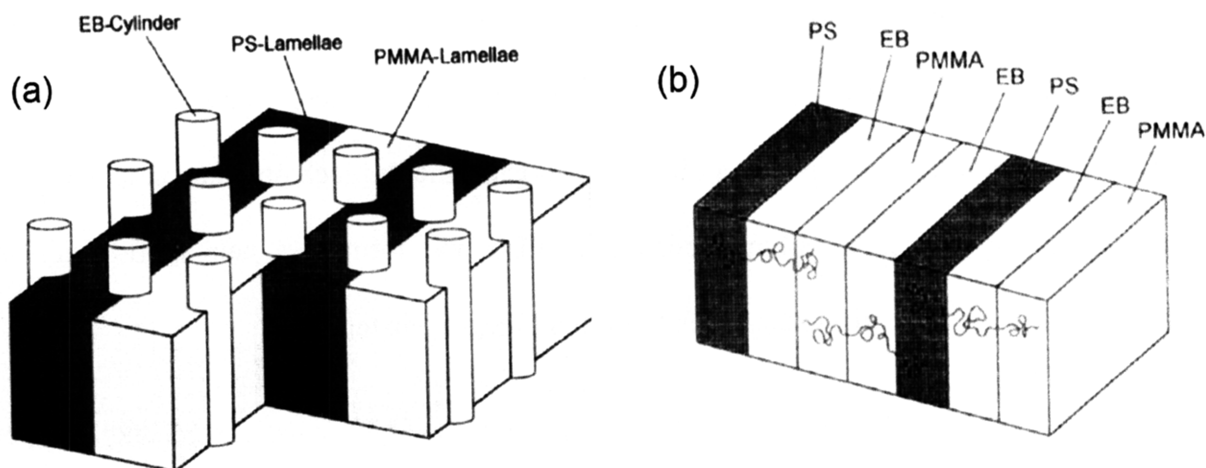

Figure 8-1 schematic of (a) lamellae-with-cylinders-at-the-interface-phase (b) three-phase four-layer-lamellae.

Although triblock copolymers have many interesting morphologies, it is important to also consider etch selectivity among each block. One of the ideal materials for a lithographic template would be a block containing a metal or silicon based organic polymer such as PFS (or PDMS), as already demonstrated in the thesis. An alternative can be to add some functional groups or a nanohybrid inorganic precursor to one of the blocks. For example, a new polymer, poly(styrene-4-hydroxystyrene-isoprene)--PS-*b*-PHOST-*b*-PI does not have selective etching resistance from oxygen plasma. Core-shell structured PS-PHOST-PI provides the same morphology as the core-shell structured PB-*b*-PS-*b*-PMM; and PS-PHOST-PI with a composition of 22%/60%/18% is expected to order into cylinders with square array.[5] The radius of the PS cylinder is different from that of PI cylinder and the ordering method for both morphologies is similar to the PB-*b*-PS-*b*-PMMA. In order to preserve the PHOST rings or PHOST matrix in a square arrangement of holes, adding some functional groups is necessary to selectively etch away the PS and PI and leave the PHOST rings or matrix using oxygen RIE. By adding an inorganic precursor

silsesquioxane(SSQ) to the triblock terpolymer, the etch selectivity can be raised. SSQ or organosilicate can also incorporate into polyethylene oxide(PEO) as demonstrated in Chapter 6- the antidot magnetic film was made on a PS-b-PEO+organosilicate block polymer template. As a result, designing a triblock terpolymer containing PEO and forming a nanohybrid with an inorganic precursor is a promising approach to form a lithographic template.

By selecting triblock terpolymer with blocks which have high χ parameters and a proper volume ratio, it is possible to scale the minimum feature size down to below the current limitation of diblock copolymers. As demonstrated in Chapter 5 and 6, cylinder structures were obtained from triblock terpolymers with composition of 16%:28%:56% and 10%:65%:25%. This suggests that the spherical morphology can be formed with minority block composition below 10% or even 5 %,[6] with which the morphology generally falls in the disordered region in diblock copolymers. As a result, with the same total molecular weight, the feature size made by the minority block in triblock terpolymers can be smaller than that in diblock copolymers. In addition, long range order with small feature size may be achieved simultaneously. For example, one can design a core-shell cylindrical or spherical structure of PDMS-*b*-PS-*b*-P2VP with high χ parameter and very low volume ratio of PDMS and select a third block, such as PEO or P2VP, which leads to long range order. Another example is to use a tetragonal packed cylinders structure of a triblock terpolymer with high χ parameter and very low volume ratio of end blocks. By removing (or preserving) both end blocks, the period of hole(or dots) pattern created by triblock terpolymers can be smaller than that created by diblock copolymers with the same total molecular weight. As shown in Chapter 6, with staining, both end blocks were left after

removing the middle block. It is possible to get different period of the dots or holes by staining only some regions of the sample.

For magnetic applications, it is required to transfer patterns such as rings or square arrays of dots into films of Co, NiFe or multilayer magnetic films such as IrMn/Co using ion milling, and study the magnetic properties. The results can be compared with OOMMF micromagnetic simulation and also compared with hexagonal-packed dots. Besides, the packing orientation of square array dots or in-plane cylinders can be controlled by tuning the trench wall chemistry. By patterning different brush layers on the trench wall, controllable packing orientation can be achieved. Moreover, the method for making silicon nanowire shown in Chapter 7 may be useful for applications such as lithium batteries.

Reference

1. *International technology roadmap for semiconductors-emerging research materials*; ITRS 2007 edition: http://www.itrs.net/Links/2007ITRS/2007_Chapters/2007_ERM.pdf.
2. Auschra, C.; Stadler, R. *Macromolecules* **1993,** 26, (9), 2171-2174.
3. Huckstadt, H.; Goldacker, T.; Gopfert, A.; Abetz, V. *Macromolecules* **2000,** 33, (10), 3757-3761.
4. Sioula, S.; Hadjichristidis, N.; Thomas, E. L. *Macromolecules* **1998,** 31, (16), 5272-5277.
5. Jung, K.; Abetz, V.; Stadler, R. *Macromolecules* **1996,** 29, (3), 1076-1078.
6. Mogi, Y.; Nomura, M.; Kotsuji, H.; Ohnishi, K.; Matsushita, Y.; Noda, I. *Macromolecules* **1994,** 27, (23), 6755-6760.